

## **INFORMATION TO USERS**

**This material was produced from a microfilm copy of the original document. While the most advanced technological means to photograph and reproduce this document have been used, the quality is heavily dependent upon the quality of the original submitted.**

**The following explanation of techniques is provided to help you understand markings or patterns which may appear on this reproduction.**

- 1. The sign or "target" for pages apparently lacking from the document photographed is "Missing Page(s)". If it was possible to obtain the missing page(s) or section, they are spliced into the film along with adjacent pages. This may have necessitated cutting thru an image and duplicating adjacent pages to insure you complete continuity.**
- 2. When an image on the film is obliterated with a large round black mark, it is an indication that the photographer suspected that the copy may have moved during exposure and thus cause a blurred image. You will find a good image of the page in the adjacent frame.**
- 3. When a map, drawing or chart, etc., was part of the material being photographed the photographer followed a definite method in "sectioning" the material. It is customary to begin photoing at the upper left hand corner of a large sheet and to continue photoing from left to right in equal sections with a small overlap. If necessary, sectioning is continued again — beginning below the first row and continuing on until complete.**
- 4. The majority of users indicate that the textual content is of greatest value, however, a somewhat higher quality reproduction could be made from "photographs" if essential to the understanding of the dissertation. Silver prints of "photographs" may be ordered at additional charge by writing the Order Department, giving the catalog number, title, author and specific pages you wish reproduced.**
- 5. PLEASE NOTE: Some pages may have indistinct print. Filmed as received.**

**University Microfilms International**

300 North Zeeb Road  
Ann Arbor, Michigan 48106 USA  
St. John's Road, Tyler's Green  
High Wycombe, Bucks, England HP10 8HR

77-16,975

SHANKAR, V. S. Vijaya, 1951-  
DIFFRACTION OF A SHOCK WAVE BY A  
COMPRESSION CORNER; REGULAR AND  
SINGLE MACH REFLECTION.

Iowa State University, Ph.D., 1977  
Economics, theory

**Xerox University Microfilms**, Ann Arbor, Michigan 48106

**Diffraction of a shock wave by a compression corner;  
regular and single Mach reflection**

by

**V. S. Vijaya Shankar**

**A Dissertation Submitted to the  
Graduate Faculty in Partial Fulfillment of  
The Requirements for the Degree of  
DOCTOR OF PHILOSOPHY**

**Major: Aerospace Engineering**

**Approved:**

Signature was redacted for privacy.

**In Charge of Major Work**

Signature was redacted for privacy.

**For the Major Department**

Signature was redacted for privacy.

**For the Graduate College**

**Iowa State University  
Ames, Iowa**

**1977**

## TABLE OF CONTENTS

	Page
NOMENCLATURE . . . . .	111
CHAPTER I. INTRODUCTION . . . . .	1
CHAPTER II. REGULAR REFLECTION. . . . .	10
The Transformed Governing Equations . . . . .	12
Initial Conditions. . . . .	15
Boundary Conditions . . . . .	21
Reflected shock. . . . .	21
Impermeable boundaries . . . . .	24
Outer boundary . . . . .	28
Results . . . . .	28
CHAPTER III. SINGLE MACH REFLECTION . . . . .	41
Double Normalization Procedure. . . . .	43
Initial Conditions. . . . .	45
Boundary Conditions . . . . .	57
Reflected shock. . . . .	57
Mach stem. . . . .	58
Impermeable boundaries . . . . .	59
Shock Speed Calculations. . . . .	59
Floating-Fitting Procedure for the Slip Surface . . . . .	62
Results . . . . .	70
CHAPTER IV. CONCLUDING REMARKS. . . . .	85
ACKNOWLEDGEMENTS . . . . .	86
REFERENCES . . . . .	87
APPENDIX A. STRONG CONSERVATION-LAW FORM OF THE GOVERNING EQUATIONS AND THE GEOMETRIC DERIVATIVES . . . . .	91
APPENDIX B. INTEGRATION PROCEDURE AND STEP SIZE CALCULATIONS. . . . .	98
APPENDIX C. EXACT SOLUTION FOR REGULAR REFLECTION . . . . .	102
APPENDIX D. KENTZER'S SCHEME FOR IMPERMEABLE BOUNDARIES . . . . .	107
APPENDIX E. EXACT TRIPLE POINT SOLUTION . . . . .	113

## NOMENCLATURE

$a$	Speed of sound
$A$	Coefficients of the inviscid equations in nonconservative form
$e$	Total energy per unit volume
$E$	$x$ -dependent conservative variable
$E', \bar{E}$	$\eta$ -dependent conservative variables
$F$	$y$ -dependent conservative variable
$F', \bar{F}$	$\xi$ -dependent conservative variables
$\hat{i}, \hat{j}$	Unit vectors in Cartesian system
$I$	Incident shock impingement point
$J$	Jacobian of the transformation
$M_s$	Incident shock Mach number
$p$	Pressure
$q$	Velocity vector
$Q$	Primitive variable vector
$t$	Time
$u, v$	Velocity components in $x, y$ directions
$U$	$t$ -dependent conservative variable
$U', \bar{U}$	$\tau$ -dependent conservative variables
$x, y$	Independent variables in stationary Cartesian frame
$x', y'$	Independent variables in moving Cartesian frame
$\gamma$	Ratio of specific heats
$\delta$	Turning angle

$\Delta\tau$	Integration step size
$\theta_r$	Ramp angle
$\phi$	Shock angle
$(\tau, \eta, \xi)$	Transformed independent variables
$\sigma$	Eigenvalues of the gasdynamic equations
$\chi$	Triple point trajectory angle
$\rho$	Density

#### Subscripts:

$b$	Body surface
$j$	Grid point location in $\eta$ -direction
$k$	Grid point location in $\xi$ -direction
$\max$	Maximum
$M$	Mach stem
$R$	Reflected shock
$s$	Shock
$ss$	Self-similar
$1,2,3,4$	Four regions of the triple point

#### Superscripts:

$n$	Time level
$*$	Limiting value

## CHAPTER I. INTRODUCTION

For well over a quarter of a century experimentalists (1-8) and theoreticians (9-25) have been studying the problem of shock wave diffraction, that is, the deflection of a shock wave whose normal path has been impeded by some obstacle. Current interest in this problem has been generated by researchers (26) investigating the nuclear blast fields around aerospace vehicles and around flush-mounted structures (Figure 1) in an attempt to accumulate a data base for survivability and vulnerability studies. Such parametric information can be used to determine the nonuniform dynamic loading to be applied in structural analysis programs for the design of present day or future generic aerospace systems.

The interaction of a spherical blast wave with a planar surface, such as the examples shown in Figure 1, results in the complete range of shock reflections; that is, from regular reflection at  $0^\circ$  incidence of the blast wave with the surface (Figure 2a) to Mach reflection at  $90^\circ$  incidence (Figure 2b). The determination and the understanding of this interaction is of importance not only to the structural designer interested in the transient blast loading effects but also the aerodynamicist interested in the mechanics of the flow field.

The simplest laboratory experiment designed to study the shock diffraction problem consists of a two-dimensional wedge or ramp mounted on the wall of a shock tube (see Figure 3). Depending on the angle of inclination of the ramp with respect to the shock tube wall  $\theta_r$  and the strength of the planar shock (with Mach number  $M_g$ ), either regular reflection or one of the several types of Mach reflection occurs as shown in

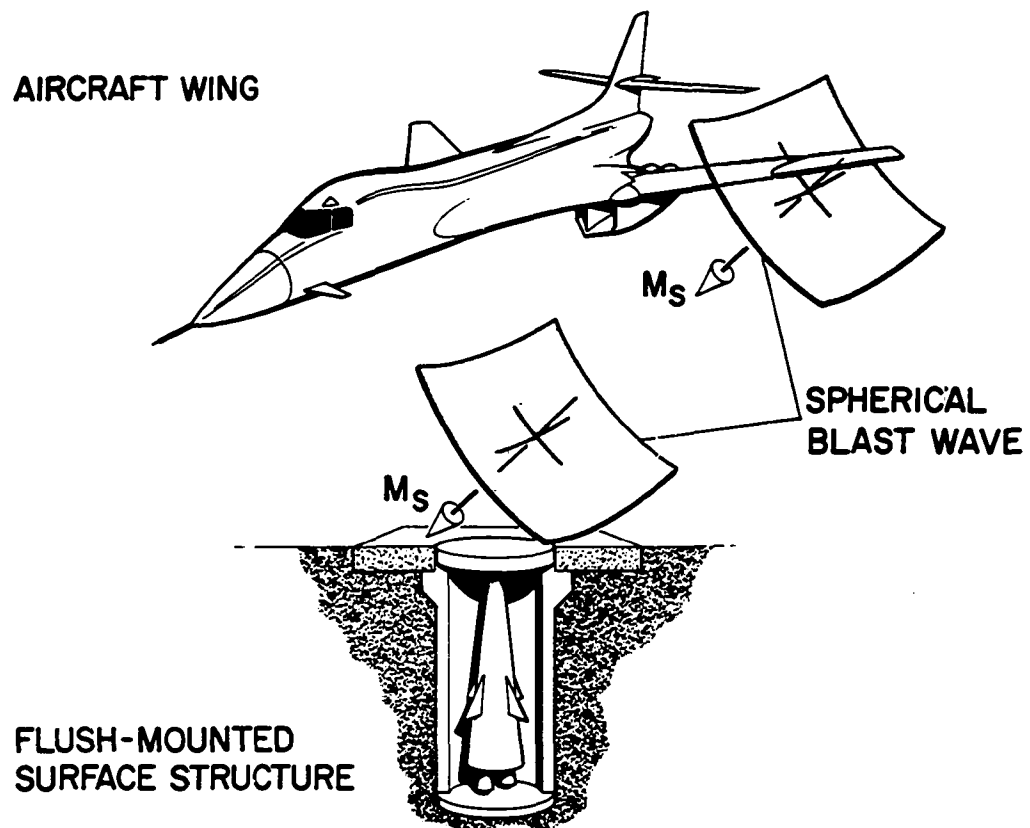


Figure 1. Possible blast-wave encounters with a planar surface



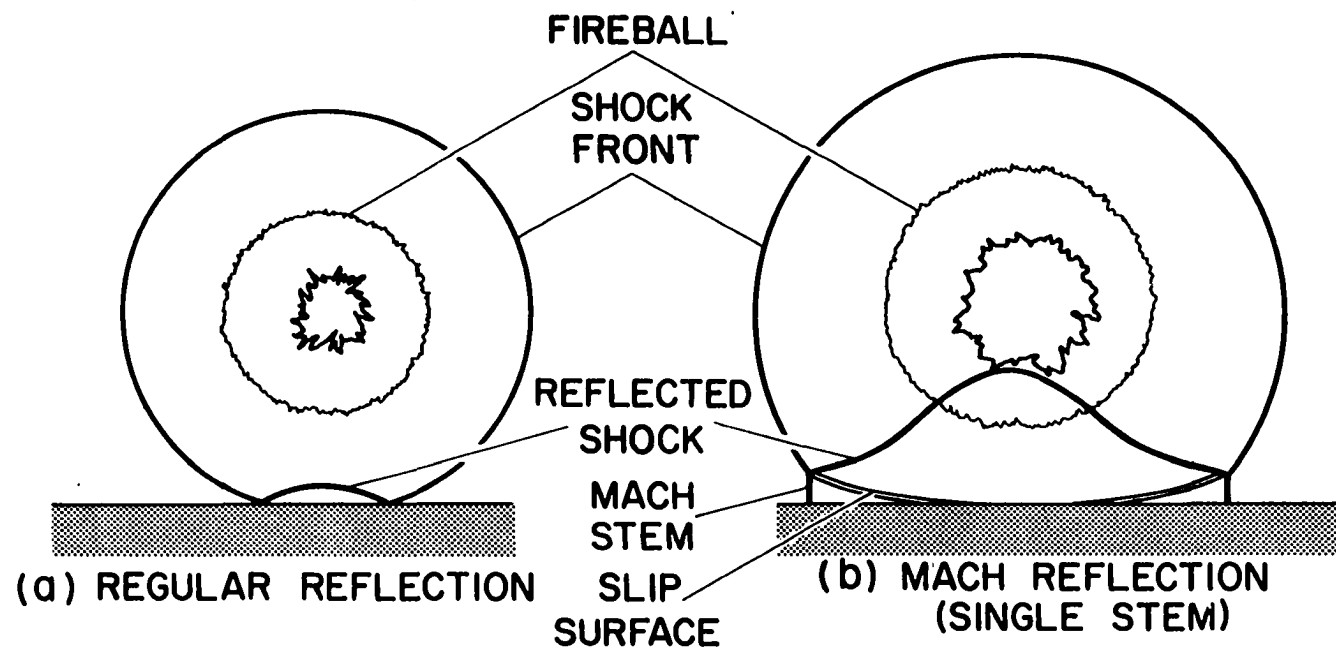


Figure 2. Interaction of spherical blast-wave with planar surface

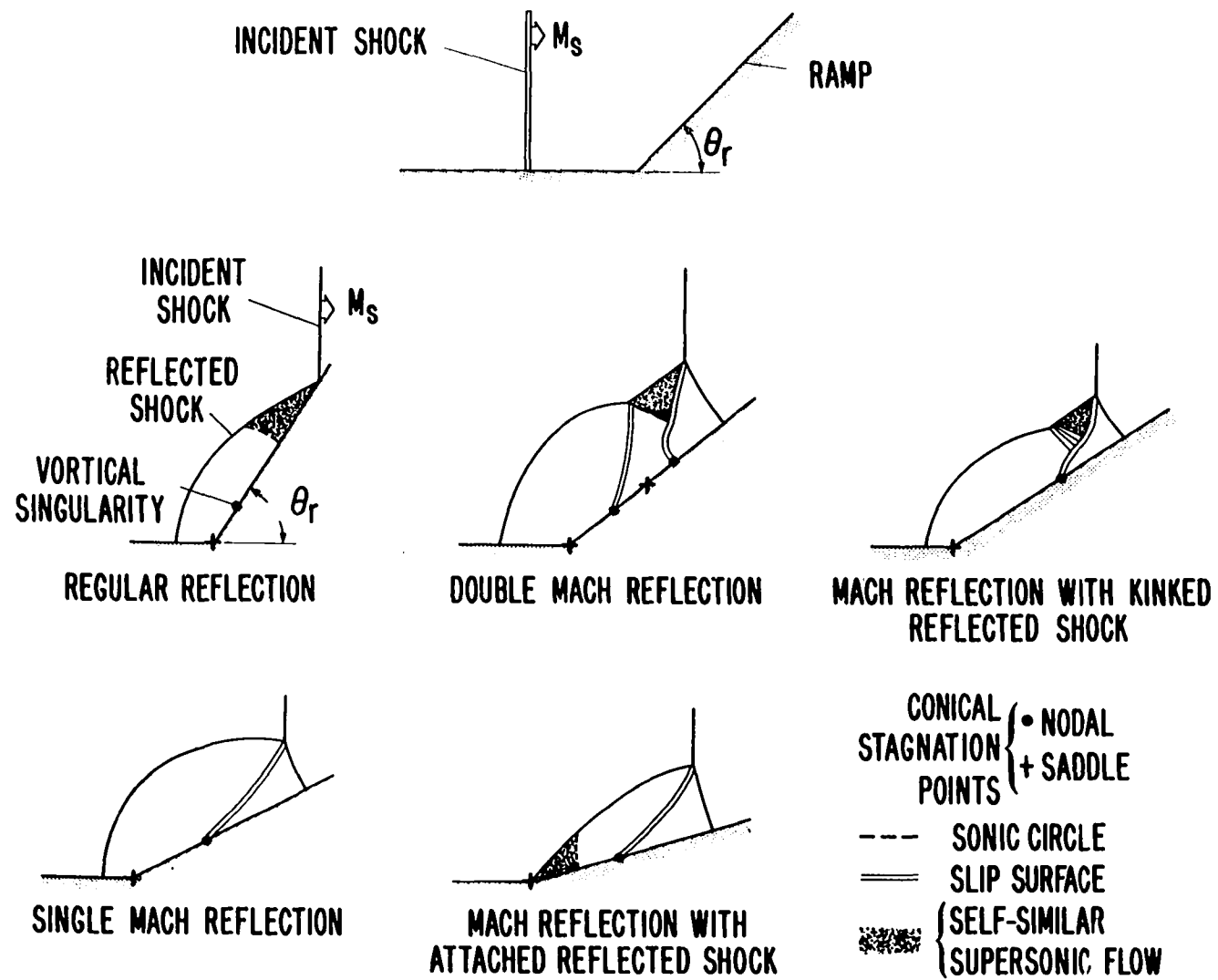
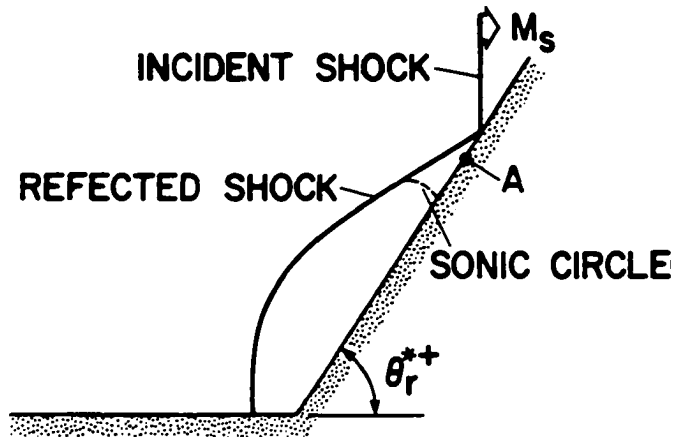


Figure 3. Blast-wave before and after interacting with the compression ramp

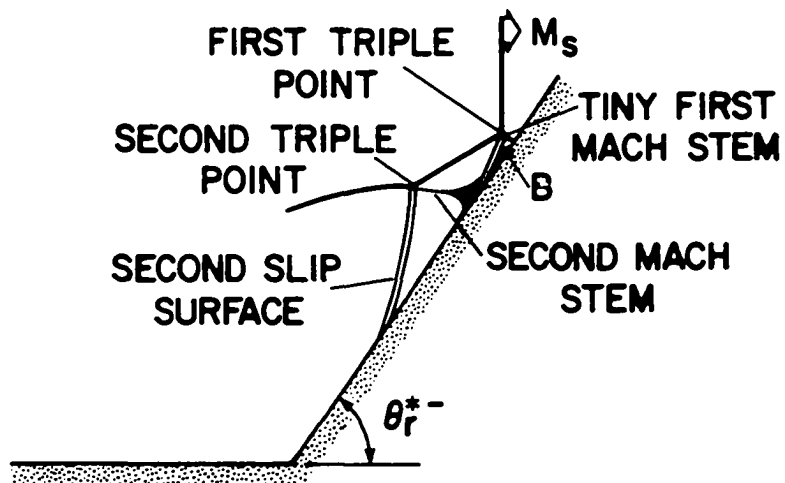
Figure 3. Regardless of the type of reflection process, this shock diffraction problem is self-similar with respect to time since there is no characteristic length associated with the problem.

When the ramp angle is sufficiently large ( $50^\circ \leq \theta_r < 90^\circ$ ) regular reflection results. As the ramp angle is gradually decreased, the shock incident angle ( $90^\circ - \theta_r$ ) increases and the regular reflection first transitions to a double Mach stem configuration with two triple points (see Figure 3). The second triple point disappears as the ramp angle is decreased further and the curvature of the reflected shock reverses. This curvature reversal disappears with further decrease in the ramp angle and a single Mach stem with a smooth reflected shock appears. For very small ramp angles the reflected shock is attached to the ramp edge as shown in Figure 3.

The reason for the formation of a double Mach stem configuration during the transition stage from regular to single Mach reflection can be explained by a careful examination of the flow field shown in Figures 4a and 4b. Let  $\theta_r^*$  be the limiting angle for regular reflection. That is, when  $\theta_r = \theta_r^{*+}$  regular reflection results and when  $\theta_r = \theta_r^{*-}$  a tiny Mach stem is formed which strikes the ramp perpendicularly. The pressure behind the tiny Mach stem (point B in Figure 4b) is considerably lower than the pressure at point A in the limiting regular reflection case. For example, at an incident shock Mach number of 4.71 the pressure at point A for the limiting regular reflection case is 147, while the pressure behind the tiny Mach stem (point B in Figure 4b) is 62.5. Thus, one Mach stem is not sufficient to produce a pressure jump which matches the



(a) LIMITING REGULAR REFLECTION



(b) FORMATION OF A DOUBLE MACH STEM

Figure 4. Transition from regular reflection to double Mach stem

limiting reflection value. A second Mach stem is formed such that the pressure increase across the second Mach stem matches with the limiting regular reflection value. The formation of the second Mach stem is not well understood yet.

The goal of this study is to obtain numerical results for the cases of regular reflection and single Mach reflection with a smooth reflected shock. The double Mach stem case is not included in the present study. All the discontinuities that appear in the flow field are fitted using special logic. The reflected shock and the Mach stem are fitted using the "sharp shock" technique (27,28). A floating discontinuity fitting scheme in conjunction with the method of characteristics is employed to fit the slip surface. In the regular reflection as well as the single Mach stem case there exists two self-similar stagnation points, that is, points at which the self-similar velocity components  $u-x\tau$  and  $v-y/\tau$  are zero; the first is located at the juncture of the wall and the ramp (saddle singularity), and the second, termed a vortical singularity, is located at some point along the ramp (nodal singularity). In the Mach reflection case the slip surface terminates at the vortical singularity on the ramp. All streamlines in the self-similar plane converge at the nodal singularity, and therefore, the entropy is multivalued. At the saddle singularity the streamlines turn away, and the entropy is single-valued. The level of entropy on the stagnation streamline and along the ramp up to the vortical singularity is equal to that behind the normal part of the reflected shock. In the regular reflection case the level of entropy between the vortical singularity and the incident shock impingement

point is equal to that behind the straight part of the reflected shock. In the case of single Mach reflection the level of entropy behind the vortical singularity and the Mach foot is equal to that behind the Mach foot.

From an analysis of the equations governing the flow behavior in the vicinity of conical, self-similar stagnation points (11,29), it can be shown that the pressure is a local maximum at the saddle point of streamlines (juncture of the wall and the ramp), and this point corresponds to a center point of isobars. Similarly it can be shown that the pressure is a local minimum at the nodal point of streamlines (vortical singularity) which corresponds to a saddle point of isobars.

In the present study, the two-dimensional, time-dependent Euler equations which govern these flows are solved with initial conditions that result in either regular reflection or single Mach reflection of the incident shock. The hyperbolic partial differential equations are first transformed to include the self-similarity of the problem. Secondly, a normalization procedure is incorporated to align the discontinuities as computational boundaries to implement the "sharp shock" technique. The self-similar transformation reduces these equations from an unsteady to an equivalent steady set of mixed elliptic-hyperbolic equations. The equations are made totally hyperbolic by reintroducing a time-like or residual term which should approach zero in the converged solution. The final set of equations is written in strong conservation-law form (30,31) and then solved using MacCormack's (32) second-order, finite-difference algorithm.

Unlike previous solutions (12,13,15,22-24) the reflected shock, the Mach stem and the slip surface are all treated as sharp discontinuities thus resulting in a more accurate description of the inviscid flow field. The resulting numerical solutions are compared with available experimental data (5) and existing first-order, shock-capturing numerical solutions (15,22).

## CHAPTER II. REGULAR REFLECTION

When a spherical blast wave strikes a planar surface, regular reflection occurs first and then transitions to Mach reflection as the shock incident angle increases (Figure 2). In this chapter regular reflection of a planar shock is studied as a prelude to understanding more about regular reflection of a spherical incident shock. The simplest laboratory experiment designed to study the shock diffraction problem consists of a two-dimensional ramp mounted on the wall of a shock-tube (Figure 3). The resulting flow field is self-similar because there is no characteristic length associated with the problem. It consists of only the reflected shock (Figure 5) which is straight up to the sonic circle and then curves to become perpendicular to the shock-tube wall. Between the sonic circle and the shock impingement point I the flow field is uniform. The flow field linearly grows with time in the physical plane.

In this problem, there exists two self-similar stagnation points, that is, points at which the self-similar velocity components  $u-x/t$  and  $v-y/t$  are zero; the first is located at the juncture of the wall and the ramp (saddle singularity), and the second, termed a vortical singularity, is located at some point along the ramp (nodal singularity). All self-similar streamlines converge at the nodal point or the vortical singularity, and therefore, the entropy is multivalued. At the saddle point the streamlines turn away, and the entropy is regular. The level of entropy on the stagnation streamline and along the ramp up to the vortical singularity is equal to that behind the normal part of the reflected shock,



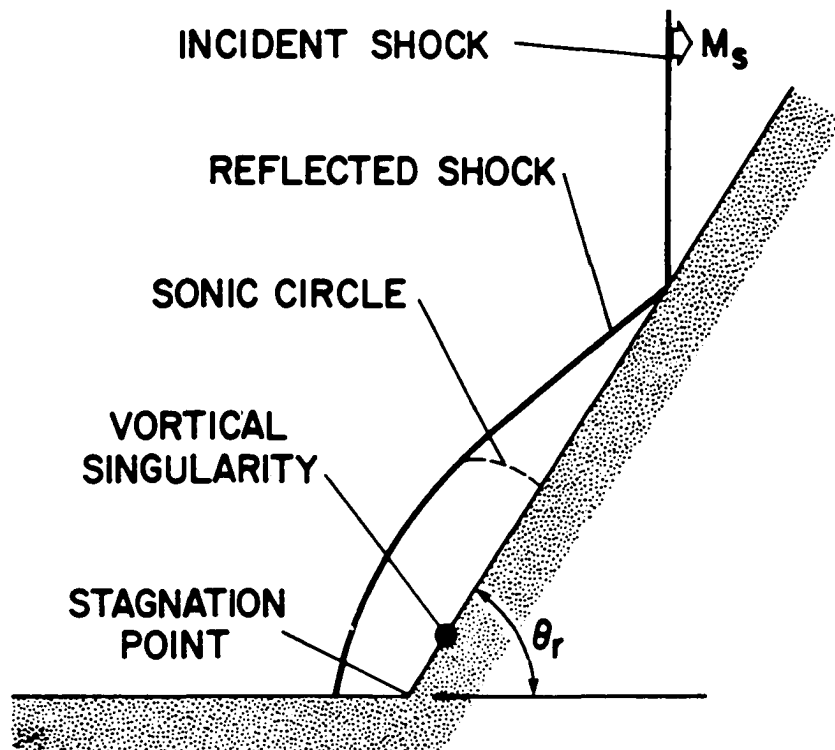


Figure 5. Regular reflection of the incident planar shock

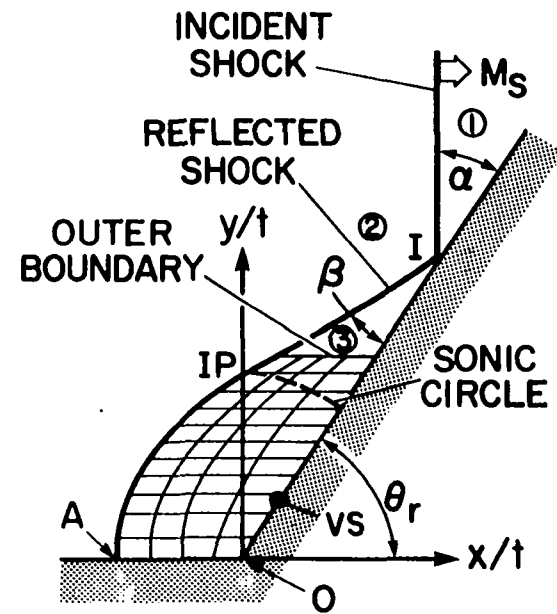
while the level of entropy between the vortical singularity and the shock impingement point is equal to that behind the straight part of the reflected shock.

Two popular techniques for solving supersonic flow problems are currently being used. One is the "shock-capturing" method (28), and the other is the "discontinuity-fitting" (27,33) method. The first method does not require any special logic to treat the discontinuity and hence yields inferior solutions. The discontinuity-fitting procedure requires special treatment for all the discontinuities in the flow field (shocks, slip surfaces, vortical singularities, etc.). This makes the scheme more complicated and involved, but yields a much better solution compared to "shock-capturing" results.

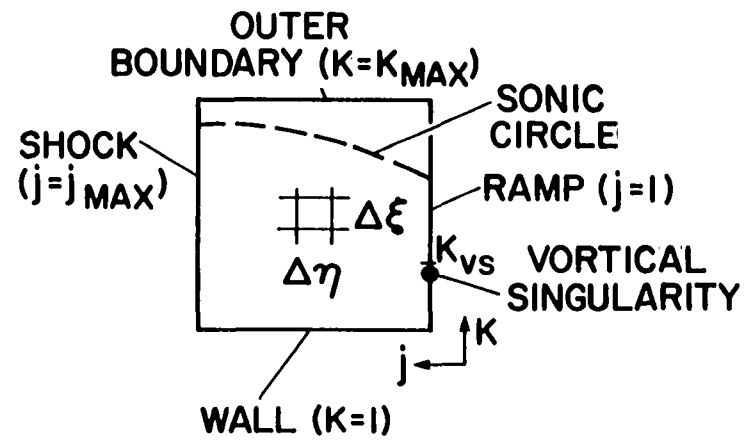
In the present work the "discontinuity-fitting" procedure is adopted and the resulting numerical solutions are compared with available experimental data (5) and existing first-order, shock-capturing numerical solutions (15,22).

#### The Transformed Governing Equations

A Cartesian coordinate system is used in the problem formulation, the origin of which is located at the juncture of the wall and the ramp. The x-axis is aligned with the wall and the y-axis is normal to the wall and in the direction of the ramp (Figure 6a). Under the assumptions of an inviscid, nonheat-conducting, ideal gas, the fluid dynamic equations in strong conservation-law form (30,31) for the independent variable transformation  $\tau = t$ ,  $\eta = \eta(x,y,t)$ , and  $\xi = \xi(x,y,t)$  are



(a) COORDINATE SYSTEM



(b) COMPUTATIONAL PLANE

Figure 6. Coordinate system and the computational plane

$$\left(\frac{U}{J}\right)_{\tau} + \left(\frac{U\eta_t + E\eta_x + F\eta_y}{J}\right)_{\eta} + \left(\frac{U\xi_t + E\xi_x + F\xi_y}{J}\right)_{\xi} = 0 \quad (1)$$

where  $U, E$ , and  $F$  are the conservative variables in the Cartesian coordinate system.  $J$  is the Jacobian of the transformation. Expressions for  $U, E, F$ , and  $J$  along with the derivation of Equation (1) are presented in Appendix A.

In a shock-fitting procedure the shock is treated as one of the computational boundaries, so that jump conditions across the shock can be easily applied. This is done through a normalizing transformation. For the regular reflection problem, the following functions are used for  $\tau$ ,  $\eta$  and  $\xi$  which include the self-similarity of the problem and a normalization of the distance between the ramp and the reflected shock:

$$\left. \begin{aligned} \tau &= t \\ \eta &= \frac{x - x_b(y)}{x_s(y, t) - x_b(y)} \\ \xi &= \frac{y}{t} \end{aligned} \right\} \quad (2)$$

where  $x_b(y)$  represents the equation of the ramp, and  $x_s(y, t)$  represents the equation of the reflected shock. The geometric derivatives  $\eta_x$ ,  $\eta_y$ ,  $\eta_t$ ,  $\xi_x$ ,  $\xi_y$ , and  $\xi_t$  corresponding to the transformation above are used in Equation (1). They are derived in Appendix A (see Equations (A13)).

The self-similar transformation to  $\eta$  and  $\xi$  reduces the unsteady gasdynamic equations in the Cartesian system (Equation (A1)), which are hyperbolic, to an equivalent steady set of mixed elliptic-hyperbolic

equations, that is, in the region between the wall and the sonic circle (see Figure 6a) they are elliptic, while above the sonic circle they are hyperbolic. The equations are made totally hyperbolic by reintroducing a time-like or residual term  $(U/J)_\tau$  which should approach zero as the solution converges. That is, the transformed Euler equations (Equation (1)), which are hyperbolic with respect to  $\tau$ , are solved using a time asymptotic approach. Because of the self-similarity of the problem, the term  $(U/J)_\tau$  approaches zero as  $\tau$  gets large thus establishing a convergence criterion.

#### Initial Conditions

The transformation given by Equation (2) results in the computational plane shown in Figure 6b. It is bounded by the reflected shock and outer boundary, both of which are permeable surfaces, and by the wall and the ramp. The region between the wall and the outer boundary is divided into  $(k_{\max} - 1)$  equal intervals and the region between the ramp and the reflected shock is divided into  $(j_{\max} - 1)$  equal intervals. The intersections of constant- $\eta$  and constant- $\xi$  lines generate the discrete computational grid used in the finite-difference formulation of the problem. Initial conditions (either in terms of flow variables or conservative variables) are to be specified at all grid points in order to initiate the integration of the transformed Equation (1) using MacCormack's (32) scheme (Appendix B).

To initialize the flow field at time  $\tau = 1$  given the incident shock Mach number  $M_s$  and ramp angle  $\theta_r$ , the pressure and density in region (1) (see Figure 6a) are first set equal to unity. The flow conditions in

region (2) which are used as the upstream conditions for the reflected shock are calculated from the following equations for a moving shock:

$$p_2 = p_1 \frac{2\gamma M_s^2 - (\gamma - 1)}{\gamma + 1} \quad (3)$$

$$\rho_2 = \rho_1 \left( \frac{\gamma + 1}{\gamma - 1} \frac{p_2}{p_1} + 1 \right) / \left( \frac{\gamma + 1}{\gamma - 1} + \frac{p_2}{p_1} \right) \quad (4)$$

$$u_2 = M_s \left[ 1 - \frac{(\gamma - 1)M_s^2 + 2}{(\gamma + 1)M_s^2} \right] \left( \frac{\gamma p_1}{\rho_1} \right)^{1/2} \quad (5)$$

$$v_2 = 0 \quad (6)$$

$$e_2 = \frac{p_2}{\gamma - 1} + \frac{\rho_2 u_2^2}{2} \quad (7)$$

The subscript 2 in the above equations refers to region (2). The position and the slope of the reflected shock along with the uniform flow conditions in region (3) (above the sonic circle in Figure 6a) are then determined from the equivalent steady, regular shock reflection equations. This procedure is outlined in Appendix C. The conditions in region (3) determine the position of the sonic circle at time  $\tau = 1$ . At all points along the sonic circle the self-similar velocity is sonic. That is,

$$\left( u_3 - \frac{x_{sc}}{\tau} \right)^2 + \left( v_3 - \frac{y_{sc}}{\tau} \right)^2 = a_3^2 = \frac{\gamma p_3}{\rho_3} \quad (8)$$

where  $u_3$ ,  $v_3$ , and  $a_3$  are known in the uniform flow region (3).

Solving Equation (8) gives the ordinate ( $x_{sc}$ ,  $y_{sc}$ ) of any point lying on the sonic circle. Now, the outer boundary is chosen such that it falls above the sonic circle but below the shock impingement point I (see

Figure 6a). Since the outer boundary lies in the uniform flow region (3), the conditions at grid points along this boundary are exactly known using the solution developed in Appendix C.

The intersection of the sonic circle with the reflected shock is determined by simultaneously solving Equation (8) and the slope equation for the reflected shock in region (3). Between this intersection point (IP in Figure 6a) and the wall a cubic is used to approximate the reflected shock shape. Knowing the shock shape and assuming a self-similar flow, that is,  $x_{s_\tau} = x_s/\tau$  ( $x_{s_\tau}$  is the shock speed), the flow variables behind the reflected shock are given by the following equations, which include the Rankine-Hugoniot relations:

$$\vec{n}_s = \frac{\hat{i} - x_{s_y} \hat{j}}{\sqrt{1 + x_{s_y}^2}} \quad (9)$$

$$\vec{q}_2 = u_2 \hat{i} + v_2 \hat{j} \quad (10)$$

$$\tilde{u}_2 = \vec{q}_2 \cdot \vec{n}_s = \frac{u_2}{\sqrt{1 + x_{s_y}^2}} \quad (11)$$

$$a_2 = \sqrt{\gamma p_2 / \rho_2} \quad (12)$$

$$x_{s_\tau} = x_{s_t} + x_{s_y} y_\tau \quad (13)$$

$$x_{s_t} = q_s / \cos \beta \quad (14)$$

$$\beta = \tan^{-1} x_{s_y} \quad (15)$$

$$x_{s_y} = x_{s_\xi} \xi_y \quad (16)$$

$$M_x = \frac{\tilde{u}_2 - q_s}{a_2} \quad (17)$$

$$\frac{p_s}{p_2} = \frac{2\gamma M_x^2 - (\gamma - 1)}{\gamma + 1} \quad (18)$$

$$\frac{\rho_s}{\rho_2} = \frac{(\gamma + 1)M_x^2}{(\gamma - 1)M_x^2 + 2} \quad (19)$$

$$M_y = \frac{\tilde{u}_s - q_s}{a_s} = \left[ \frac{(\gamma - 1)M_x^2 + 2}{2\gamma M_x^2 - (\gamma - 1)} \right]^{1/2} \quad (20)$$

$$a_s = \sqrt{\gamma p_s / \rho_s} \quad (21)$$

$$u_s = u_2 + \frac{(\tilde{u}_s - \tilde{u}_2)}{\sqrt{1 + x_{s_y}^2}} \quad (22)$$

$$v_s = - \frac{(\tilde{u}_s - \tilde{u}_2)x_{s_y}}{\sqrt{1 + x_{s_y}^2}} \quad (23)$$

$$e_s = \frac{p_s}{\gamma - 1} + \frac{\rho_s(u_s^2 + v_s^2)}{2} \quad (24)$$

where  $\vec{n}_s$  is the inward normal,  $\vec{q}_s$  is the velocity of the shock in its normal direction (see Figure 7),  $\tilde{u}_2$  is the velocity of the flow in the direction normal to the shock in region (2),  $x_{s_\tau}$  is the shock speed in the computational plane,  $x_{s_t}$  is the shock speed in the physical plane, and  $x_{s_y}$  is the shock slope. The quantity  $x_{s_\xi}$  in Equation (16) is



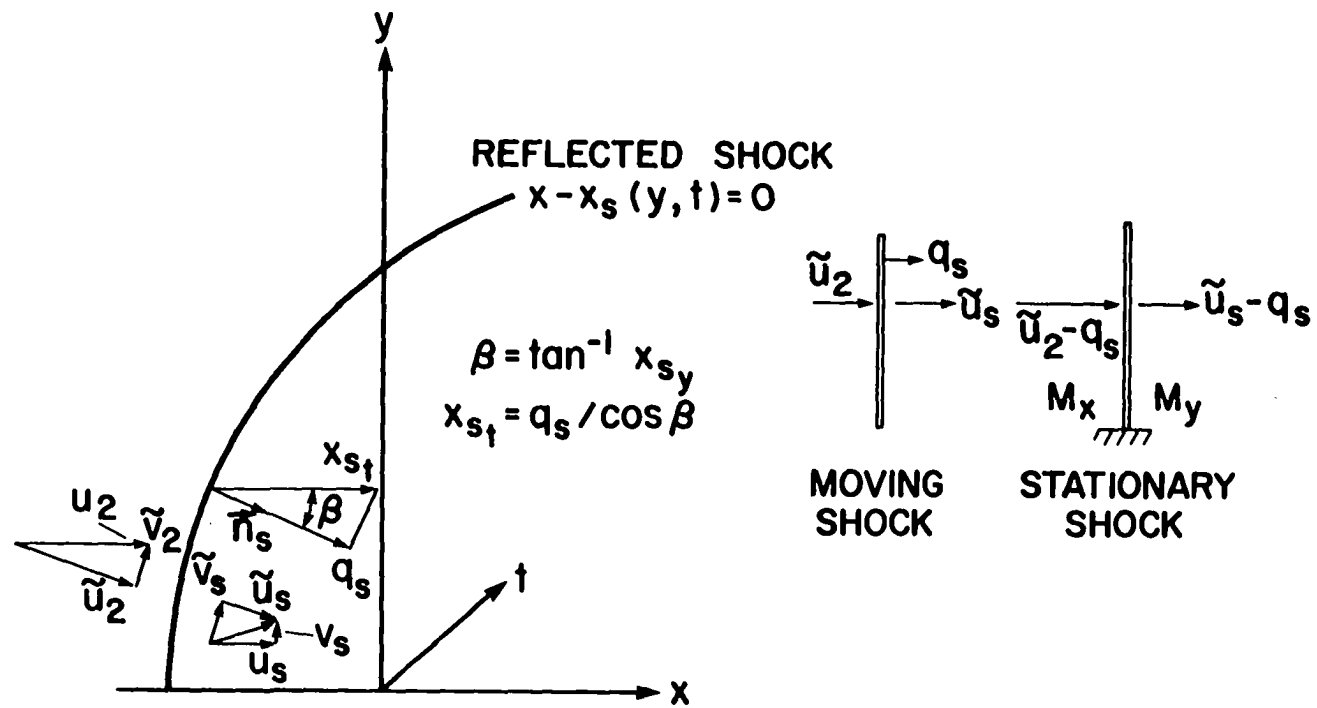


Figure 7. Shock propagation in unsteady flow

determined numerically using a second-order central difference formula.

The subscript  $s$  refers to flow conditions behind the reflected shock.

To initialize the flow field between the ramp and the reflected shock, the conditions at the stagnation point (point 0 in Figure 6a) are first computed based on the flow conditions behind the normal part of the reflected shock (point A in Figure 6a).

$$u_o = 0 \quad (25)$$

$$v_o = 0 \quad (26)$$

$$\frac{p_o}{p_A} = \left(1 + \frac{\gamma - 1}{2} M_A^2\right)^{\frac{\gamma}{\gamma - 1}} \quad (27)$$

$$\frac{\rho_o}{\rho_A} = \left(1 + \frac{\gamma - 1}{2} M_A^2\right)^{\frac{1}{\gamma - 1}} \quad (28)$$

$$e_o = \frac{p_o}{\gamma - 1} \quad (29)$$

$$s_o = s_A = \frac{p_o}{\rho_o \gamma} \quad (30)$$

$$M_A = \sqrt{\frac{u_A^2 + v_A^2}{\gamma p_A / \rho_A}} \quad (31)$$

Along the ramp between the stagnation point and the sonic circle, a parabolic approximation of the flow variables is assumed. The field points ( $1 < k < k_{\max}$ ,  $1 < j < j_{\max}$ ) are then initialized by a linear interpolation of the flow variables at the ramp and the reflected shock. Based on the

initial flow field, conservative variables  $U, E, F$ , and the geometric derivatives  $\eta_t, \eta_x, \eta_y, \xi_t, \xi_x$ , and  $\xi_y$  that are needed in Equation (1), are formulated and stored at each of the grid points.

Starting with this initialized flow field, Equation (1) is integrated (subject to certain boundary conditions discussed in the next section) using the explicit, second-order, predictor-corrector MacCormack's (32) scheme. Using a one-dimensional, amplification matrix, stability analysis (34) of MacCormack's scheme, a governing integration step size is obtained. The integration procedure and step size calculations are presented in Appendix B.

### Boundary Conditions

The computational region is bounded by the reflected shock and the outer boundary, both of which are permeable surfaces, and by the wall and the ramp, both of which are impermeable surfaces. The boundary condition procedures applied at each of these surfaces are discussed below.

#### Reflected shock

The position and the shape of the reflected shock wave are determined at each step of the time-asymptotic, integration procedure. The variables  $x_s, x_{s_y}$ , and  $x_{s_t}$  which appear in the conservative variables of Equation (1) along with the flow variables at the shock can be determined by employing an unsteady variation of the Thomas' "pressure approach" (27,28) for propagating shock waves. In this approach, it is only necessary to know the pressure behind the shock in order to alter its position for the next time level. The required pressure is obtained by

using the normal field point predictor-corrector algorithm at the shock but with one-sided differences away from the shock or in the  $\eta$ -direction. The shock speed (see Figure 7) and remaining flow variables are given by the following equations, which include the Rankine-Hugoniot relations:

$$M_x = \left\{ \frac{1}{2\gamma} \left[ \frac{p_s}{p_2} (\gamma + 1) + (\gamma - 1) \right] \right\}^{1/2} \quad (32)$$

$$\tilde{u}_2 = \frac{u_2}{\sqrt{1 + x_{s_y}^2}} \quad (33)$$

$$x_{s_y} = x_{s_\xi} \xi_y \quad (34)$$

$$a_2 = \sqrt{\gamma p_2 / \rho_2} \quad (35)$$

$$q_s = \tilde{u}_2 - a_2 M_x \quad (36)$$

$$x_{s_t} = \frac{q_s}{\cos \beta} \quad (37)$$

$$\beta = \tan^{-1} x_{s_y} \quad (38)$$

$$\rho_s = \rho_2 \left[ \frac{(\gamma + 1) M_x^2}{(\gamma - 1) M_x^2 + 2} \right] \quad (39)$$

$$\tilde{u}_s = q_s + M_y a_s \quad (40)$$

$$a_s = \sqrt{\gamma p_s / \rho_s} \quad (41)$$

$$M_y = \left[ \frac{(\gamma - 1) M_x^2 + 2}{2\gamma M_x^2 - (\gamma - 1)} \right]^{1/2} \quad (42)$$

$$u_s = u_2 + \frac{\tilde{u}_s - \tilde{u}_2}{\sqrt{1 + x_{s_y}^2}} \quad (43)$$

$$v_s = - \frac{(\tilde{u}_s - \tilde{u}_2)x_{s_y}}{\sqrt{1 + x_{s_y}^2}} \quad (44)$$

$$e_s = \frac{p_s}{\gamma - 1} + \rho_s \frac{u_s^2 + v_s^2}{2} \quad (45)$$

The quantity  $x_{s_\xi}$  in Equation (34) is determined numerically using a second-order central difference formula. The subscript 2 refers to flow conditions in the uniform region (2) and the subscript s refers to flow conditions behind the reflected shock (along  $k=k_{\max}$  in Figure 6a).

The actual propagation of the shock wave in the numerical procedure is accomplished by using a second-order Euler predictor/modified Euler corrector

$$\tilde{x}_s^{n+1} = x_s^n + x_{s_\tau}^n \Delta\tau ; \quad \text{predictor} \quad (46)$$

$$x_s^{n+1} = x_s^n + \frac{1}{2} \left( x_{s_\tau}^n + \tilde{x}_{s_\tau}^{n+1} \right) \Delta\tau ; \quad \text{corrector} \quad (47)$$

where

$$x_{s_\tau} = x_{s_t} + x_{s_y} y_\tau \quad (48)$$

The integration step size  $\Delta\tau$  is obtained from a stability analysis described in Appendix B.

The above equations are used in the following manner:

Initially at time step  $n$  all flow variables at the shock are known including the shock speed and the shape. The pressure behind the shock is predicted using the first step of MacCormack's scheme. The shock wave is then moved using Equation (46). The predicted position permits the shock derivatives  $x_{s_y}$  to be computed from Equation (34). The shock speed, and other flow variables are then calculated from Equations (32)-(45). The same procedure is followed in the corrector step except that the second step of MacCormack's scheme is used to get the pressure behind the shock and Equation (47) is used to correct the shock position.

#### Impermeable boundaries

The impermeable boundaries in the shock diffraction problem consist of the wall surface and the ramp surface. Each of these surfaces is aligned with a constant coordinate line as a result of the self-similar, normalizing transformation. Because of this alignment, and the fact that the flow must be tangent to these boundaries, the only variable required at the body to advance the field points using Equation (1) is the pressure. However, determination of the remaining flow variables and the position of the vortical singularity on the ramp is essential in computing the correct surface pressure. Discussed below are two different boundary condition procedures that were tested for satisfying the tangency condition and determining the flow variables along the wall and the ramp.

In the first, a simple Euler predictor/modified Euler corrector with one-sided  $\xi$ -derivatives at the wall and  $\eta$ -derivatives at the ramp for Equation (1) is used. The tangency condition itself, that is,  $v = 0$  at

the wall and  $v = u \tan \theta_r$  along the ramp, is imposed after the corrector step. Having determined the velocity components from this procedure, the self-similar velocities  $u-x/t$  and  $v-y/t$  are used to locate the vortical singularity by noting at what point along the ramp they are identically zero. Knowing this location, the appropriate entropy levels are assigned to the surface grid points. As mentioned in the Introduction, the level of entropy at grid points along the wall and on the ramp up to the vortical singularity is equal to that behind the normal part of the reflected shock, while the level of entropy at grid points between the vortical singularity and the incident shock impingement point is equal that behind the straight part of the reflected shock. The corresponding body density is obtained from the following expression by using the pressure computed by the one-sided finite-difference scheme:

$$\rho = \left( \frac{p}{s} \right)^{1/\gamma} \quad (49)$$

where  $s$  is an appropriate measure of entropy level. The total energy  $e$  is then recomputed from

$$e = \frac{p}{\gamma - 1} + \rho \frac{u^2 + v^2}{2} \quad (50)$$

The second boundary condition procedure tested was that of Kentzer (35). It is based on a method of characteristics approach in combination with one-sided finite-differences. Here, the goal is to derive an expression for  $p_\tau$  and  $u_\tau$  valid at the impermeable boundary grid points which can be integrated to obtain the surface pressure and the  $u$ -component of velocity. This procedure is well outlined in Appendix D. Having the

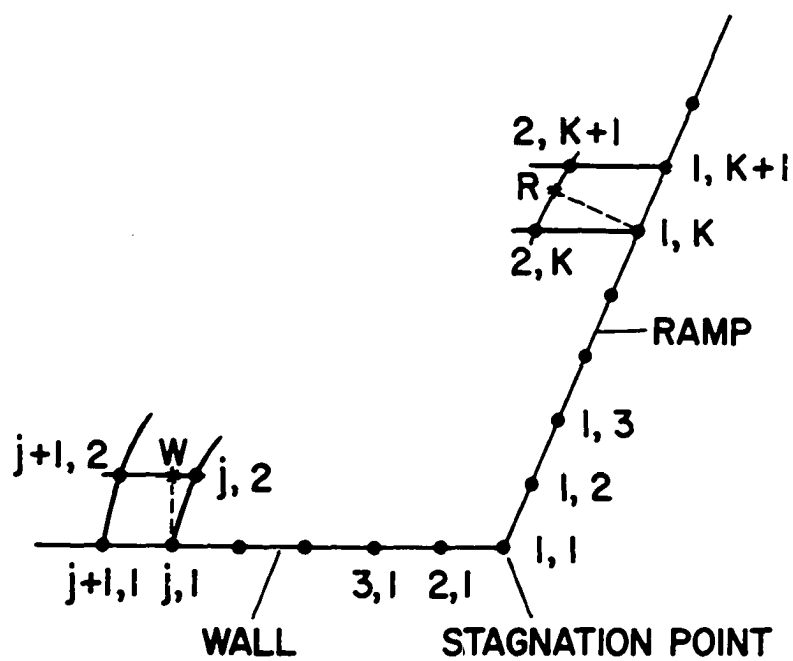
u-velocity component, the v-velocity component is computed from the surface tangency condition. The self-similar velocities, position of the vortical singularity, and the body density are computed in the same way as described for the previous boundary condition procedure.

Using the self-similar property of the flow field in conjunction with the surface tangency condition, it can be shown from the normal momentum equation that  $\partial p / \partial n$  (where  $n$  is the direction normal to each surface) is zero at the wall and ramp surfaces. Neither Kentzer's scheme nor the Euler predictor/modified Euler corrector method satisfy this condition exactly because of the approximate one-sided, finite-differences involved. Therefore, after the converged solution is obtained using either of the above boundary condition procedures, the pressure at the body is recomputed after the corrector step to satisfy  $\partial p / \partial n = 0$ . This is done in the following manner. First, the surface normal is drawn and its intersection with the first grid line above is found (point R or W in Figure 8). The pressure at the intersection point ( $p_W$  or  $p_R$ ) is then obtained from a simple linear interpolation of the data at two neighboring grid points. A simple first-order extrapolation of the form

$$\left. \begin{aligned} p_{1,k} &= p_R \\ p_{j,1} &= p_W \end{aligned} \right\} \quad (51)$$

satisfies  $\partial p / \partial n = 0$  to the zeroth order. At the stagnation point both  $p_\eta$  and  $p_\xi$  are zero. Making use of this condition, the pressure at the stagnation point is obtained by taking an average of the two extrapolated pressures, one along the wall and the other along the ramp.





$$p_{1, K} = p_R$$

$$p_{j, 1} = p_W$$

$$p_{1, 1} = 1/2 \left\{ \frac{(4p_{2,1} - p_{3,1})}{3} + \frac{(4p_{1,2} - p_{1,3})}{3} \right\}$$

Figure 8. Procedure for imposing  $\partial p / \partial n = 0$

$$p_{1,1} = \frac{1}{2} \left( \frac{4p_{2,1} - p_{3,1}}{3} + \frac{4p_{1,2} - p_{1,3}}{3} \right) \quad (52)$$

A comparison of the different boundary condition schemes is presented in the Result section.

#### Outer boundary

The outer boundary (see Figure 6a) is positioned beyond the sonic circle (defined by Equation (8)) so that the flow conditions are supersonic along it. This allows flow conditions along the outer boundary to be specified initially and held fixed during the entire integration procedure.

#### Results

The computational grid for a typical regular reflection case consisted of 11 points in the  $\eta$ -direction and 27 points in the  $\xi$ -direction. An average of 300 iteration was required to obtain a converged solution and these consumed approximately 15 minutes of computer time on an IBM 360/67.

Numerical results in the form of pressure and density contour plots are qualitatively compared with the first-order shock-capturing results of Rusanov (15) and Schneyer (22) in Figures 9 and 10, respectively. Rusanov's solution was obtained using Godunov's method for an incident shock Mach number of 1.89 impinging on a 65° ramp. Most of the contours which appear in Figure 9a lie within the captured shock wave, and very few describe the flow field between the ramp and reflected shock in comparison with the contours of Figure 9b.

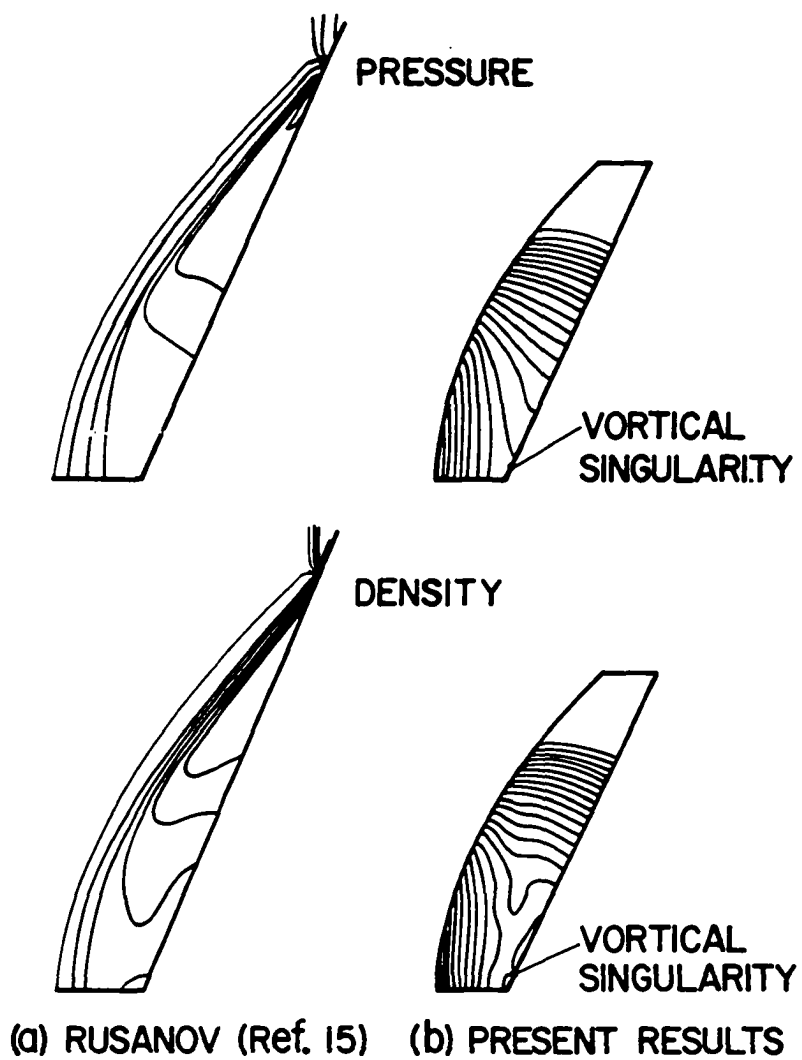


Figure 9. Comparison of numerically generated pressure contour plots.  
 $M_s = 1.89$ ,  $\theta_r = 65^\circ$

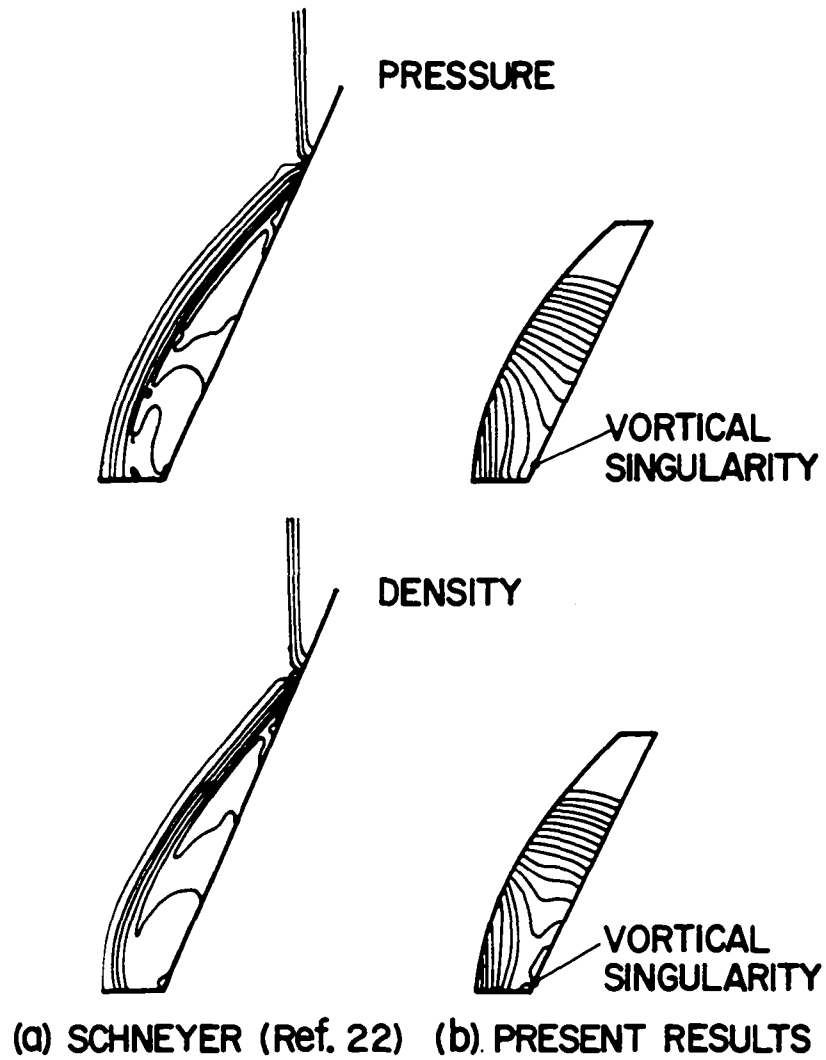


Figure 10. Comparison of numerically generated pressure contour plots.  
 $M_s = 2$ ,  $\theta_r = 63.41^\circ$

In studying the Mach reflection phenomenon, Schneyer (22) used a two-dimensional, Eulerian, hydrodynamic code to obtain the regular reflection result shown in Figure 10a. The incident shock Mach number was 2.0 and the ramp angle was  $63.41^\circ$ . His result exhibits the same qualitative behavior as does Rusanov's. The present result for the same case is shown in Figure 10b. The results of both Schneyer and Rusanov fail to reveal the presence of the vortical singularity.

Law (5) performed a series of experiments on the shock diffraction problem for various gases using a Mach-Zehnder interferogram. He tested a Mach 4.71 incident shock striking a  $60^\circ$  ramp in oxygen; the result was regular reflection. This case in addition to others at the same incident shock Mach number but for different ramp angles was obtained numerically to demonstrate the flow field behavior in the regular reflection regime. The results are presented in Figures 11-16.

The density and pressure distributions along the wall and the ramp are shown in Figure 11. At the stagnation point (point C of Figure 11), the density and pressure reach a local minimum, while at the vortical singularity (point D of Figure 11), the pressure is continuous and at a local minimum, and the density is discontinuous. A partial plot (see Figure 12) of the self-similar velocity along the ramp reveals the two self-similar stagnation points at A (junction of the wall and the ramp) and B (vortical singularity).

In Figure 13, results from the different body boundary condition procedures are compared. Both the Euler predictor/modified Euler corrector and Kentzer's scheme yield very nearly the same results. The

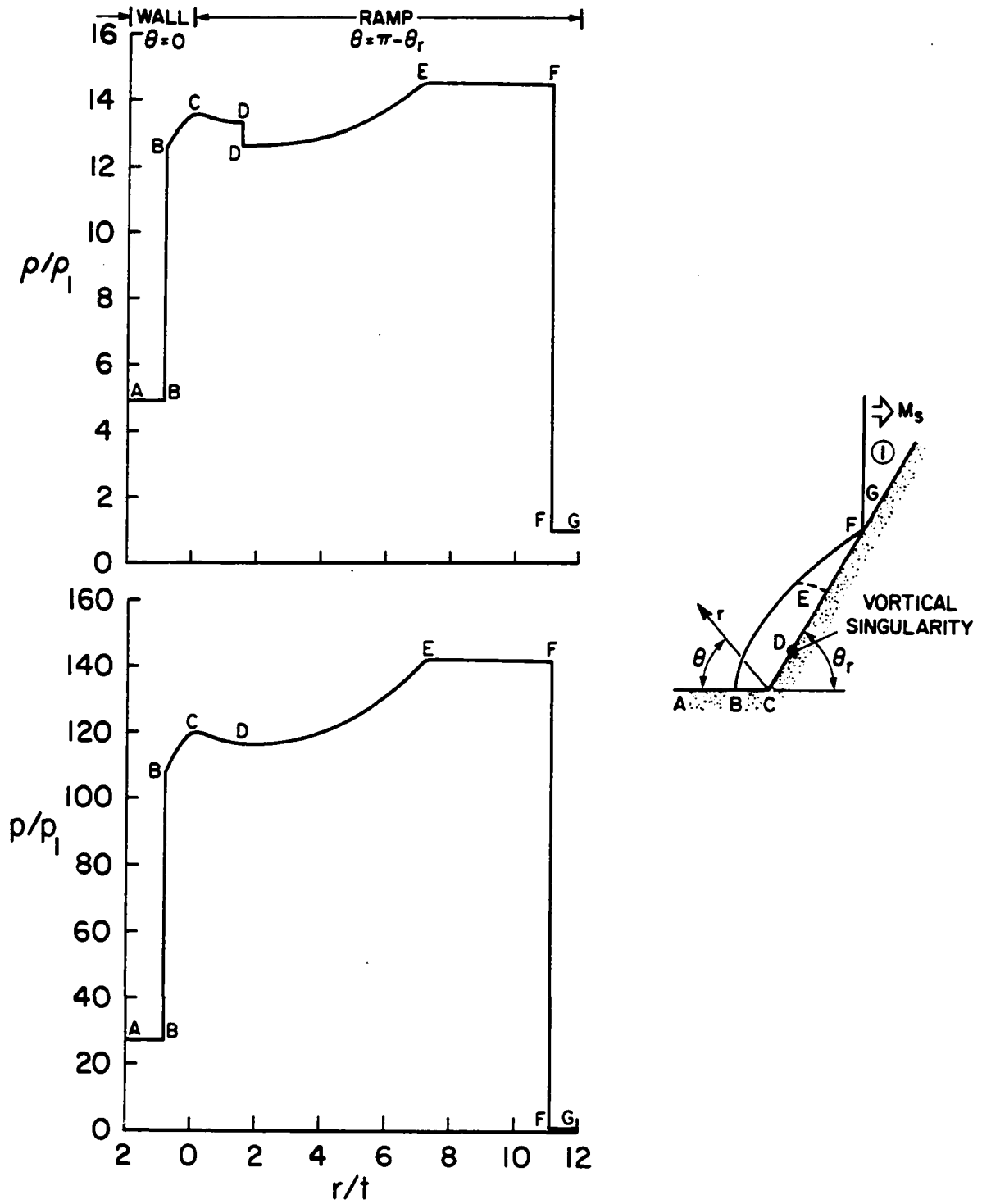


Figure 11. Surface density and pressure distribution along the wall and the ramp.  $M_s = 4.71$ ,  $\theta_r = 60^\circ$

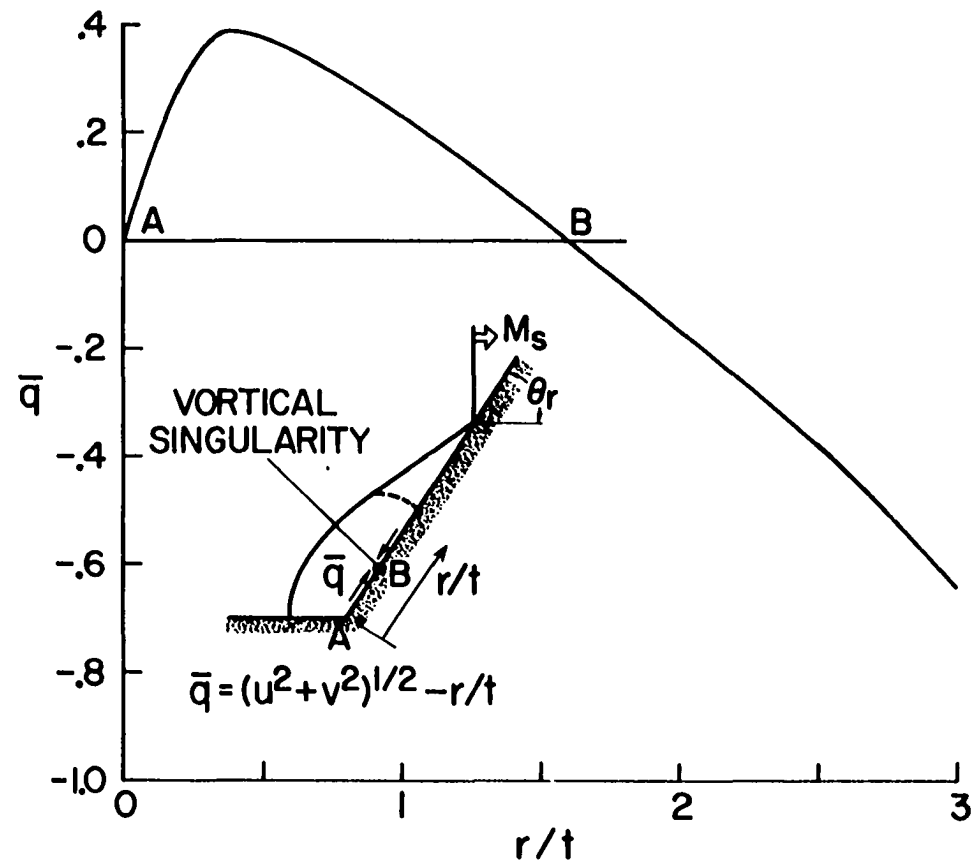


Figure 12. Self-similar surface velocity distribution.  $M_s = 4.71$ ,  $\theta_r = 60^\circ$

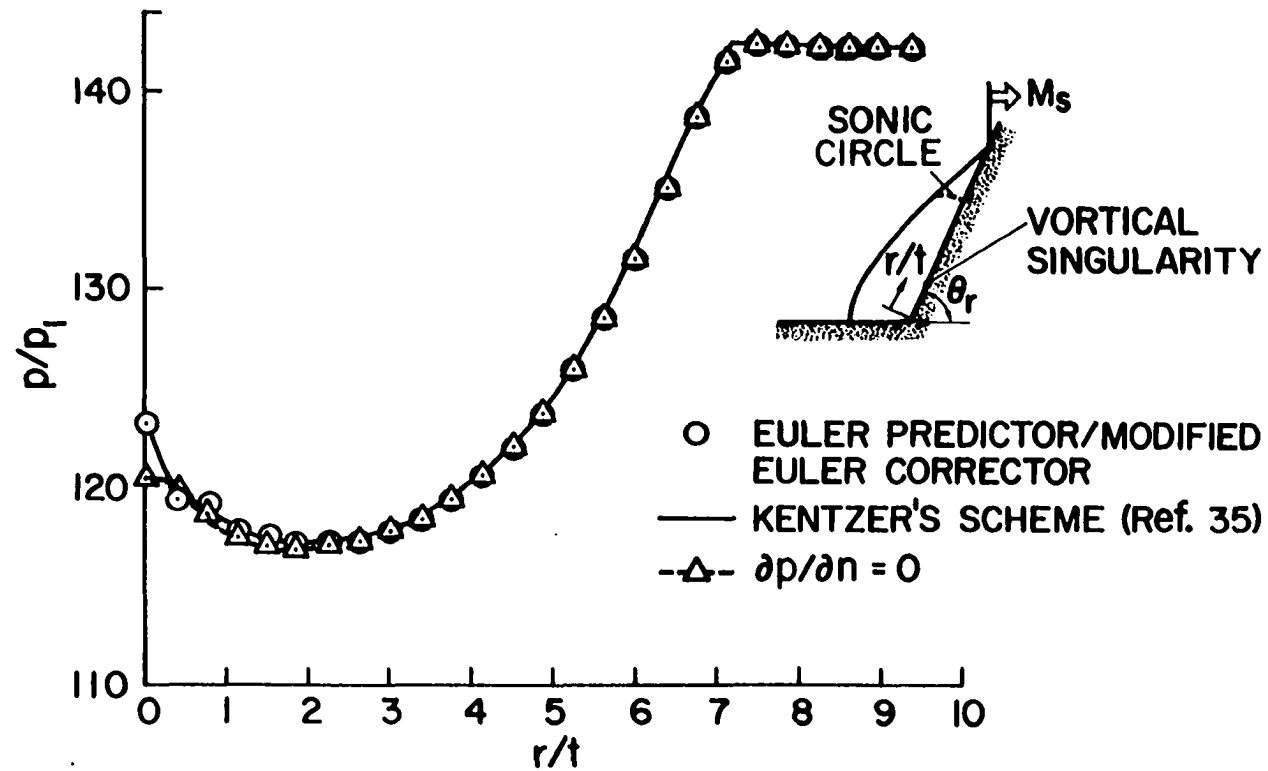


Figure 13. Comparison of ramp surface pressure distribution for different boundary condition procedures.  $M_g = 4.71$ ,  $\theta_r = 60^\circ$



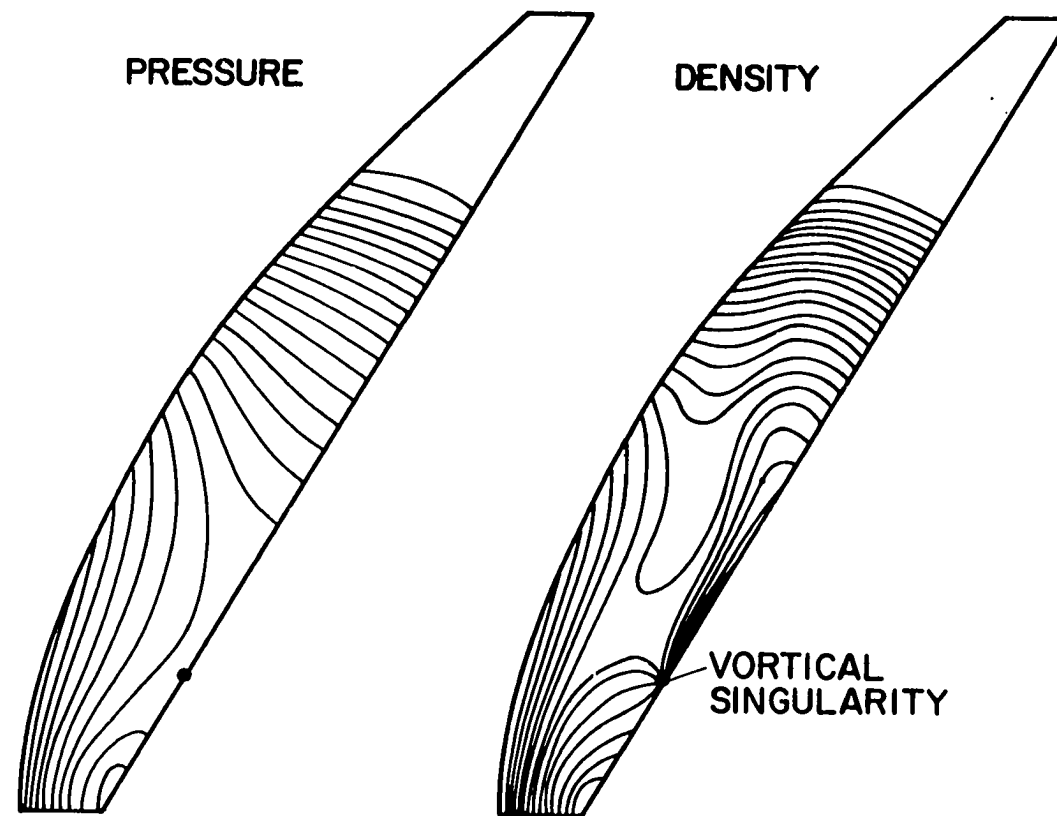


Figure 14. Pressure and density contour plots.  $M_s = 4.71$ ,  $\theta_r = 60^\circ$

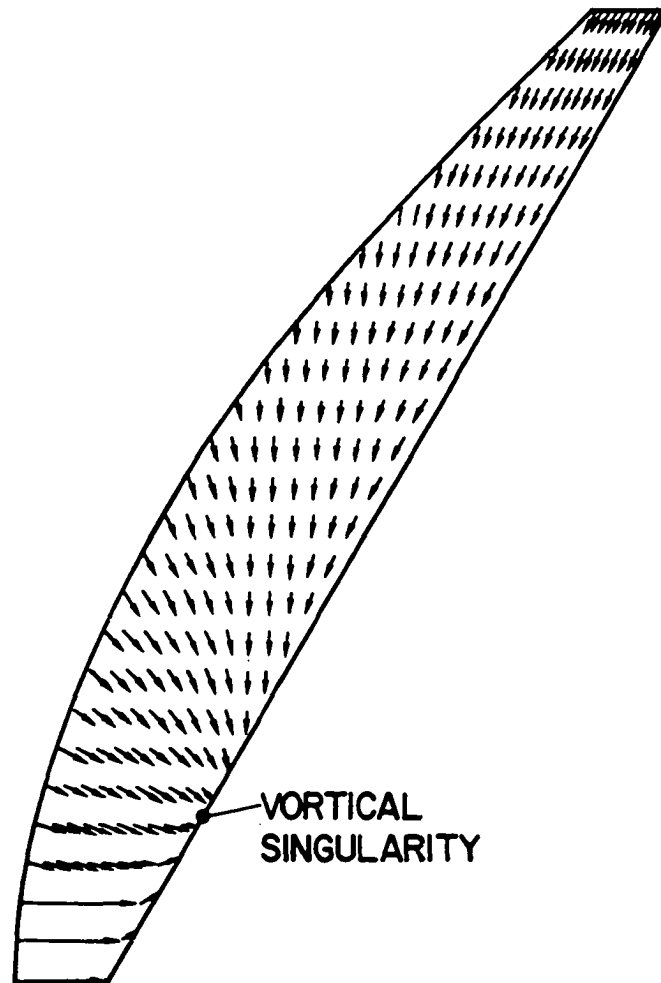


Figure 15. Self-similar velocity directional plot.  $M_s = 4.71$ ,  $\theta_r = 60^\circ$

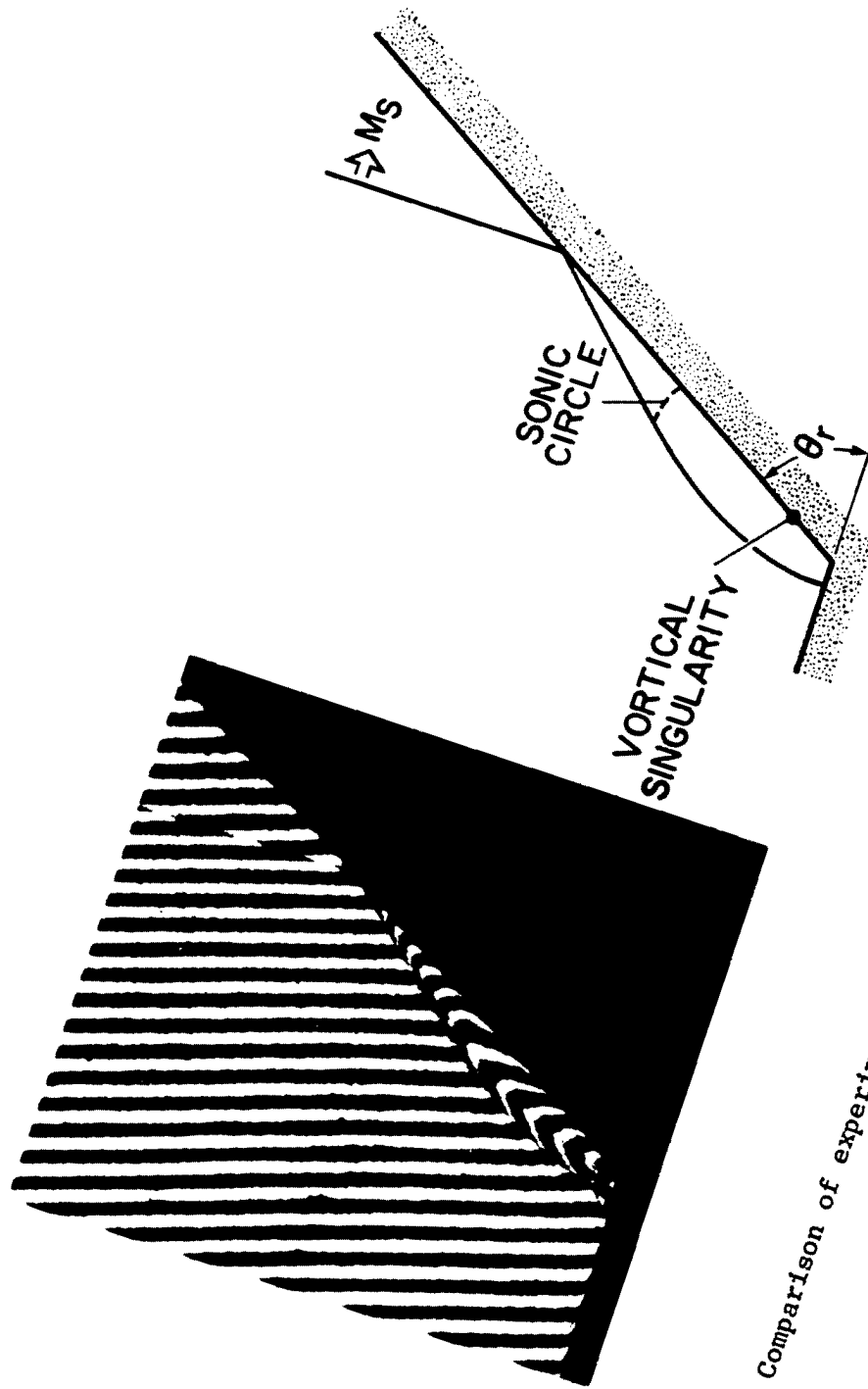


Figure 16. Comparison of experimental and computed shock positions.  $M_s = 4.71$ ,  $\theta_r = 60^\circ$

oscillations near the stagnation point are a result of the one-sided, finite-differences used in these schemes. Imposing  $\partial p / \partial n = 0$  seems to yield a much better solution without any oscillations in the flow variables near the stagnation point.

Pressure and density contour plots of these computational region are shown in Figure 14. The centerpoint of isobars near the wall-ramp intersection point, and the saddle point of isobars near the vortical singularity (for which moving away from the vortical singularity the pressure increases along the ramp and decreases perpendicular to the ramp) can be clearly observed in the figure. In the density contour plot, the convergence of the various isopycnics at the vortical singularity can be observed. The behavior of the flow near the stagnation points in this unsteady two-dimensional self-similar problem exhibits the same behavior as the steady, self-similar, three-dimensional flow about an external axial corner (36).

The self-similar streamline pattern can be visualized by observing the velocity vector directional plot of the computational plane shown in Figure 15. Notice that all the streamline converge at the vortical singularity.

A comparison of the interferogram obtained by Law (5) with the numerically computed shock shape is shown in Figure 16. If an overlay of the two results were made by matching shock impingement points, the experimental shock location would fall inside the numerical solution. The reason for the discrepancy is probably twofold: First, the viscous effects (the majority of which can be observed near the wall-ramp

intersection point) might have the effect of decreasing the ramp angle as a result of the boundary layer growth with distance from the shock impingement point. The reduced ramp angle in turn results in a smaller shock standoff distance. Second, the computed solution assumes flow of an ideal gas ( $\gamma = 1.4$ ). Thus, high temperature effects on the internal energy such as molecular, vibrational excitation are not taken into account.

The effect of varying the ramp angle for a given shock Mach number of 4.71 on the shock standoff distance ( $r_{so}$ ), position of the vortical singularity ( $r_{vs}$ ), location of the sonic circle ( $r_{sc}$ ), and shock impingement point ( $r_i$ ) are shown in Figure 17. The standoff distance exhibits almost a linear variation with ramp angle between the limit for regular reflection and the last computed case of  $\theta_r = 85^\circ$ . The vortical singularity moves towards the wall with increasing ramp angle and actually attaches itself to the wall for values of  $\theta_r$  greater than  $77^\circ$ . The location of the sonic circle along the ramp, and the shock impingement point are identical at the limit for regular reflection. As  $\theta_r$  increases the sonic circle moves toward the wall while the impingement point moves away from the wall.

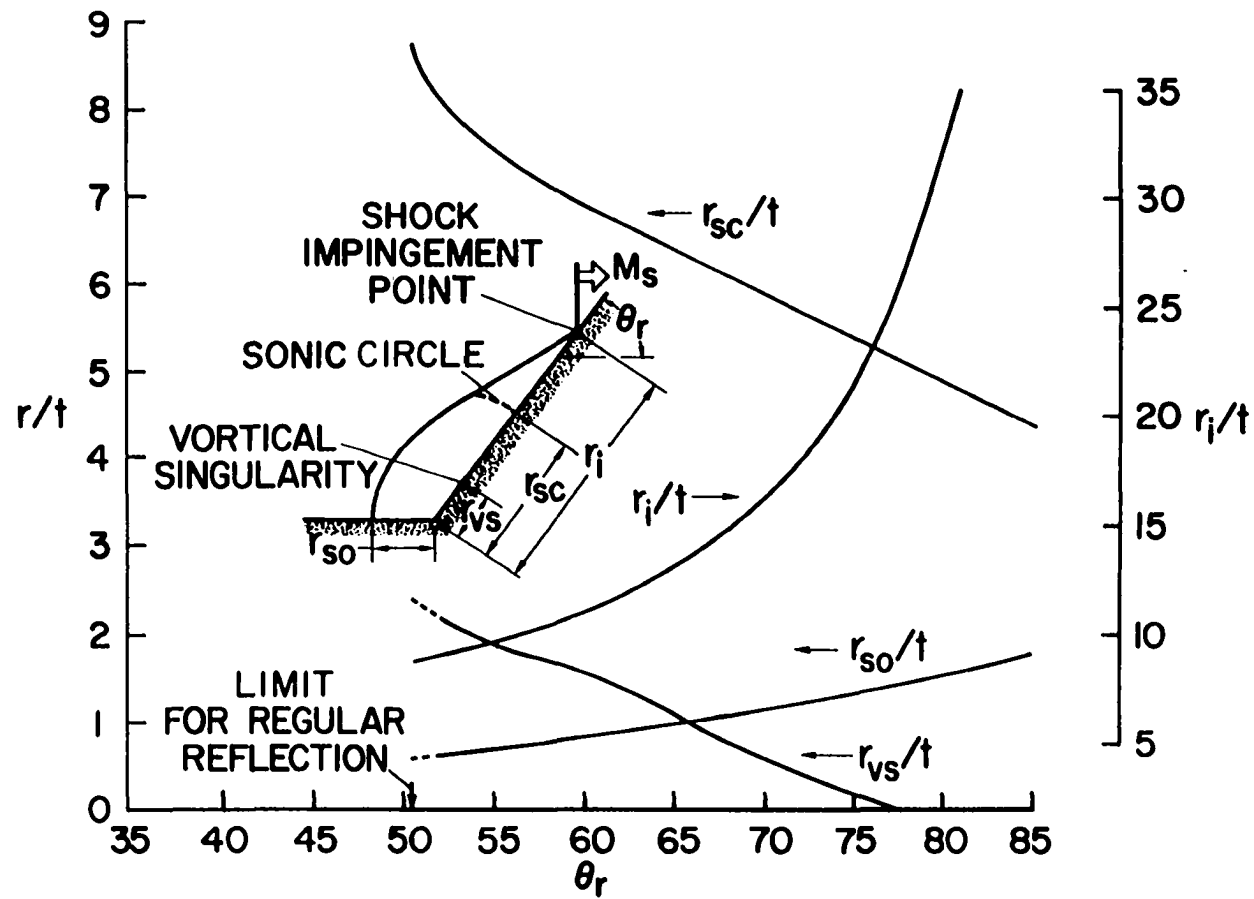


Figure 17. Variations of geometrical variables with ramp angle.  $M_8 = 4.71$

## CHAPTER III. SINGLE MACH REFLECTION

A typical single Mach reflection of an incident shock is shown in Figure 18. The self-similar flow field is somewhat complicated in this case by the existence of a triple point at which the reflected shock, the Mach stem and the incident shock meet. Emanating from the triple point is a slip surface which intersects the ramp at the vortical singularity. In Figure 18,  $M_{ss}$  denotes the self-similar Mach number. A sonic line exists in most of the single Mach reflection cases in the region between the reflected shock and the slip surface. Below this sonic line (region I in Figure 18) and in the region between the Mach stem and the slip surface (region III) the self-similar Mach number is subsonic ( $M_{ss} < 1$ ), while above the sonic line (region II) it is supersonic ( $M_{ss} > 1$ ).

In this problem, there are two self-similar stagnation points, that is, points at which the self-similar velocity components  $u-x/t$  and  $v-y/t$  are zero; the first is located at the juncture of the wall and the ramp (saddle point), and the second, termed a vortical singularity, is located at the point where the slip surface meets the ramp (nodal singularity). All the self-similar streamlines converge at the vortical singularity and the entropy is multivalued. The value of entropy on the stagnation streamline and along the ramp up to the vortical singularity is equal to that behind the normal part of the reflected shock, while the entropy between the vortical singularity and the Mach foot is the same as that behind the foot of the Mach stem.

In the present work, the reflected shock and the Mach stem (including the triple point) are fitted using the "sharp shock" (27,33) technique.

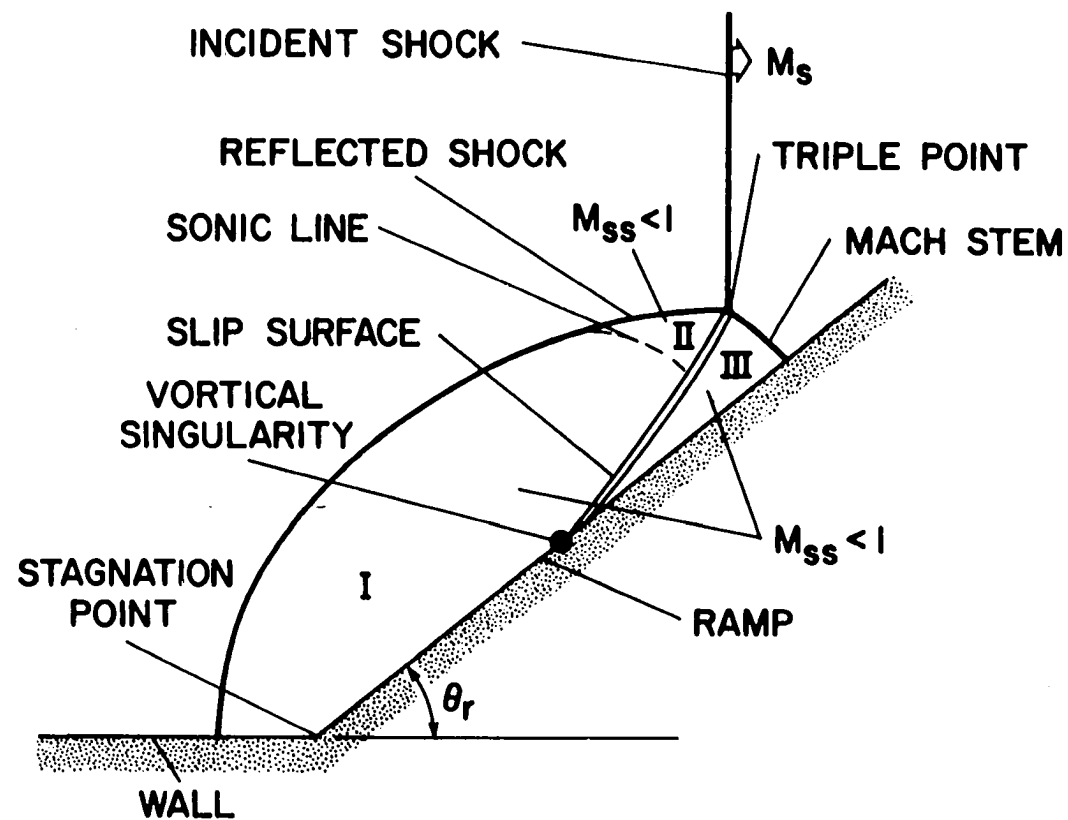


Figure 18. Single Mach reflection of the incident planar shock



A floating discontinuity-fitting scheme in conjunction with the method of characteristics is developed to fit the slip surface.

#### Double Normalization Procedure

A Cartesian coordinate system is used in the problem formulation with the origin located at the juncture of the wall and the ramp. The x-axis is aligned with the wall and the y-axis is normal to the wall (Figure 19a). The gasdynamic equations in this Cartesian system are given by Equation (A1) for the assumptions stated in Appendix A.

In order to apply the "sharp shock" technique, the reflected shock and the Mach stem are used as computational boundaries. This is done by means of a double normalizing transformation. The following functions are used for  $\tau$ ,  $\eta$ , and  $\xi$  which include the self-similarity of the problem, a normalization of the distance between the ramp and the reflected shock and a normalization of the distance between the wall and the Mach stem:

$$\left. \begin{aligned} \tau &= t \\ \eta &= \frac{x - X_b(\xi, \tau)}{X_s(\xi, \tau) - X_b(\xi, \tau)} \\ \xi &= \frac{y}{Y_s(\eta, \tau)} \end{aligned} \right\} \quad (53)$$

where  $X_b(\xi, \tau)$  represents the equation of the ramp,  $X_s(\xi, \tau)$  represents the equation of the reflected shock and  $Y_s(\eta, \tau)$  represents the equation of the Mach stem. Note that the ramp and the shock shapes are defined in terms of the computational variables  $\eta$ ,  $\xi$ , and  $\tau$  and not in terms of  $x$ ,  $y$ , and  $t$ . From Figure 19a it can be seen that such a representation

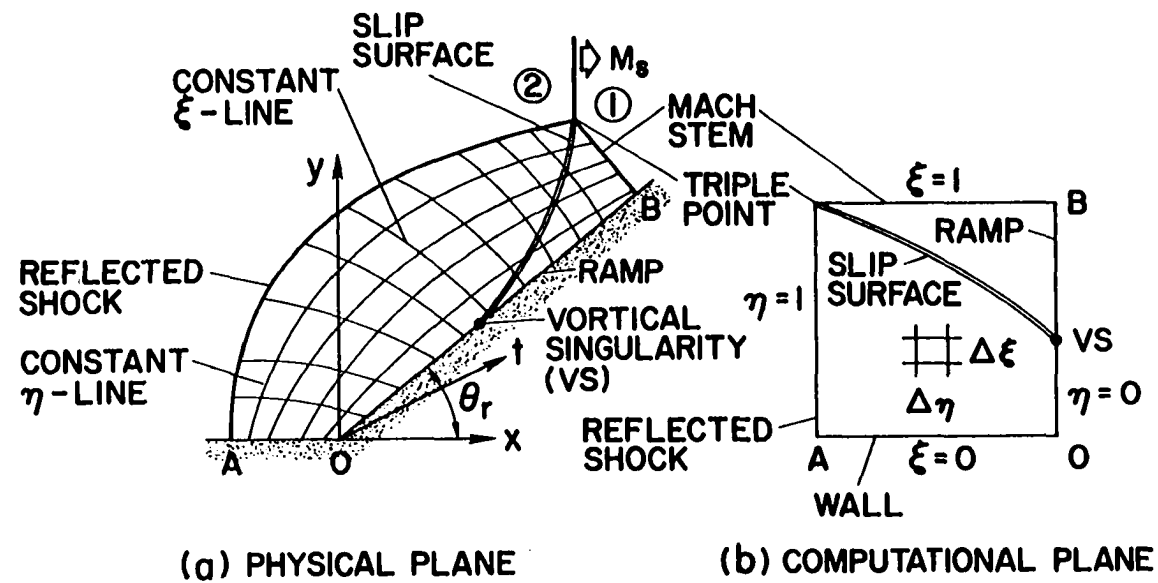


Figure 19. Coordinate system and the computational plane

is necessary because constant  $\eta$  and constant  $\xi$  lines are not parallel to the Cartesian  $x$  and  $y$  axis, respectively.

The equations corresponding to the independent variables  $\tau$ ,  $\eta$ , and  $\xi$  are given by Equation (1) in strong conservation-law form. The geometric derivatives  $\eta_t$ ,  $\eta_x$ ,  $\eta_y$ ,  $\xi_t$ ,  $\xi_x$ , and  $\xi_y$  appearing in this equation are derived in Appendix A (see Equations (A15) and (A16)).

The self-similar transformation to  $\eta$  and  $\xi$  reduces the unsteady gasdynamic equations in  $x$ ,  $y$ , and  $t$  system, which are hyperbolic, to an equivalent steady set of mixed elliptic-hyperbolic equations; they are elliptic in regions of subsonic self-similar velocity ( $M_{ss} < 1$ ) and hyperbolic in regions of supersonic self-similar velocity ( $M_{ss} > 1$ ). The equations are made totally hyperbolic by reintroducing a time-like or residual term  $((U/J)_\tau)$ . Because of the self-similar nature of the flow field this time-like term should approach zero in the converged solution.

#### Initial Conditions

The transformation given by Equation (53) results in the computational plane shown in Figure 19b. It is bounded by the reflected shock and the Mach stem, both of which are permeable boundaries, and by the wall and the ramp. The coordinate  $\eta$ , is zero at the ramp and equal to one at the reflected shock. Similarly  $\xi$  is zero at the wall and equal to one at the Mach stem. The slip surface floats within the mesh generated by the double normalization (Figure 19a). The region between the ramp and the reflected shock is divided into  $(j_{\max} - 1)$  equal intervals and the region between the wall and the Mach stem is divided into  $(k_{\max} - 1)$  equal intervals. This determines the mesh spacings  $\Delta\eta$  and  $\Delta\xi$ . The

intersections of constant  $\eta$  and constant  $\xi$  lines generate the discrete computational grid used in the finite-difference formulation of the problem. Initial conditions are specified at all grid points in order to initiate the integration of the transformed Equation (1) using MacCormack's (32) scheme (see Appendix B).

To initialize the flow field at time  $\tau = 1$  given the incident shock Mach number  $M_s$  and the ramp angle  $\theta_r$ , the pressure and the density in region (1) (see Figure 20) are first set equal to unity. The flow conditions in region (2), which are used as the upstream conditions for the reflected shock are calculated from Equations (3) to (7). Referring to Figure 20, an initial value for the triple point trajectory angle ( $\chi$ ) is assumed. Corresponding to this assumed value of  $\chi$ , the triple point solution is computed from an equivalent steady approach described in Appendix E. This gives the flow conditions at points 3 and 4 lying on either side of the slip surface at the triple point (see Figure 20). The reflected shock slope ( $\phi_R$ ), the Mach stem slope ( $\phi_M$ ) and the slip surface angle  $\alpha$  are also obtained from the triple point solution.

Assuming some standoff distance for the reflected shock (distance 0-A) at time  $\tau = 1$ , a cubic is used to approximate the reflected shock shape between the triple point and the wall. This cubic satisfies the conditions that the shock be normal to the wall at point A and the slope at the triple point be equal to that determined by the triple point solution ( $\tan \phi_R$ ). Similarly, assuming some value for the distance between the origin 0 and the Mach foot B, a cubic is used to approximate the Mach stem between the triple point and the ramp. This cubic satisfies the



conditions that the Mach stem be normal to the ramp at the foot and the slope at the triple point be equal to that determined by the triple point solution ( $\tan \phi_M$ ). The slip surface is initially approximated by a straight line with a slope  $\tan (90^\circ - \alpha)$ . This straight slip surface meets the ramp at the point denoted by VS in Figure 20.

Even though the double normalization requires that both the reflected shock and the Mach stem be represented in terms of the computational variables  $\eta$ ,  $\xi$ , and  $\tau$  the calculation of the flow variables behind them and their actual propagation requires a representation in terms of the physical variables  $x$ ,  $y$ , and  $t$ . The reflected shock is represented by

$$x = X_s(\xi, \tau) \equiv \bar{x}_s[y(\eta=1, \xi), t] \quad (54)$$

where  $\bar{x}_s(y, t)$  is the representation in terms of the physical variables. Similarly, the Mach stem is represented by

$$y = Y_s(\eta, \tau) \equiv \bar{y}_s[x(\xi=1, \eta), t]$$

where  $\bar{y}_s(x, t)$  is the representation in terms of the physical variables.

Knowing the initial reflected shock shape and assuming a self-similar flow, that is,

$$X_{s_\tau}(\xi, \tau) = \frac{X_s(\xi, \tau)}{\tau} \quad (55)$$

the flow variables behind the reflected shock are given by the following equations, which include the Rankine-Hugoniot relations (see Figure 21):

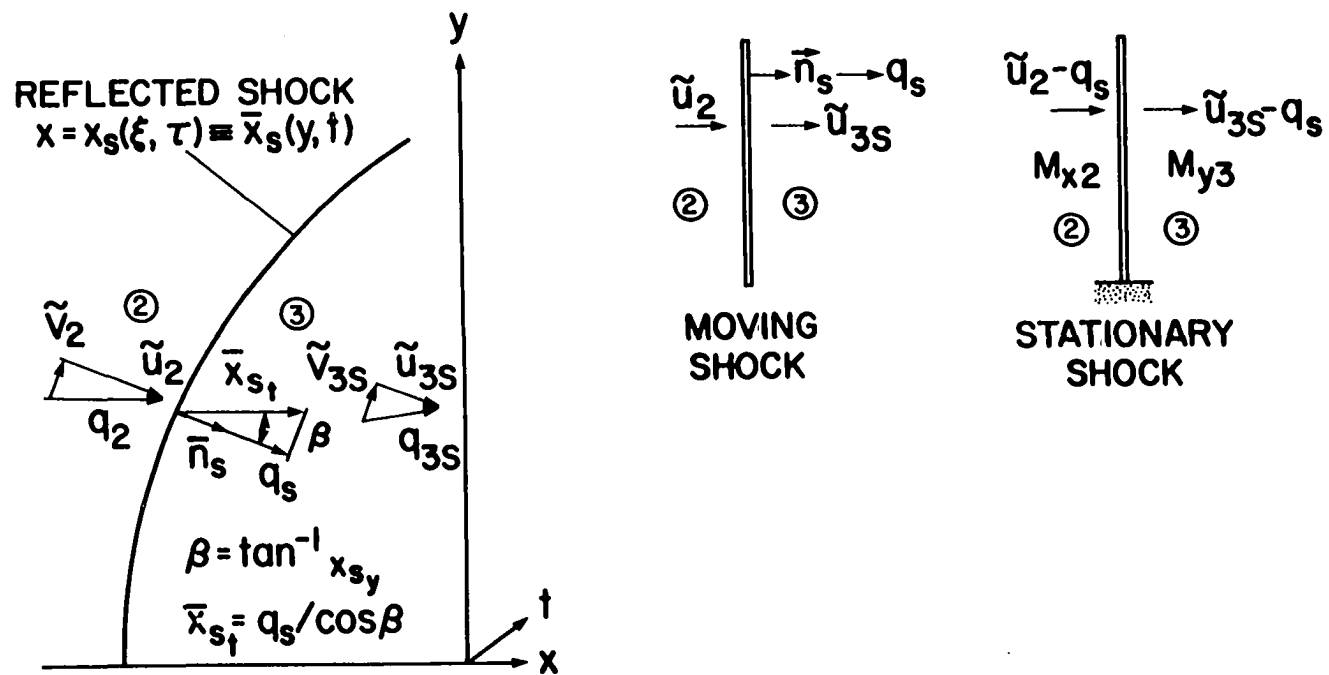


Figure 21. Reflected shock propagation in unsteady flow

$$\vec{n}_s = \frac{\hat{i} - \bar{x}_{sy} \hat{j}}{\sqrt{1 + \bar{x}_{sy}^2}} \quad (56)$$

$$\tilde{u}_2 = \vec{q}_2 \cdot \vec{n}_s = \frac{u_2}{\sqrt{1 + \bar{x}_{sy}^2}} \quad (57)$$

$$a_2 = \sqrt{\gamma p_2 / \rho_2} \quad (58)$$

$$X_{s_\tau}(\xi, \tau) = \bar{x}_{st} + \bar{x}_{sy} y_\tau = \frac{X_s(\xi, \tau)}{\tau} \quad (59)$$

$$q_s = \bar{x}_{st} \cos \beta \quad (60)$$

$$\bar{x}_{sy} = \frac{X_{s_\xi}(\xi, \tau)}{y_\xi} \quad (61)$$

$$\beta = \tan^{-1}(\bar{x}_{sy}) \quad (62)$$

$$M_{x2} = \frac{\tilde{u}_2 - q_s}{a_2} \quad (63)$$

$$\frac{p_{3s}}{p_2} = \frac{2\gamma M_{x2}^2 - (\gamma - 1)}{\gamma + 1} \quad (64)$$

$$\frac{\rho_{3s}}{\rho_2} = \frac{(\gamma + 1) M_{x2}^2}{(\gamma - 1) M_{x2}^2 + 2} \quad (65)$$



$$M_{y3} = \frac{\tilde{u}_{3s} - q_s}{a_{3s}} = \left[ \frac{(\gamma - 1)M_{x2}^2 + 2}{2\gamma M_x^2 - (\gamma - 1)} \right]^{1/2} \quad (66)$$

$$a_{3s} = \sqrt{\gamma p_{3s} / \rho_{3s}} \quad (67)$$

$$u_{3s} = u_2 + \frac{(\tilde{u}_{3s} - \tilde{u}_2)\bar{x}_{sy}}{\sqrt{1 + \bar{x}_{sy}^2}} \quad (68)$$

$$v_{3s} = - \frac{(\tilde{u}_{3s} - \tilde{u}_2)\bar{x}_{sy}}{\sqrt{1 + \bar{x}_{sy}^2}} \quad (69)$$

$$e_{3s} = \frac{p_{3s}}{\gamma - 1} + \frac{\rho_{3s}(u_{3s}^2 + v_{3s}^2)}{2} \quad (70)$$

where  $\vec{n}_s$  is the inward reflected shock normal,  $\vec{q}_s$  is the velocity of the shock in its normal direction,  $\tilde{u}_2$  is the velocity of the flow normal to the shock in region (2),  $X_{s\tau}$  is the shock speed in the computational plane,  $\bar{x}_{st}$  is the shock speed in the physical plane, and  $\bar{x}_{sy}$  is the shock slope. The quantity  $X_{s\xi}(\xi, \tau)$  appearing in Equation (61) is computed numerically using a second-order central difference formula. The subscript 3s refers to flow conditions behind the reflected shock (along  $\eta = 1$  in Figure 19b).

The flow conditions behind the Mach stem are computed in a similar fashion knowing the initial shape and assuming a self-similar flow (see Figure 22).

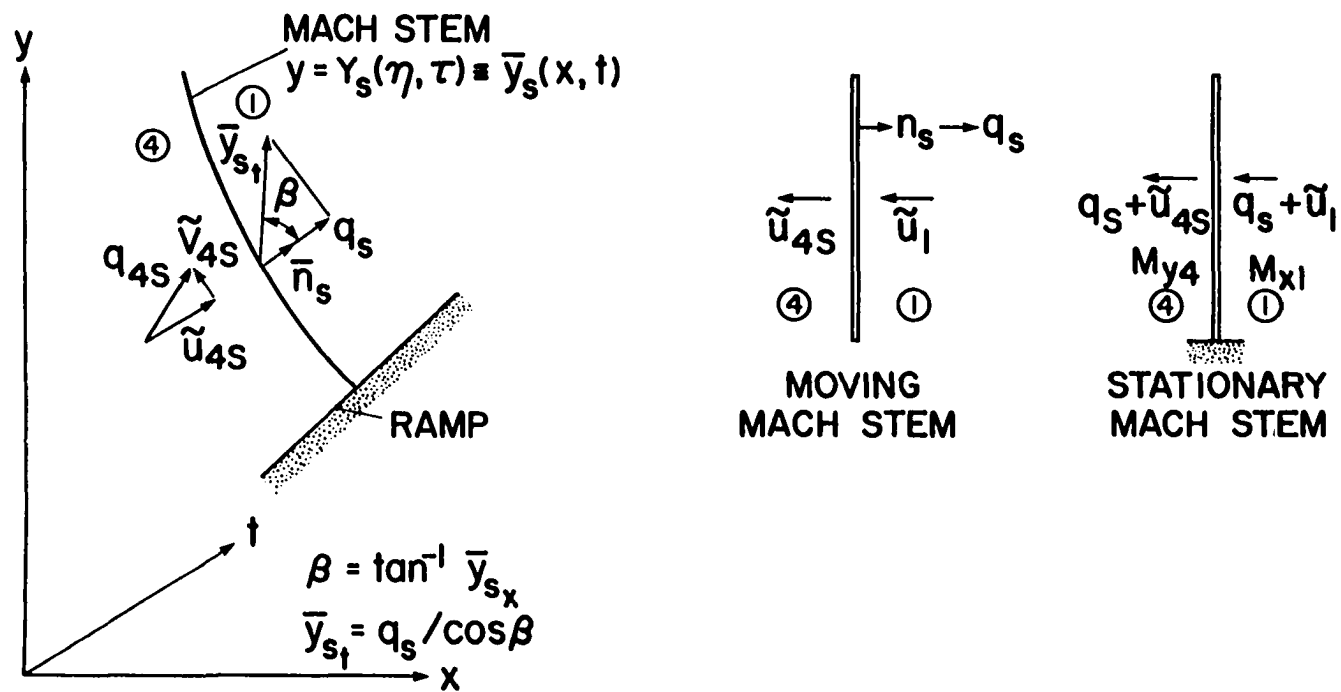


Figure 22. Mach stem propagation in unsteady flow

$$\vec{n}_s = - \frac{\bar{y}_s \hat{i} + \hat{j}}{\sqrt{1 + \bar{y}_{s_x}^2}} \quad (71)$$

$$\tilde{u}_1 = \vec{q}_1 \cdot \vec{n}_s = 0 \quad (72)$$

$$a_1 = \sqrt{\gamma p_1 / \rho_1} = \sqrt{\gamma} \quad (73)$$

$$Y_{s_\tau}(\eta, \tau) = \bar{y}_{s_t} + \bar{y}_{s_x} x_\tau = \frac{Y_s(\eta, \tau)}{\tau} \quad (74)$$

$$q_s = \bar{y}_{s_t} \cos \beta \quad (75)$$

$$\bar{y}_{s_x} = \frac{Y_{s_\eta}(\eta, \tau)}{x_\eta} \quad (76)$$

$$\beta = \tan^{-1}(\bar{y}_{s_x}) \quad (77)$$

$$M_{y1} = \frac{\tilde{u}_1 + q_s}{a_1} \quad (78)$$

$$\frac{p_{4s}}{p_1} = \frac{2\gamma M_{y1}^2 - (\gamma - 1)}{\gamma + 1} \quad (79)$$

$$\frac{\rho_{4s}}{\rho_1} = \frac{(\gamma + 1)M_{y1}^2}{(\gamma - 1)M_{y1}^2 + 2} \quad (80)$$

$$M_{x4} = \left[ \frac{(\gamma - 1)M_{y1}^2 + 2}{2\gamma M_{y1}^2 - (\gamma - 1)} \right] \quad (81)$$

$$\tilde{u}_{4s} = -q_s + M_{x4} a_{4s} \quad (82)$$

$$a_{4s} = \sqrt{\gamma p_{4s} / \rho_{4s}} \quad (83)$$

$$u_{4s} = \frac{(\tilde{u}_{4s} - \tilde{u}_1) \bar{y}_{s_x}}{\sqrt{1 + \bar{y}_{s_x}^2}} \quad (84)$$

$$v_{4s} = - \frac{\tilde{u}_{4s} - \tilde{u}_1}{\sqrt{1 + \bar{y}_{s_x}^2}} \quad (85)$$

$$e_{4s} = \frac{p_{4s}}{\gamma - 1} + \rho_{4s} \left( \frac{u_{4s}^2 + v_{4s}^2}{2} \right) \quad (86)$$

where  $\vec{n}_s$  is the outward Mach stem normal,  $\vec{q}_s$  is the velocity of the Mach stem in its normal direction,  $Y_{s_\tau}$  is the shock speed in the computational plane,  $\bar{y}_{s_t}$  is the shock speed in the physical plane, and  $\bar{y}_{s_x}$  is the Mach stem slope. The quantity appearing in Equation (76) is computed numerically using a central difference formula. The subscript 1 refers to flow conditions in region (1), and the subscript 4s refers to flow conditions behind the Mach stem (along  $\xi = 1$  in Figure 19b).

With the flow conditions behind the reflected shock and the Mach stem known, all the field points ( $1 < k < k_{\max}$ ,  $1 < j < j_{\max}$ ) are now initialized. The conditions at the stagnation point (point 0 in Figure 20) are computed from Equations (25) to (31) based on the normal part of the reflected shock (point A). The point where the slip surface meets the ramp is a vortical singularity where the self-similar velocity components are zero. Thus, initially the velocities at point VS (see Figure 20) are assumed to be

$$\left. \begin{aligned} u_{VS} &= \frac{x_{VS}}{\tau} \\ v_{VS} &= \frac{y_{VS}}{\tau} \end{aligned} \right\} \quad (87)$$

Along the ramp between point 0 and point VS and between point VS and point B (Mach foot) the velocities are linearly interpolated and the pressure is approximated by a parabola. Along the wall (A-0) a parabolic approximation of the flow variables is used. The entropy along the wall and the ramp up to the point VS is equal to that behind the normal part of the reflected shock, and between VS and the Mach foot it is equal to that behind the foot of the Mach stem. With pressure and entropy known along the ramp and the wall, the density is computed from

$$\rho = \left( \frac{p}{s} \right)^{1/\gamma} \quad (88)$$

where  $s$  is an appropriate measure of the entropy level. The total energy  $e$  is then computed. The pressure at the field points ( $1 < k < k_{\max}$ ,  $1 < j < j_{\max}$ ) are obtained by a linear interpolation of the pressure at the reflected shock and the ramp. The pressure along the slip surface is then obtained by a linear interpolation using the values at the neighboring grid points. The side of the slip surface facing the reflected shock is denoted by "a" (see Figure 20) and the side facing the Mach stem is denoted by "b." The pressure on either side of the slip surface is the same but the velocities are not. The velocity components along the slip surface on side "a" are obtained by linear interpolation using the values at point VS and point 3 at the triple point. Similarly the velocity

components along the slip surface on side "b" are obtained by linear interpolation using the values at point VS and point 4 at the triple point. The u-velocity component along the slip surface on side "a" is recomputed to satisfy the jump condition

$$(u_a - u_b) \tan(90^\circ - \alpha) = v_a - v_b \quad (89)$$

The entropy along the slip surface on side "a" and side "b" is equal to  $s_3$  and  $s_4$  respectively (the slip surface is a self-similar streamline along which the entropy is constant). Knowing the entropy and the pressure, the density along the slip surface is computed. Based on the flow conditions along the slip surface on side "a" and the reflected shock, the field points lying in region I (Figure 20) are initialized. Similarly, based on the flow conditions along the slip surface on side "b" and the Mach stem, the field points lying in region II are initialized using linear interpolation.

Starting with this initialized flow field, Equation (1) is integrated (subject to certain boundary conditions discussed in the next section) using the explicit, second-order, MacCormack's (32) scheme. Since the slip surface floats within the  $\eta, \xi$  mesh system a floating-fitting scheme in conjunction with the method of characteristics is developed to propagate the slip surface. Under this scheme differencing across the slip surface is forbidden. Thus, special one-sided differencing formulas (37) are used at grid points neighboring the slip surface. The floating-fitting scheme along with the special differencing formulas are explained in a later section.

### Boundary Conditions

The computational region is bounded by the reflected shock, the Mach stem, the wall and the ramp. The boundary condition procedures used at each of these surfaces are discussed below.

#### Reflected shock

The position, shape and the speed of the reflected shock wave are determined at each step of the time-asymptotic integration procedure. The variables  $X_s(\xi, \tau)$ ,  $X_{s_\xi}(\xi, \tau)$ , and  $X_{s_\tau}(\xi, \tau)$  which appear in Equation (1) along with the flow variables behind the shock are determined by employing the unsteady version of the Thomas' "pressure approach" (27,28) for propagating shock waves. As mentioned in Chapter II, in this approach it is necessary to know only the pressure behind the reflected shock ( $p_{3s}$ ) in order to alter its position for the next time level. This required pressure is obtained by using the normal field point predictor-corrector algorithm at the reflected shock but with one-sided differences in the  $\eta$ -direction. As mentioned in the previous section (Initial Conditions) in order to compute the shock speed  $X_{s_\tau}(\xi, \tau)$ , it is necessary to define an equivalent reflected shock shape in terms of the physical variables  $t$ ,  $x$ , and  $y$ . Such a representation is given by Equation (54). Knowing pressure the remaining flow variables are given by the following equations, which include the Rankine-Hugoniot relations.

$$M_{x2} = \left\{ \frac{1}{2\gamma} \left[ \frac{p_{3s}}{p_2} (\gamma + 1) + (\gamma - 1) \right] \right\}^{1/2} \quad (90)$$

$$q_s = \tilde{u}_2 - a_2 M_{x2} \quad (91)$$

$$a_2 = \sqrt{\gamma p_2 / \rho_2} \quad (92)$$

$$\rho_{3s} = \rho_2 \frac{(\gamma + 1)M_{x2}^2}{(\gamma - 1)M_{x2}^2 + 2} \quad (93)$$

$$M_{y3} = \left[ \frac{(\gamma - 1)M_{x2}^2 + 2}{2\gamma M_{x2}^2 - (\gamma - 1)} \right]^{1/2} \quad (94)$$

$$\tilde{u}_{3s} = M_{y3} a_{3s} + q_s \quad (95)$$

$$a_{3s} = \sqrt{\gamma p_{3s} / \rho_{3s}} \quad (96)$$

The velocity components  $u_{3s}$  and  $v_{3s}$  and the total energy  $e_{3s}$  are then computed from Equations (68) to (70). The actual propagation of the reflected shock along with the Mach stem is presented under a separate subheading.

#### Mach stem

The variables  $Y_s(\eta, \tau)$ ,  $Y_{s_\eta}(\eta, \tau)$ , and  $Y_{s_\tau}(\eta, \tau)$  along with the flow variables behind the Mach stem are determined from pressure ( $p_{4s}$ ) using the same Thomas' "pressure approach" employed for the reflected shock. The pressure behind the Mach stem ( $p_{4s}$ ) is obtained from the finite-difference algorithm using one-sided differences in the  $\xi$ -direction. The remaining flow variables are given by the following equations:

$$M_{y1} = \left\{ \frac{1}{2\gamma} \left[ \frac{p_{4s}}{p_1} (\gamma + 1) + (\gamma - 1) \right] \right\}^{1/2} \quad (97)$$

$$q_s = M_{y1} a_1 - \tilde{u}_1 \quad (98)$$

$$a_1 = \sqrt{\gamma} \quad (99)$$



$$\rho_{4s} = \rho_1 \frac{(\gamma + 1)M_{y1}^2}{(\gamma - 1)M_{y1}^2 + 2} \quad (100)$$

$$M_{x4} = \left[ \frac{(\gamma - 1)M_{y1}^2 + 2}{2\gamma M_{y1}^2 - (\gamma - 1)} \right]^{1/2} \quad (101)$$

$$\tilde{u}_{4s} = -q_s + M_{x4} a_{4s} \quad (102)$$

$$a_{4s} = \sqrt{\gamma p_{4s} / \rho_{4s}} \quad (103)$$

The velocity components  $u_{4s}$  and  $v_{4s}$  and the total energy  $e_{4s}$  are computed from Equations (84) to (86).

#### Impermeable boundaries

The boundary condition procedure used at the wall and the ramp is exactly the same as that used for the regular reflection case except that Kentzer's scheme (35) was not used because it gives the same results as one-sided finite-differences.

#### Shock Speed Calculations

The actual propagation of the reflected shock and the Mach stem in the numerical procedure is accomplished by using a second-order Euler predictor/modified Euler corrector. For the reflected shock it is given by

$$\tilde{X}_s^{n+1}(\xi, \tau) = X_s^n(\xi, \tau) + X_{s_\tau}^n(\xi, \tau) \Delta \tau \quad (104)$$

$$X_s^{n+1}(\xi, \tau) = X_s^n(\xi, \tau) + \frac{1}{2} \left[ X_{s_\tau}^n(\xi, \tau) + \tilde{X}_s^{n+1}(\xi, \tau) \right] \Delta \tau \quad (105)$$

For the Mach stem

$$\tilde{Y}_s^{n+1}(\eta, \tau) = Y_s^n(\eta, \tau) + Y_{s_\tau}^n(\eta, \tau) \Delta \tau \quad (106)$$

$$Y_s^{n+1}(\eta, \tau) = Y_s^n(\eta, \tau) + \frac{1}{2} \left[ Y_{s_\tau}^n(\eta, \tau) + \tilde{Y}_{s_\tau}^{n+1}(\eta, \tau) \right] \Delta \tau \quad (107)$$

Equations (104) and (106) are the predictor step and Equations (105) and (107) are the corrector step. It is necessary to represent the shocks in terms of the physical variables in order to evaluate the shock speeds

$X_{s_\tau}(\xi, \tau)$  and  $Y_{s_\tau}(\eta, \tau)$ . They are evaluated in the following manner:

$$X_{s_\tau}(\xi, \tau) = \bar{x}_{s_t}(y, t) + \bar{x}_{s_y} y_\tau \Big|_{\eta=1} \quad (108)$$

$$Y_{s_\tau}(\eta, \tau) = \bar{y}_{s_t}(x, t) + \bar{y}_{s_x} x_\tau \Big|_{\xi=1} \quad (109)$$

where

$$\bar{x}_{s_y} = \frac{X_{s_\xi}(\xi, \tau)}{y_\xi} \quad (110)$$

$$\bar{y}_{s_x} = \frac{Y_{s_\eta}(\eta, \tau)}{x_\eta} \quad (111)$$

$$y_\tau \Big|_{\eta=1} = \xi Y_{s_\tau}(1, \tau) \quad (112)$$

$$x_\tau \Big|_{\xi=1} = \eta X_{s_\tau}(1, \tau) + (1 - \eta) X_{b_\tau}(1, \tau) \quad (113)$$

$$X_{b_\tau}(1, \tau) = \tan(90^\circ - \theta_r) Y_{s_\tau}(0, \tau) \quad (114)$$

$$x_\eta \Big|_{\xi=1} = X_s(1, \tau) - X_b(1, \tau) \quad (115)$$

$$y_\xi \Big|_{\eta=1} = Y_s(1, \tau) \quad (116)$$

$\bar{x}_{s_t}$  and  $\bar{y}_{s_t}$  are evaluated from Equations (60) and (75), respectively.

It can be seen from Equation (108) that evaluation of  $X_{s_\tau}(\xi, \tau)$  requires

$y_\tau \Big|_{\eta=1}$  which in turn requires  $Y_{s_\tau}(1, \tau)$ . Similarly, evaluation of

$Y_{s_\tau}(\eta, \tau)$  requires  $X_{s_\tau}(1, \tau)$  which is the reflected shock speed at the

triple point. Since the triple point moves with a Mach number  $M_s$ ,  $X_{s_\tau}(1, \tau)$  is simply the speed of the incident shock wave.

$$X_{s_\tau}(1, \tau) = M_s \sqrt{\gamma} \quad (117)$$

Substituting  $\eta = 1$  in Equation (109) an expression for  $Y_{s_\tau}(1, \tau)$  is obtained

$$Y_{s_\tau}(1, \tau) = \bar{y}_{s_t} + \bar{y}_{s_x} X_{s_\tau}(1, \tau) \quad (118)$$

In Equation (118)  $\bar{y}_{s_t}$  and  $\bar{y}_{s_x}$  are evaluated at the triple point.

This completes the calculation of shock speeds. Knowing  $X_{s_\tau}(\xi, \tau)$  and  $Y_{s_\tau}(\eta, \tau)$  the reflected and the Mach stem are advanced using Equations (104) to (107).

### Floating-Fitting Procedure for the Slip Surface

In a usual discontinuity-fitting procedure, the discontinuity is transformed into a computational boundary by means of a normalizing transformation. According to Moretti (37) this is not necessary. His floating-fitting procedure allows one to float the discontinuity within the existing mesh and still fit it by using special one-sided differencing at grid points neighboring the discontinuity. The idea is not to allow differencing across the discontinuity. The actual propagation of the discontinuity in Moretti's approach is done using Kentzer's scheme. In the present analysis, Moretti's floating-fitting idea is used to treat the slip surface. Instead of using Kentzer's scheme, the method of characteristics is used to compute the flow conditions along the slip surface on either side (38).

Figure 19a shows the slip surface floating within the existing mesh system. Since differencing across the discontinuity either in space or time is strictly forbidden in a fitting approach, special one-side differencing formulas are used at grid points neighboring the discontinuity, instead of the usual equally spaced difference approximations (MacCormack's scheme uses forward differences in the predictor and backward differences in the corrector). Application of the usual MacCormack's scheme at the grid point 0 neighboring the slip surface in Figure 23 requires conservative variables at grid points 5 and 6 lying on the other side of the slip surface. Since this is forbidden, the forward differencing in the  $\eta$ -direction ( $\bar{E}_\eta$  in Equation (A10)) is modified to the following (Reference 37):

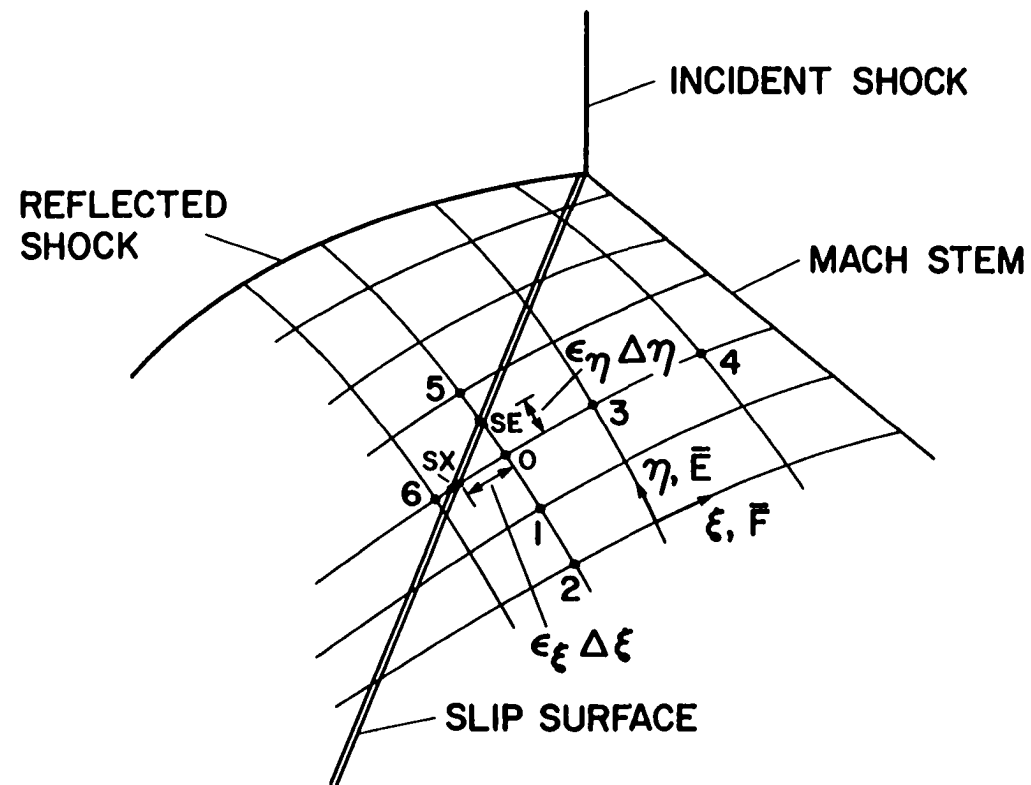


Figure 23. Special differencing approximation for floating-fitting

$$\bar{E}_\eta \Big|_0 = \frac{[\bar{E}_{SE} - (1 - \delta_2)\bar{E}_0 - \delta_2\bar{E}_1]}{\Delta\eta} + \delta_1\bar{E}_\eta \Big|_{SE} \quad (119)$$

where

$$\bar{E}_\eta \Big|_{SE} = \frac{[3\bar{E}_{SE} - 4\epsilon_\eta\bar{E}_0 - (4 - 5\epsilon_\eta)\bar{E}_1 + (1 - \epsilon_\eta)\bar{E}_2]}{2\Delta\eta} \quad (120)$$

$$\delta_1 = \frac{1 - \epsilon_\eta}{1 + \epsilon_\eta} \quad (121)$$

$$\delta_2 = \epsilon_\eta\delta_1 \quad (122)$$

Equation (119) requires two backward grid points (1 and 2). If only one backward grid point is available then Equation (120) is modified to

$$\bar{E}_\eta \Big|_{SE} = \frac{1}{\Delta\eta} \left[ \left( \frac{2\epsilon_\eta - 1}{1 + \epsilon_\eta} \right) \bar{E} + \frac{3}{1 + \epsilon_\eta} \bar{E}_{SE} - 2\bar{E}_0 \right] \quad (123)$$

If no backward grid point is available then Equation (119) is modified to

$$\bar{E}_\eta \Big|_0 = \frac{\bar{E}_{SE} - \bar{E}_0}{\epsilon_\eta \Delta\eta} \quad (124)$$

Similarly, the backward differencing in the  $\xi$ -direction ( $\bar{F}_\xi$  in Equation (A10)) at grid point 0 is modified to

$$\bar{F}_\xi \Big|_0 = - \frac{[\bar{F}_{SX} - (1 - \delta_2)\bar{F}_0 - \delta_2\bar{F}_3]}{\Delta\xi} + \delta_1\bar{F}_\xi \Big|_{SX} \quad (125)$$

where

$$\bar{F}_\xi \Big|_{SX} = - \frac{[3\bar{F}_{SX} - 4\epsilon_\xi\bar{F}_0 - (4 - 5\epsilon_\xi)\bar{F}_3 + (1 - \epsilon_\xi)\bar{F}_4]}{2\Delta\xi} \quad (126)$$

$$\delta_1 = \frac{1 - \varepsilon_\xi}{1 + \varepsilon_\xi} \quad (127)$$

$$\delta_2 = \varepsilon_\xi \delta_1 \quad (128)$$

Equation (125) requires two forward grid points (3 and 4). If only one forward grid point is available then Equation (126) is modified to

$$\bar{F}_\xi \Big|_{SX} = -\frac{1}{\Delta\xi} \left[ \left( \frac{2\varepsilon_\xi - 1}{1 + \varepsilon_\xi} \right) \bar{F}_3 + \frac{3}{1 + \varepsilon_\xi} \bar{F}_{SX} - 2\bar{F}_0 \right] \quad (129)$$

If no forward grid point is available then Equation (125) is modified to

$$\bar{F}_\xi \Big|_0 = \frac{\bar{F}_{SX} - \bar{F}_0}{\varepsilon_\xi \Delta\xi} \quad (130)$$

Similar special differencing formulas are used at grid points neighboring the slip surface on the other side.

All of these special one-sided formulas require the evaluation of the conservative variables at points where the slip surface intersects the constant  $\eta$  and constant  $\xi$  lines. In order to formulate the conservative variables, the flow conditions along the slip surface must be evaluated at each time level. This is done using the method of characteristics.

The flow field is initially assumed on either side of the slip surface at points where it intersects the constant  $\eta$  and constant  $\xi$  lines. As integration proceeds in the time ( $\tau$ ) direction, the location of the initially assumed slip surface keeps changing along with the flow variables on either side until the correct self-similar solution is reached. The actual propagation of the slip surface is carried out only along the

constant  $\eta$  lines, using the method of characteristics. The location and the flow conditions at points where the slip surface intersects the constant  $\xi$  lines are then obtained by a linear interpolation of the values at two neighboring slip surface points lying on constant  $\eta$  lines (see Figure 24). In Figure 24, points "a<sub>1</sub>" and "b<sub>1</sub>" represent two sides of the slip surface at a constant  $\eta$  line at the initial time level "n." At the new time level  $(\tau + \Delta\tau)$  n+1, they are given by "a" and "b." The problem here is to locate this new slip surface position and to compute the flow conditions at "a" and "b." Out of the ten flow variables ( $p_a, \rho_a, u_a, v_a, e_a, p_b, \rho_b, u_b, v_b$  and  $e_b$ ) only six ( $p_a, u_a, v_a, p_b, u_b$ , and  $v_b$ ) need to be evaluated. The densities  $\rho_a$  and  $\rho_b$  and the total energies  $e_a$  and  $e_b$  can be obtained from

$$\rho_a = \left( \frac{p_a}{s_a} \right)^{1/\gamma} \quad (131)$$

$$\rho_b = \left( \frac{p_b}{s_b} \right)^{1/\gamma} \quad (132)$$

$$e_a = \frac{p_a}{\gamma - 1} + \frac{\rho_a (u_a^2 + v_a^2)}{2} \quad (133)$$

$$e_b = \frac{p_b}{\gamma - 1} + \frac{\rho_b (u_b^2 + v_b^2)}{2} \quad (134)$$

where  $s_a$  and  $s_b$  are some measure of the entropy values on either side of the slip surface. They are the same as the values at the triple point because the slip surface is a self-similar streamline along which the entropy is constant.



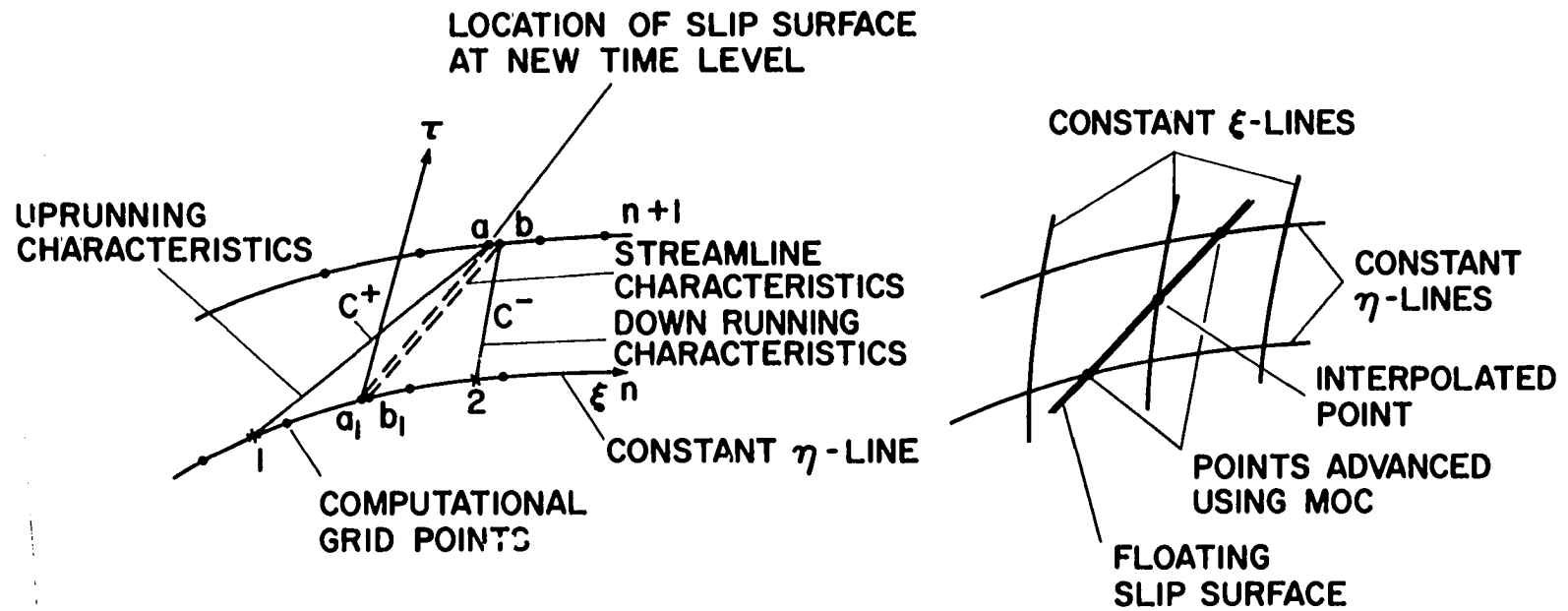


Figure 24. Method of characteristics for the unsteady slip surface propagation

Evaluation of the pressures ( $p_a$  and  $p_b$ ) and the velocities ( $u_a$ ,  $u_b$ ,  $v_a$ , and  $v_b$ ) require six simultaneous algebraic equations. As previously noted, the slip surface is advanced only along the constant  $\eta$  lines. Thus, the characteristic compatibility relations are derived only in the  $(\xi - \tau)$  plane. Figure 24 shows the slip surface location at the old ( $n$ ) and new ( $n+1$ ) time level at a constant  $\eta$  line. From the new time level location, the  $C^+$  and  $C^-$  characteristics are drawn which strike the old time level at points 1 and 2, respectively. The compatibility relation along the  $C^+$  characteristics is given by

$$\begin{aligned}
 (p_a - p_1) + \frac{\rho c \xi_x}{\sqrt{\xi_x^2 + \xi_y^2}} (u_a - u_1) + \frac{\rho c \xi_y}{\sqrt{\xi_x^2 + \xi_y^2}} (v_a - v_1) \\
 = - \left[ \bar{u} p_\eta + \rho c^2 \eta_x u_\eta + \rho c^2 \eta_y v_\eta + \frac{\rho c \xi_x}{\sqrt{\xi_x^2 + \xi_y^2}} \left( \frac{\eta_x p_\eta}{\rho} + \bar{u} u_\eta \right) \right. \\
 \left. + \frac{\rho c \xi_y}{\sqrt{\xi_x^2 + \xi_y^2}} \left( \frac{\eta_y p_\eta}{\rho} + \bar{u} v_\eta \right) \right] \Delta \tau
 \end{aligned} \tag{135}$$

Similarly, the compatibility relation along the  $C^-$  characteristics is given by

$$\begin{aligned}
 (p_b - p_2) - \frac{\rho c \xi_x}{\sqrt{\xi_x^2 + \xi_y^2}} (u_b - u_2) - \frac{\rho c \xi_y}{\sqrt{\xi_x^2 + \xi_y^2}} (v_b - v_2) \\
 = - \left[ \bar{u} p_\eta + \rho c^2 \eta_x u_\eta + \rho c^2 \eta_y v_\eta - \frac{\rho c \xi_x}{\sqrt{\xi_x^2 + \xi_y^2}} \left( \frac{\eta_x p_\eta}{\rho} + \bar{u} u_\eta \right) \right. \\
 \left. - \frac{\rho c \xi_y}{\sqrt{\xi_x^2 + \xi_y^2}} \left( \frac{\eta_y p_\eta}{\rho} + \bar{u} v_\eta \right) \right] \Delta \tau
 \end{aligned} \tag{136}$$

The line joining the old slip surface location (point  $a_1$  in Figure 24) and the new slip surface location (point  $a$ ) is nothing but the streamline characteristics in the  $(\xi - \tau)$  plane. Compatibility relations are derived along the streamline characteristics on either side of the slip surface. On side "a" it takes the form

$$\xi_y(u_a - u_{a1}) - \xi_x(v_a - v_{a1}) = - \left[ \xi_y \left( \frac{\eta_x p_\eta}{\rho} + \bar{u}u_\eta \right) - \xi_x \left( \frac{\eta_y p_\eta}{\rho} + \bar{u}v_\eta \right) \right] \Delta\tau \quad (137)$$

The similar relation on side "b" is

$$\xi_y(u_b - u_{b1}) - \xi_x(v_b - v_{b1}) = - \left[ \xi_y \left( \frac{\eta_x p_\eta}{\rho} + \bar{u}u_\eta \right) - \xi_x \left( \frac{\eta_y p_\eta}{\rho} + \bar{u}v_\eta \right) \right] \Delta\tau \quad (138)$$

The jump conditions across a moving slip surface are

$$p_a = p_b \quad (139)$$

$$\vec{q}_a \cdot \vec{n}_{s1} = \vec{q}_b \cdot \vec{n}_{s1} = q_{s1} \quad (140)$$

where  $\vec{q}_a$  and  $\vec{q}_b$  are the velocity vectors on either side of the slip surface,  $\vec{n}_{s1}$  is the slip surface normal and  $q_{s1}$  is the velocity of the slip surface in its normal direction. The slip surface is defined by

$$y - y_{s1}(x, t) = 0 \quad (141)$$

Using Equation (141), the second jump condition is rewritten in the form

$$(u_a - u_b) \left( y_{s1} \right)_x = v_b - v_a \quad (142)$$

where  $\left( y_{s1} \right)_x$  is the slope of the slip surface.

The unknown flow variables  $p_a$ ,  $p_b$ ,  $u_a$ ,  $u_b$ ,  $v_a$ , and  $v_b$  are now obtained by solving Equations (135)-(139) and (142) simultaneously. The actual propagation of the slip surface is carried out by

$$y_{sl}^{n+1} = y_{sl}^n + \left( y_{sl} \right)_\tau^n \Delta\tau \quad (143)$$

where  $\left( y_{sl} \right)_\tau$  is the speed of the slip surface and is evaluated in a manner similar to the shock speed. When the flow field converges, the slip surface speed  $\left( y_{sl} \right)_\tau$  should converge to  $y_{sl}/\tau$ .

### Results

The computational grid for a typical single Mach reflection case consisted of 6 points in the  $\eta$ -direction and 31 points in the  $\xi$ -direction. An average of 400 iterations was required to obtain a converged solution and required approximately 15 minutes of computer time on an IBM 360/67.

Numerical results in the form of pressure contours are qualitatively compared with the first-order shock-capturing results of Rusanov's solution in Figure 25. Rusanov's solution was obtained using Godunov's method for an incident shock Mach number of 1.89 impinging on a  $30^\circ$  ramp. Most of the contours which appear in Figure 25a lie within the captured shock waves, and very few describe the flow field bounded by the reflected shock, the Mach stem, the wall and the ramp in comparison with the contours of Figure 25b.

Law (5) performed a series of experiments on the shock diffraction problem for various gases using a Mach-Zehnder interferometer. He tested two cases which resulted in single Mach reflection. The ramp angle for

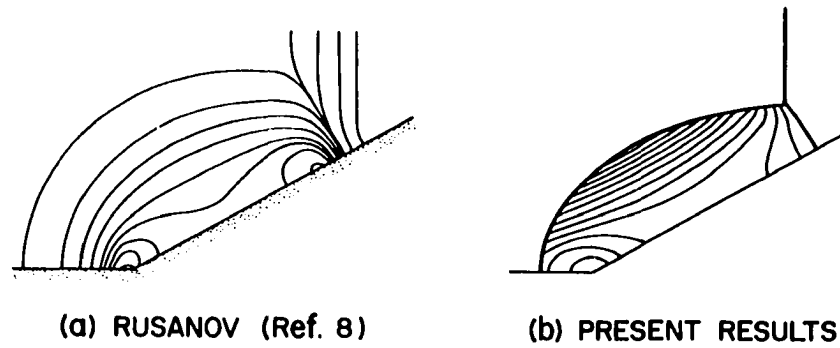


Figure 25. Comparison of numerically generated pressure contours.  $M_8 = 1.89$ ,  $\theta_r = 30^\circ$

both the cases was  $40^\circ$  and the incident shock Mach number for one case was 1.89 and for the other 2.10. Numerical results were generated for these two cases to demonstrate the flow field behavior in the single Mach reflection regime. The numerical results are presented in Figures 26-35.

The density and pressure distributions along the wall and the ramp for two cases are shown in Figures 26 and 27. The juncture of the wall and the ramp is a stagnation point (point C) at which pressure and density reach a local maximum. The point where the slip surface meets the ramp is a vortical singularity (point D) at which the pressure is continuous and reaches a local minimum. The vortical singularity is nothing but a slip surface at a point at which the density takes a jump because of the discontinuous behavior of the entropy. The numerical results clearly exhibit this flow field behavior as predicted by Ludloff and Friedman (11).

The mesh in the physical plane is automatically generated by the double normalizing transformation. As reflected shock and the Mach stem change their shapes during the iteration process, the mesh in the physical plane also keeps deforming until the self-similar flow field is established. Figures (28) and (29) show the converged mesh in the physical plane for incident shock Mach numbers 1.89 and 2.1, respectively, for a ramp angle of  $40^\circ$ . The slip surface is clearly seen to float within the physical mesh.

Pressure contour plots of the physical region are shown for two cases in Figures 30 and 31. The centerpoint of isobars near the wall-ramp juncture, and the saddle point of isobars near the vortical singularity can be clearly observed. By doing a local analysis of the gasdynamic equations

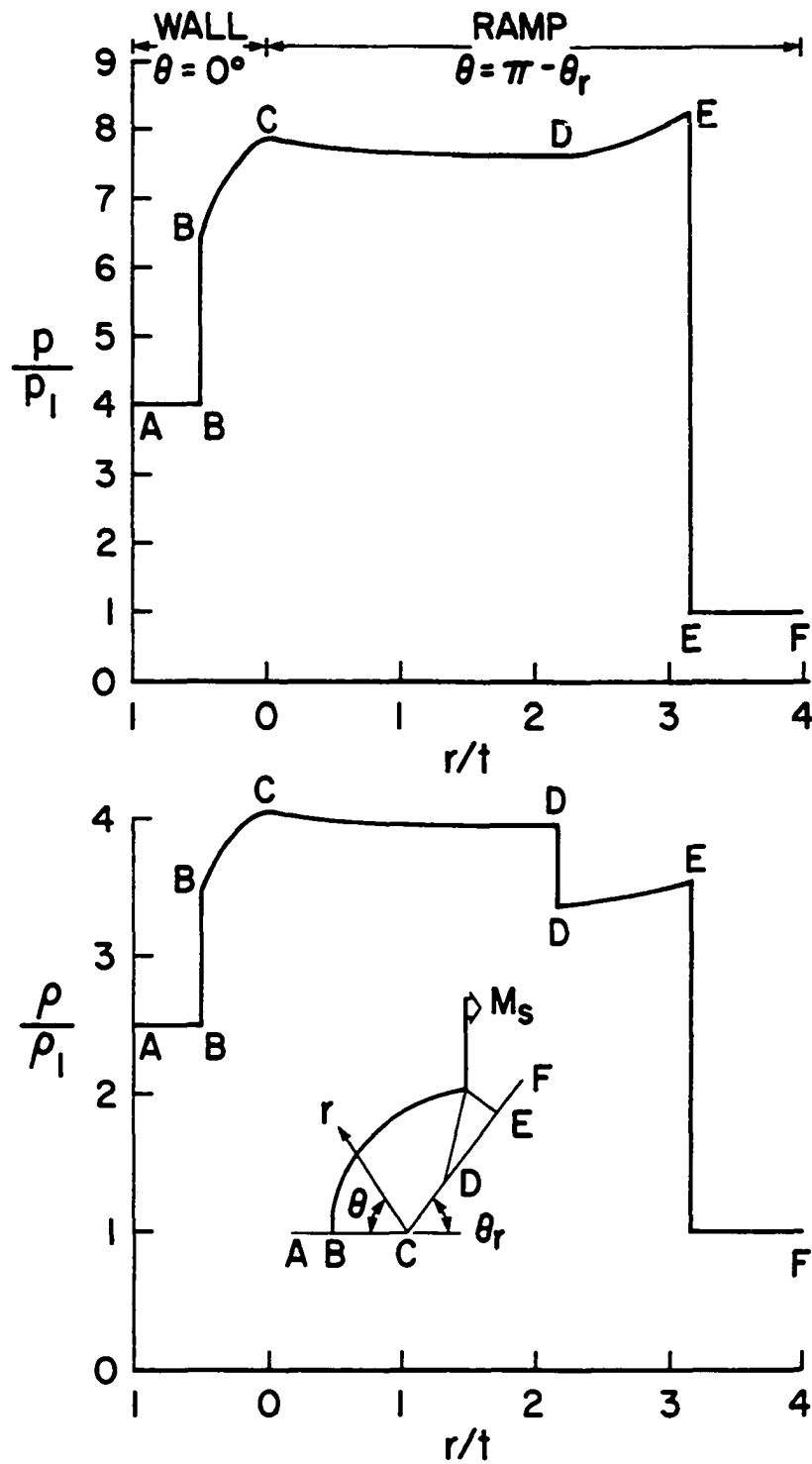


Figure 26. Surface pressure and density along the wall and the ramp.  
 $M_s = 1.89$ ,  $\theta_r = 40^\circ$

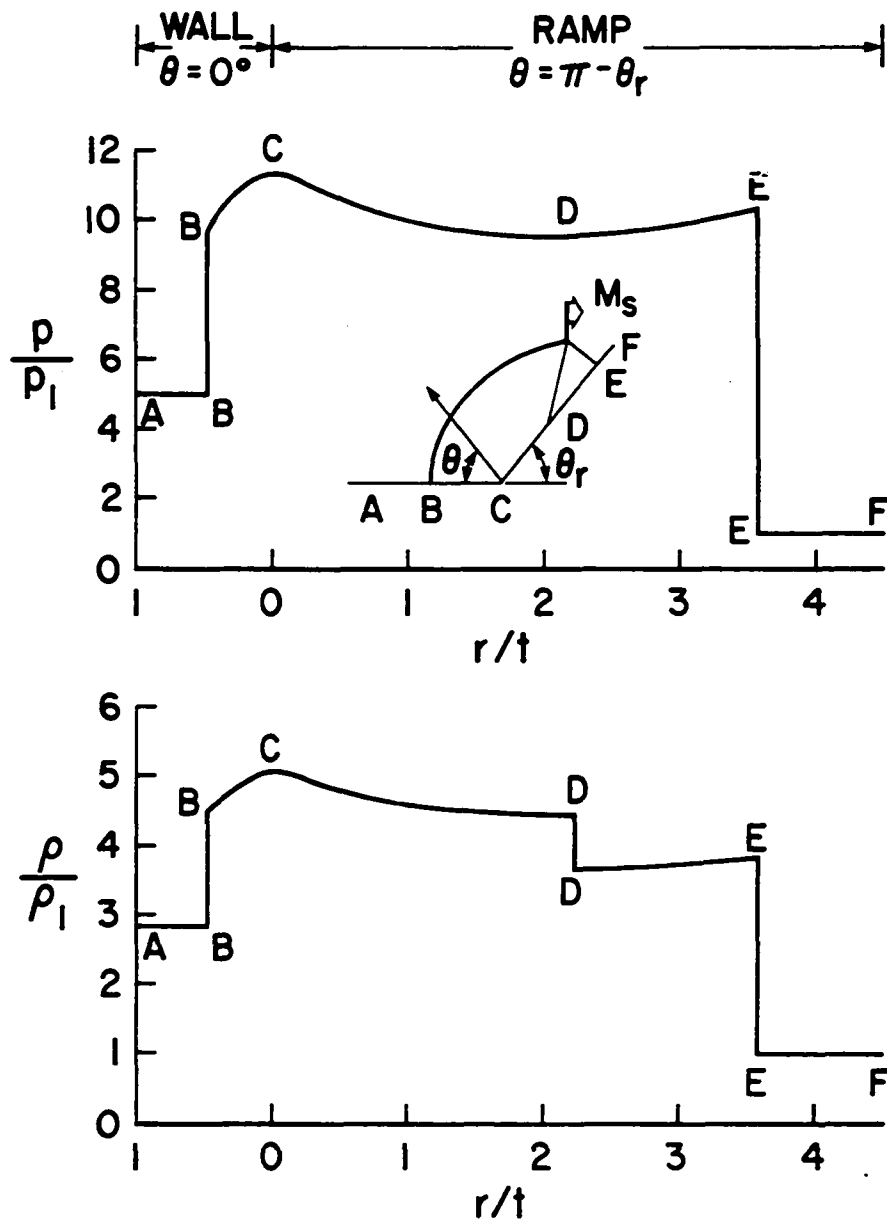


Figure 27. Surface pressure and density along the wall and the ramp.  
 $M_s = 2.1$ ,  $\theta_r = 40^\circ$



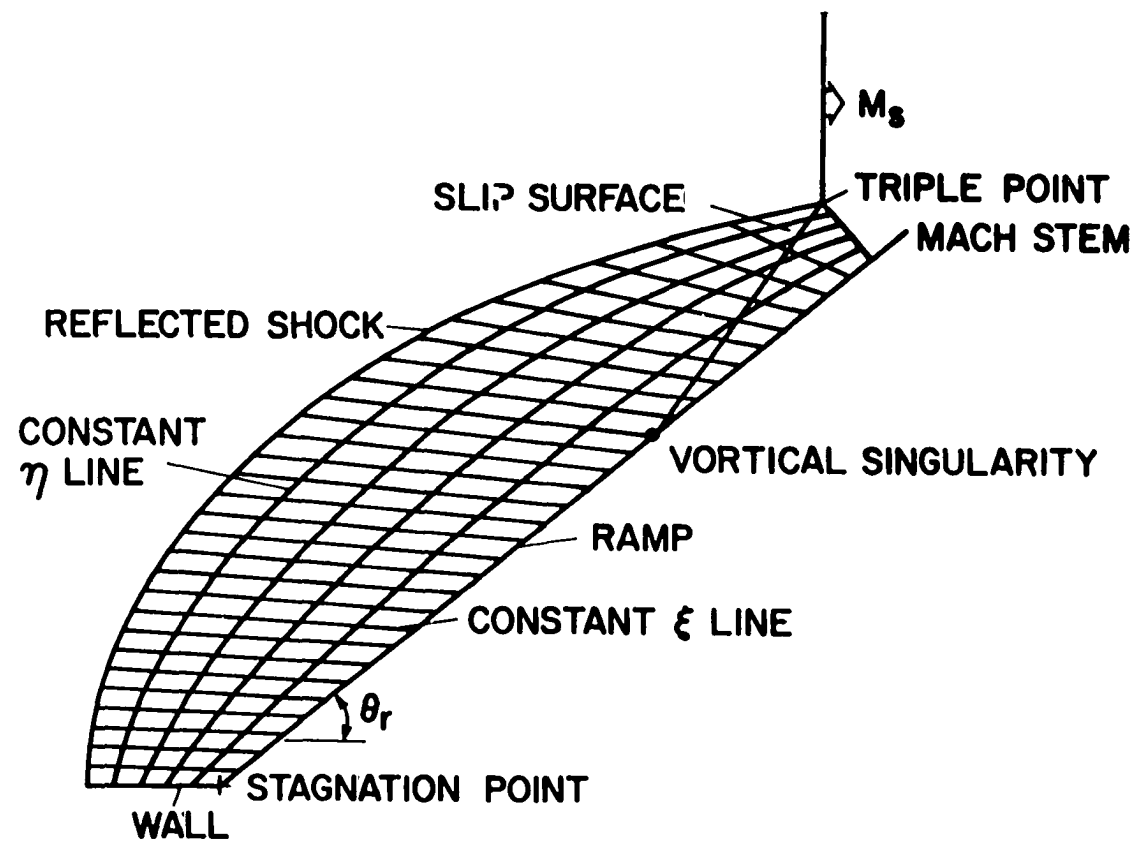


Figure 28. Mesh in physical plane.  $M_s = 1.89$ ,  $\theta_r = 40^\circ$

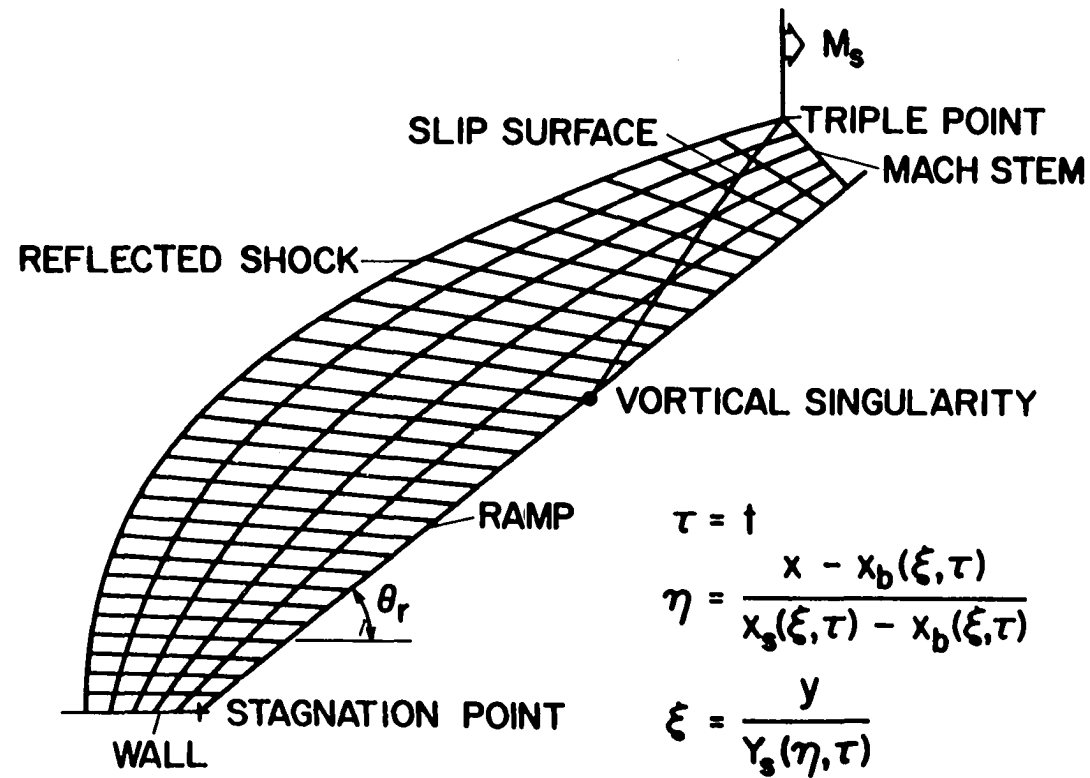


Figure 29. Mesh in physical plane.  $M_s = 2.1$ ,  $\theta_r = 40^\circ$

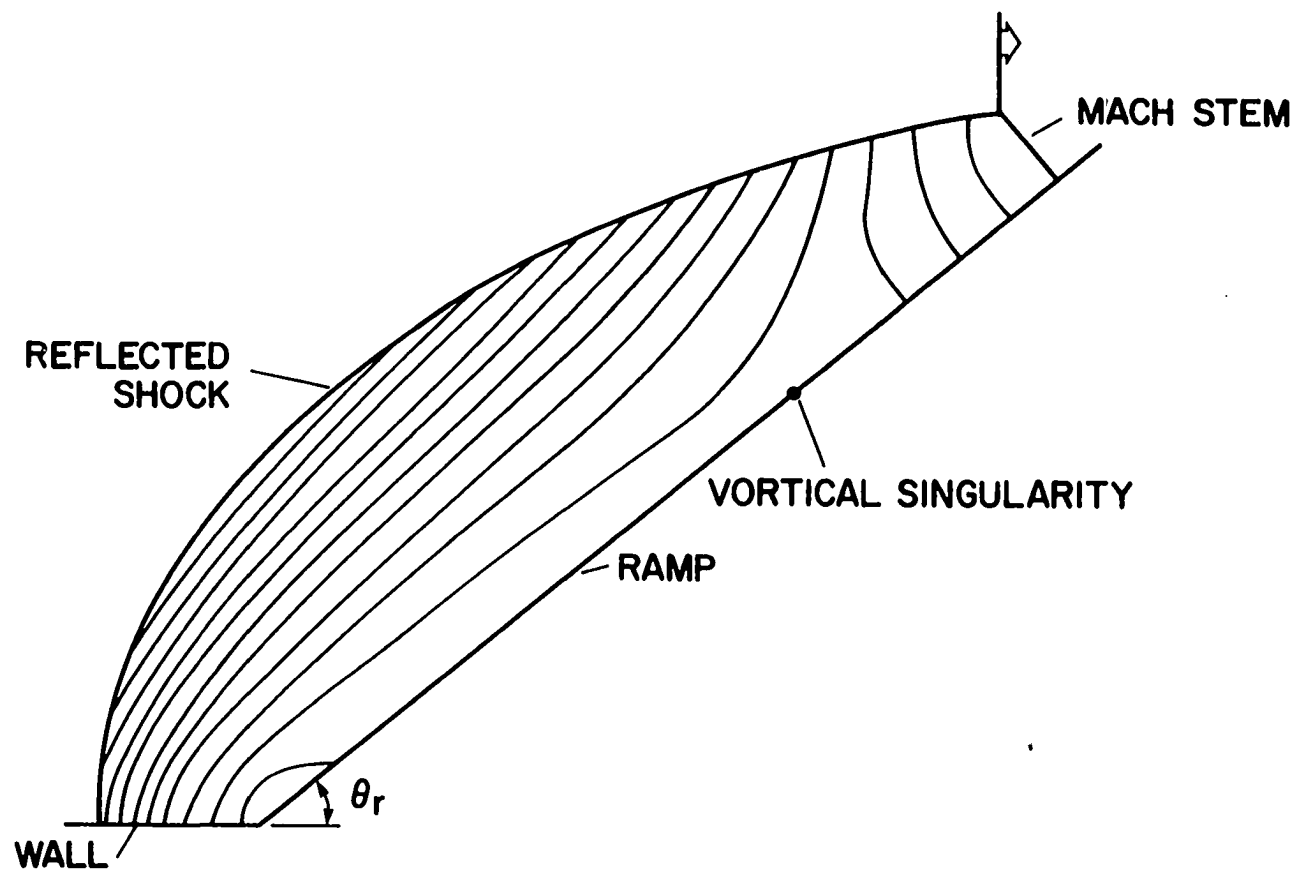


Figure 30. Pressure contours.  $M_g = 1.89$ ,  $\theta_r = 40^\circ$

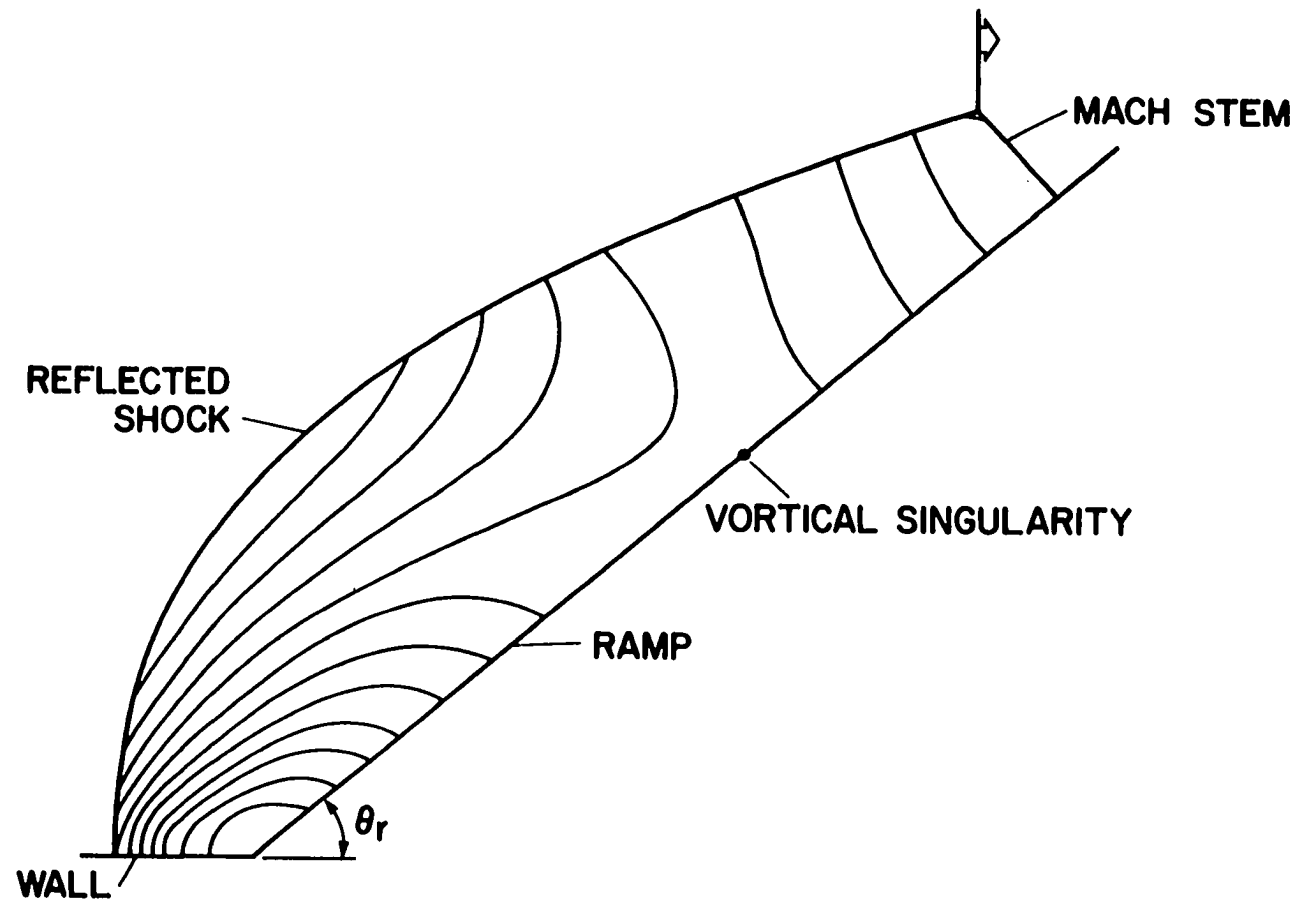


Figure 31. Pressure contours.  $M_g = 2.1$ ,  $\theta_r = 40^\circ$

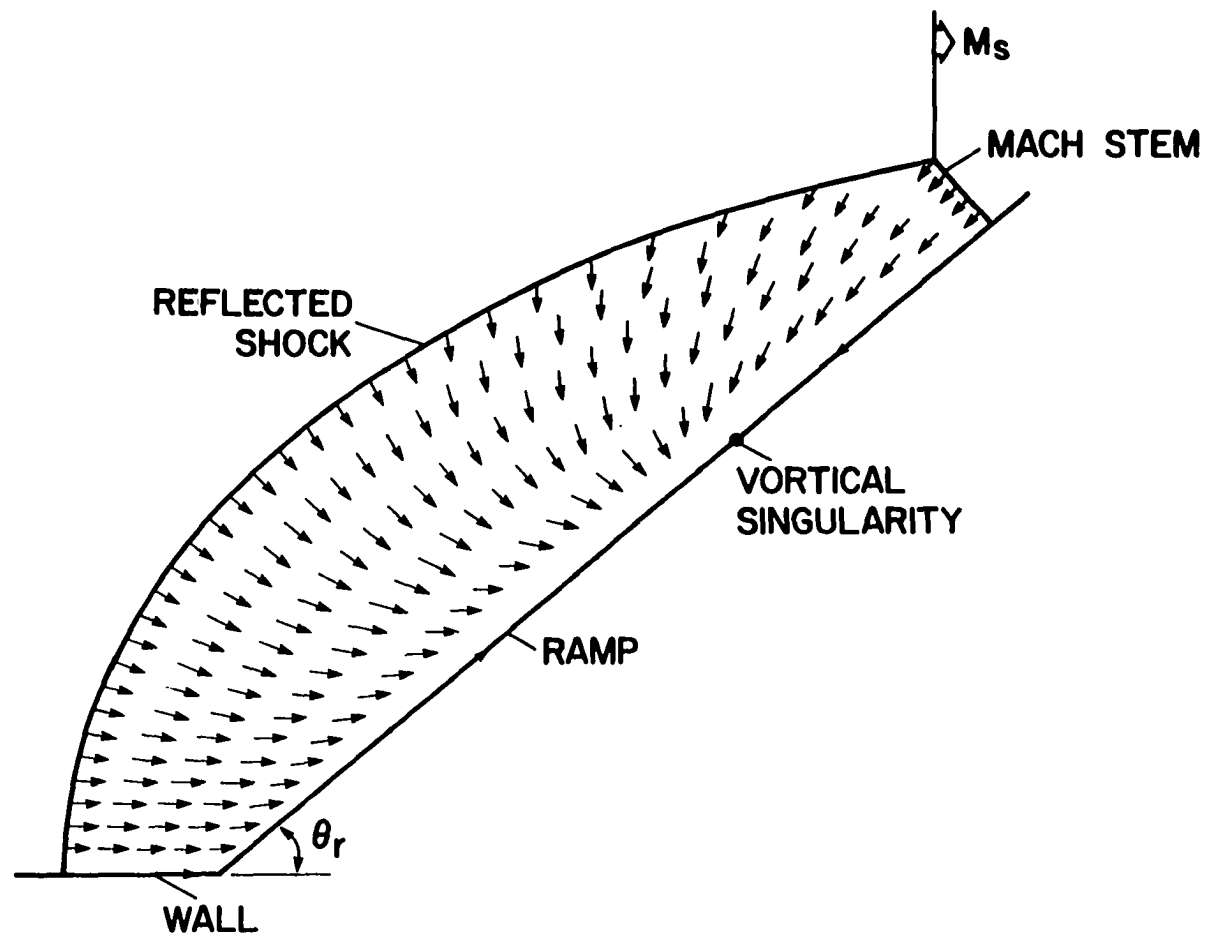


Figure 32. Self-similar velocity directional plot.  $M_s = 1.89$ ,  $\theta_r = 40^\circ$

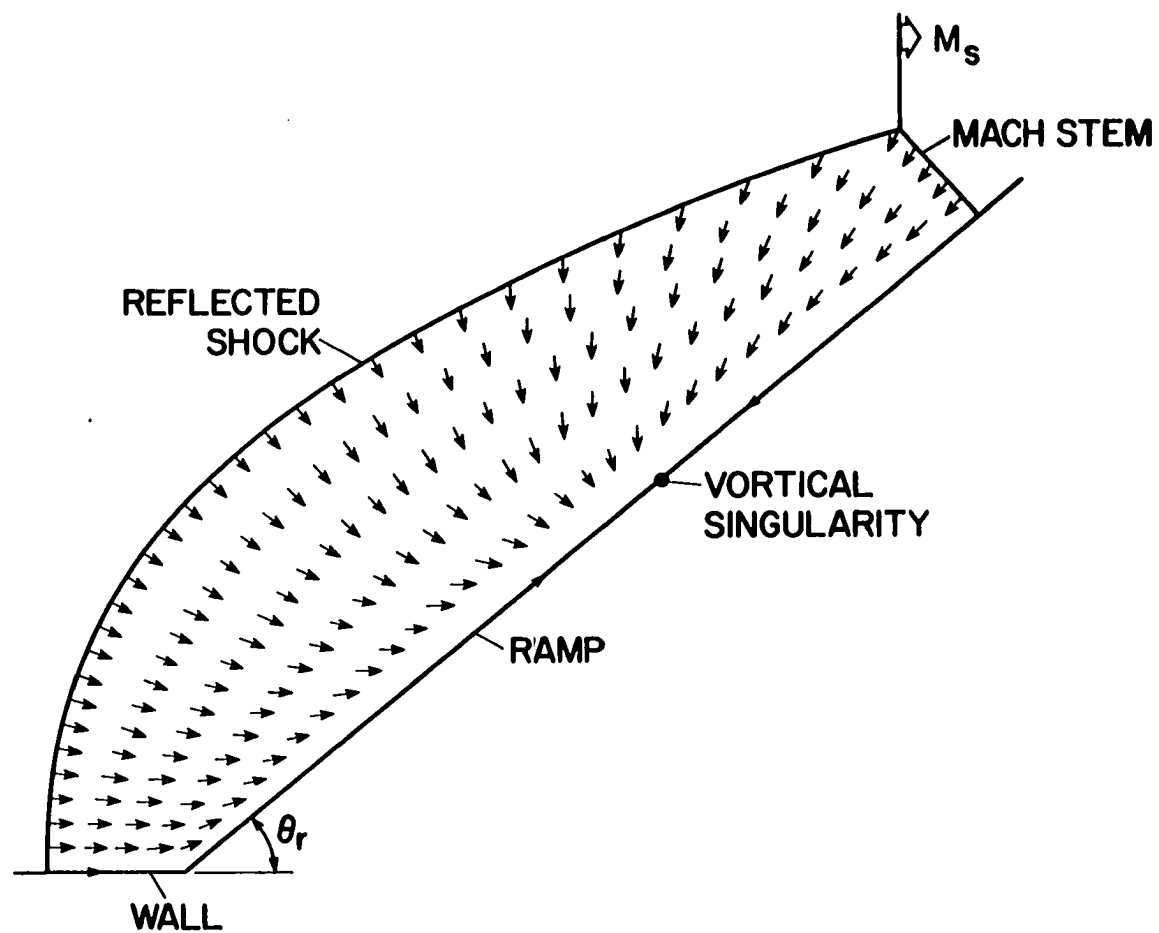


Figure 33. Self-similar velocity directional plot.  $M_s = 2.1$ ,  $\theta_r = 40^\circ$

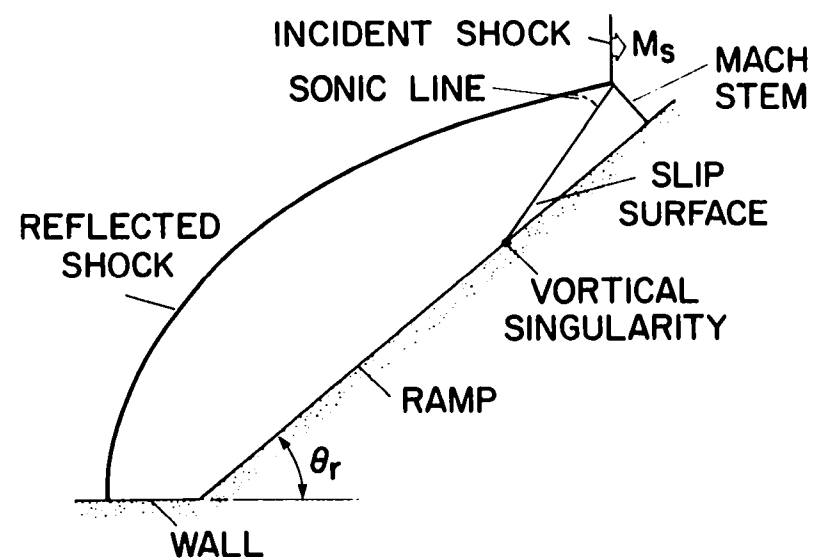
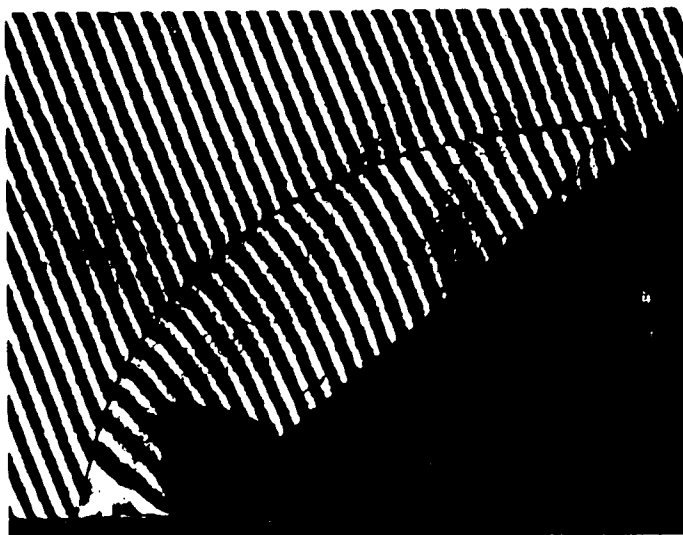


Figure 34. Comparison of experimental and computed shock and slip surface positions.  
 $M_s = 1.89$ ,  $\theta_r = 40^\circ$

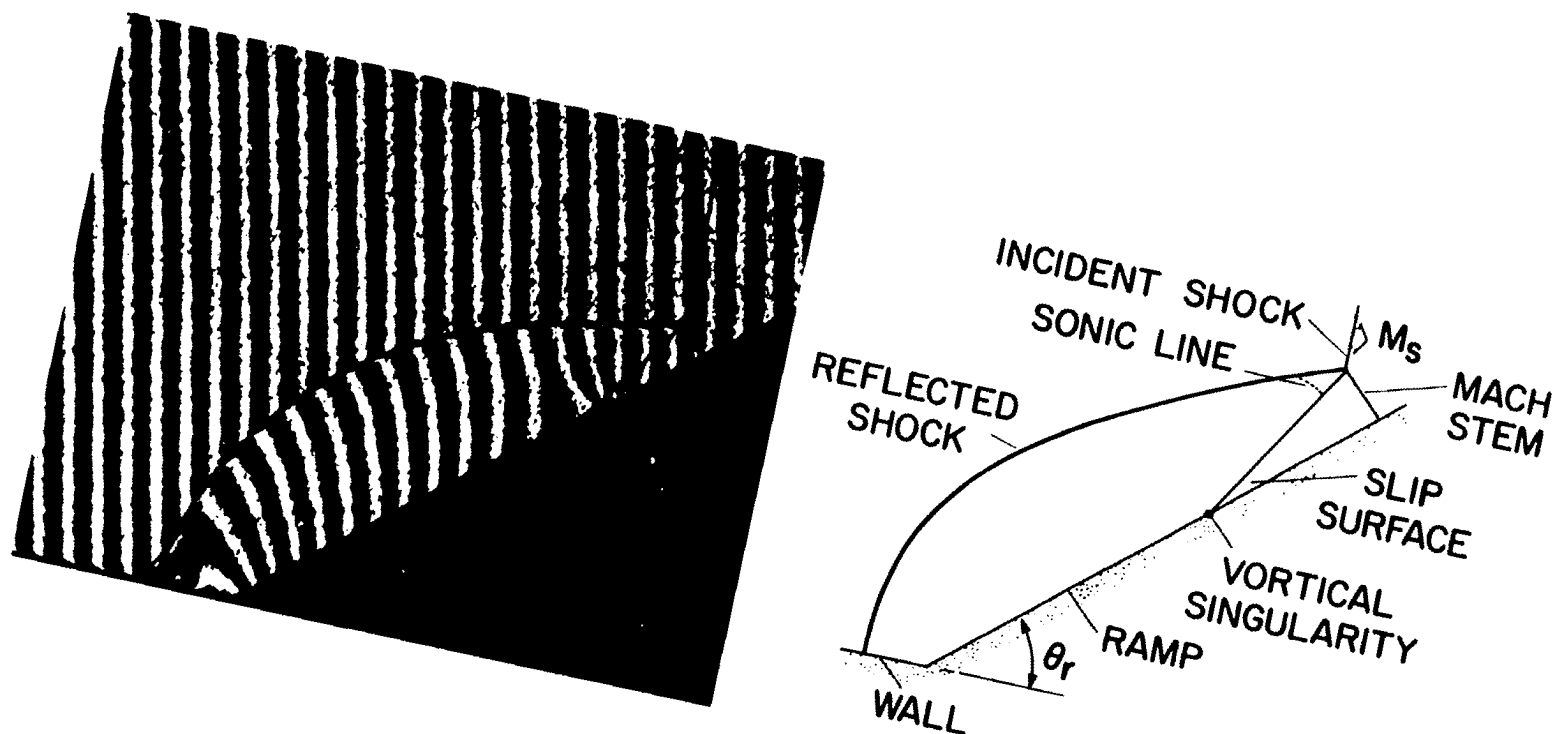


Figure 35. Comparison of experimental and computed shock and slip surface positions.  
 $M_s = 2.1$ ,  $\theta_r = 40^\circ$



at these singularities (stagnation point is a saddle singularity and the vortical singularity is a nodal singularity) Ludloff and Friedman (11) came up with the same behavior for isobars as seen in the numerical solutions. Figures 30 and 31 also exhibit the continuous behavior of pressure across the slip surface. In order to show any discontinuous behavior of the flow field as a sharp jump in the contour plot, the contour program requires that such a discontinuity be treated as one of the boundaries of the computational region because of the various interpolations involved. Since the slip surface is floated within the computational mesh the contour program cannot bring out the true sharp jump in the density across the slip surface in a density contour plot. The density contour plot might look as though the slip surface was captured within a mesh interval.

The self-similar velocity directional plot for two cases are shown in Figures 32 and 33. The self-similar streamline pattern can be visualized from these plots. Notice that all the streamlines tend to converge at the vortical singularity (nodal singularity). The streamlines also diverge away from the stagnation point (saddle point). Only the stagnation streamline passes through the stagnation point.

The comparison of the interferogram obtained by Law (5) with the numerically computed shock and slip surface shape is shown for two cases in Figures 34 and 35. The triple point trajectory angle ( $\chi$ ) in the numerical solution is larger than that shown in the experimental interferogram. The reason for the discrepancy is probably two fold: First, the viscous effects (the majority of which can be observed near the wall-ramp

intersection) might have the effect of decreasing the ramp angle as a result of the boundary layer growth with distance from the Mach foot. The reduced ramp angle in turn results in larger triple point trajectory angle. Second, the computed solution assumes flow of an ideal gas ( $\gamma = 1.4$ ). Thus, high temperature effects on the internal energy such as molecular, vibrational excitations are not taken into account. The slip surface in the numerical solution comes out to be nearly straight as seen in the experimental picture. In addition, a small self-similar supersonic region lies between the slip surface and the reflected shock. The sonic line bounding this supersonic region is shown in the numerical results in Figures 34 and 35.

## CHAPTER IV. CONCLUDING REMARKS

The discontinuity-fitting procedure developed in this report for computing the shock diffraction problem for the regular and the single Mach reflection is capable of accurately predicting the inviscid flow field with its reflected shock, the Mach stem, the slip surface and the vortical singularity. The solution in the neighborhood of the self-similar stagnation points exhibit gasdynamic equations with regards to the behavior of the self-similar streamlines, isobars and isopycnics. The present numerical results are a considerable improvement over the early first-order numerical solutions and compare favorably with available experimental data.

The present work treats only the regular reflection and the single Mach reflection cases. In order to develop a discontinuity-fitting procedure for the double Mach reflection case, a good a priori knowledge of the flow structure is required. Thus, a development of a good shock-capturing solution for the double Mach stem case is very desirable to understand what exactly is going on.

Extension of the present planar shock diffraction problem to the spherical shock diffraction problem is suggested.

### ACKNOWLEDGEMENTS

The author wishes to express his gratitude and sincere appreciation to Dr. Dale Anderson for his guidance and helpful suggestions throughout his graduate school career; to Dr. Paul Kutler of NASA Ames Research Center for his creative suggestions, technical advice, and close supervision; to Mr. Jim Daywitt for many helpful discussions.

Finally, the author would like to thank NASA Ames Research Center and Engineering Research Institute at Iowa State University for their financial support during his graduate studies.

## REFERENCES

1. Smith, L. G. "Photographic Investigation of the Reflection of Plane Shocks in Air." Office of Scientific Research and Development, Report 4943, 1945.
2. Weynants, R. R. "An Experimental Investigation of Shock Wave Diffraction Over Compression and Expansion Corners." UTIAS TN No. 126, April 1968.
3. Gvozdeva, L. G., Predvoditeleva, O. A., and Fokeev, V. P. "Mach Reflection of Shock Waves in Real Gases." Astronautica Acta, 15 (January 1969), 503-508.
4. Gvozdeva, L. G., Bazhenova, T. V., Predvoditeleva, O. A., and Fokeev, V. P. "Pressure and Temperature at the Wedge Surface for Mach Reflection of Strong Shock Waves." Astronautica Acta, 15 (January 1970), 503-510.
5. Law, C. K. "Diffraction of Strong Shock Waves by a Compressive Corner." UTIAS TN No. 150, July 1970.
6. Bertrand, B. P. "Measurement of Pressure in Mach Reflection of Strong Shock Waves in a Shock Tube." Ballistic Research Laboratories, Memorandum Report No. 2196, June 1972.
7. Bazhenova, T. V., Gvozdena, L. G., Komarov, V. S., and Sukhov, B. G. "Diffraction of Strong Shock Waves by Convex Corners." Izvestiya Akademii Nauk SSSR, Mekhanika Zhidkosti i Gaza, No. 4 (July 1973), 122-134.
8. Bazhenova, T. V., Fokeev, V. P., and Gvozdeva, L. G. "Regions of Various Forms of Mach Reflection and its Transition to Regular Reflection." Astronautica Acta, 3 (1976), 131-140.
9. Courant, R., and Friedrichs, K. O. Supersonic Flow and Shock Waves. New York: Interscience Publishers Inc., 1948.
10. Bleakney, W., and Taub, A. H. "Interaction of Shock Waves." Reviews of Modern Physics, 21, No. 4 (October 1949), 584-605.
11. Ludloff, H. F., and Friedman, M. B. "Aerodynamics of Blasts-Diffraction of Blast Around Finite Corners." Journal of the Aeronautical Sciences, 22, No. 1 (January 1955), 27-34.
12. Ludloff, H. F., and Friedman, M. B. "Difference Solution of Shock Diffraction Problem." Journal of the Aeronautical Sciences, 22, No. 2 (February 1955), 139-140.

13. Holt, M. Basic Developments in Fluid Dynamics. New York: Academic Press, 1965.
14. Pack, D. C. "The Reflection and Diffraction of Shock Waves." Journal of Fluid Mechanics, 18 (April 1964), 549-570.
15. Rusanov, V. V. "Calculation of the Interaction of Non-Stationary Shock Waves and Obstructions." Journal of Numerical Analysis and Mathematical Physics, 1, No. 2 (April 1961), 267-279.
16. Henderson, L. V. "The Refraction of a Plane Shock Wave at a Gas Interface." Journal of Fluid Mechanics, 26, Part 3 (November 1966), 607-637.
17. Whitham, G. B. "A New Approach to Problems of Shock Dynamics Part I, Two-Dimensional Problems." Journal of Fluid Mechanics, 2, Part 2 (March 1966), 145-171.
18. Harlow, F. H., and Amsden, A. A. "Fluid Dynamics." Los Alamos Scientific Laboratory Report LA-4700, 1971.
19. Wilkins, M. L. "Calculations of Surface and Ground Waves from Above-Ground and Underground Explosions." Astronautica Acta, 17, Nos. 4 and 5 (1972), 399-404.
20. Zumwalt, G. W. "Weak Wave Reflections at Near 90° Angle of Incidence." Journal of Applied Mechanics, 41, No. 4 (December 1974), 1142-1143.
21. Zhigalko, Y. F. "Approximate Locally-Nonlinear Solutions of the Problem on Interaction Between a Shock Wave and Rigid Wall." Fluid Mechanics - Soviet Research, 4, No. 2 (March 1975), 81-91.
22. Schneyer, G. P. "Numerical Simulation of Regular and Mach Reflections." The Physics of Fluids, 18, No. 9 (September 1975), 119-1124.
23. Podlubnyi, V. V., and Fonarev, A. S. "Reflection of a Spherical Blast Wave from a Planar Surface." Mekhanika Zhidkosti i Gaza, No. 6 (November 1974), 66-72.
24. Lipnitskii, Y. M., and Lyakhov, V. N. "Numerical Solution of the Problem of Wave Diffraction by a Wedge." Mekhanika Zhidkosti i Gaza, No. 6 (November 1974), 88-93.
25. H-Division Quarterly Report. Lawrence Livermore Laboratory, UCRL-50028-71-1, January-March 1976.
26. Carpenter, H. J., and Brode, H. L. "Height of Burst Blast at High Overpressure." Paper No. H3 presented at the Fourth International Symposium on Military Applications of Blast Simulations held at South-end-on-Sea, England, September 9-12, 1974.

27. Thomas, P. D., Vinokur, M., Bastianon, R., and Conti, R. J. "Numerical Solution for the Three Dimensional Inviscid Supersonic Flow of a Blunt Delta Body." AIAA Journal, 10, No. 7 (July 1972), 887-894.
28. Kutler, P. "Computation of Three-Dimensional, Inviscid Supersonic Flows." Lecture Notes in Physics, Springer-Verlag, No. 41, Progress in Numerical Fluid Dynamics, 1975.
29. Bakker, P. G., and Bannink, W. J. "Conical Stagnation Points in the Supersonic Flow Around Slender Circular Cones at Incidence." Delft University of Technology, Delft, Department of Aeronautical Engineering Report VHT-184, November 1974.
30. Vinokur, M. "Conservation Equations of Gasdynamics in Curvilinear Coordinate Systems." Journal of Computational Physics, 14, No. 2 (February 1974), 105-125.
31. Viviani, H. "Conservative Forms of Gas Dynamic Equations." LaRecherche Aeronautique, No. 1 (January-February 1974), 65-68.
32. MacCormack, R. W. "The Effect of Viscosity in Hypervelocity Impact Cratering." AIAA Paper 69-354, 1969.
33. Kutler, P., and Shankar, V. S. Vijaya "Diffraction of a Shock Wave by a Compression Corner; Part I - Regular Reflection." AIAA Paper 76-323, 1976.
34. Richtmyer, R. D., and Morton, J. W. Difference Methods for Initial-Value Problems. New York: John Wiley & Sons, 1967.
35. Kentzer, C. P. "Discretization of Boundary Conditions on Moving Discontinuities." Lecture Notes in Physics, Springer-Verlag, No. 8, Proceedings of the Second International Conference on Numerical Methods in Fluid Dynamics, 1970.
36. Kutler, P., and Shankar, V. "Computation of the Inviscid Supersonic Flow Over an External Axial Corner." Proceedings of the 1976 Heat Transfer and Fluid Mechanics Institute, University of California, Davis, June 21-23, 1976.
37. Moretti, G. "Experiments in Multidimensional Floating Shock-Fitting." PIBAL Report No. 73-18, Polytechnic Institute of Brooklyn, August 1973.
38. Shankar, V., Kutler, P., and Anderson, D. A. "Diffraction of a Shock Wave by a Compression Corner; Part II - Single Mach Reflection." AIAA Paper 77-89, 1977.
39. Merritt, D. L. "Mach Reflection on a Cone." AIAA Journal, 6, No. 6 (June 1968), 1208-1209.

40. Ames Research Staff. "Equations, Tables, and Charts for Compressible Flow." National Advisory Committee for Aeronautics, NACA Report 1135, 1953.



# APPENDIX A. STRONG CONSERVATION-LAW FORM OF THE GOVERNING EQUATIONS AND THE GEOMETRIC DERIVATIVES

Since the equations of motion in fluid mechanics are derived from conservation principles (mass, momentum, and energy), it is often convenient to cast the equations in divergence form or conservation-law form which explicitly displays the conserved quantities such as mass, momentum, and energy. In the Cartesian system  $(x, y, t)$  the gas-dynamic equations (continuity, x-momentum, y-momentum, and energy) for inviscid, nonheat-conducting, and adiabatic flow can be written in conservation-law form as:

$$U_t + E_x + F_y = 0 \quad (A1)$$

where

$$U = \begin{pmatrix} \rho \\ \rho u \\ \rho v \\ e \end{pmatrix} \quad E = \begin{pmatrix} \rho u \\ p + \rho u^2 \\ \rho uv \\ (p + e)u \end{pmatrix} \quad F = \begin{pmatrix} \rho v \\ \rho uv \\ p + \rho v^2 \\ (p + e)v \end{pmatrix}$$

$u$  and  $v$  are the velocity components in  $x$  and  $y$  directions, and  $p$ ,  $\rho$ , and  $e$  are the pressure, density, and total energy per unit volume. The system of equations is made complete by specifying the total energy in the form:

$$e = \frac{1}{\gamma - 1} p + \frac{\rho}{2} (u^2 + v^2) \quad (A2)$$

In most fluid mechanics problems it is necessary to make a coordinate transformation from the Cartesian coordinates  $(x, y, t)$  to some other system  $(\eta, \xi, \tau)$ , in order to facilitate the easy application of surface boundary conditions on arbitrary shaped bodies. Sometimes coordinate transformations

are needed to incorporate some of the special features of the flow field (conical flows, self-similar flows, etc.) in the numerical formulation of the problem.

Let the new coordinates  $\tau$ ,  $\eta$ , and  $\xi$  be related to the Cartesian system  $t$ ,  $x$ , and  $y$  by the transformation:

$$\left. \begin{aligned} \tau &= t \\ \eta &= \eta(x, y, t) \\ \xi &= \xi(x, y, t) \end{aligned} \right\} \quad (A3)$$

To arrive at the transformed equations, the derivatives with respect to  $x$ ,  $y$ , and  $t$  in Equation (A1) are replaced in terms of the derivatives with respect to  $\tau$ ,  $\eta$ , and  $\xi$  in the following manner:

$$\left. \begin{aligned} \frac{\partial}{\partial x} &= \frac{\partial}{\partial \eta} \eta_x + \frac{\partial}{\partial \xi} \xi_x \\ \frac{\partial}{\partial y} &= \frac{\partial}{\partial \eta} \eta_y + \frac{\partial}{\partial \xi} \xi_y \\ \frac{\partial}{\partial t} &= \frac{\partial}{\partial \tau} + \frac{\partial}{\partial \eta} \eta_t + \frac{\partial}{\partial \xi} \xi_t \end{aligned} \right\} \quad (A4)$$

Making use of Equation (A4), Equation (A1) can be written as

$$U_\tau + \eta_t U_\eta + \xi_t U_\xi + \eta_x E_\eta + \xi_x E_\xi + \eta_y F_\eta + \xi_y F_\xi = 0 \quad (A5)$$

Equation (A5) can always be rewritten as

$$U'_\tau + E'_\eta + F'_\xi + H' = 0 \quad (A6)$$

where

$$\left. \begin{aligned} U' &= U \\ E' &= \eta_t U + \eta_x E + \eta_y F \\ F' &= \xi_t U + \xi_x E + \xi_y F \\ H' &= -\left( U\eta_{t\eta} + E\eta_{x\eta} + F\eta_{y\eta} + U\xi_{t\xi} + E\xi_{x\xi} + F\xi_{y\xi} \right) \end{aligned} \right\} \quad (A7)$$

All the terms in the untransformed Equation (A1) are derivatives of the unknown four-component vectors (U, E, and F) with respect to the independent variables (t,x,y). This is said to be in strong conservation-law form (30). The transformed Equation (A6) is said to be in weak conservation-law form because of the presence of an undifferentiated term  $H'$ . This term is analogous to the fictitious body force term. The presence of the  $H'$  term in the governing transformed equation is undesirable for two reasons. First, it prevents the achievement of overall conservation of mass, momentum, and energy. Second, it involves several second derivatives ( $\eta_{t\eta}$ ,  $\eta_{x\eta}$ ,  $\eta_{y\eta}$ ,  $\xi_{t\xi}$ ,  $\xi_{x\xi}$ ,  $\xi_{y\xi}$ ). The analytical expressions required to evaluate these second derivatives may be difficult to obtain. As a result these are evaluated numerically thus increasing the computer time.

In the present work, the transformed Equation (A5) is rewritten in strong conservation-law form to avoid the undesirable features of the weak conservation-law form. In order to bring Equation (A6) into a strong conservation-law form the  $H'$  term must somehow be removed by including appropriate terms into  $U'$ ,  $E'$ , and  $F'$  before the derivative is taken. The technique of Viviani (31) is applied here.

The Jacobian of the transformation is given by

$$J = \frac{\partial(\eta, \xi, \tau)}{\partial(x, y, t)} = \begin{vmatrix} \eta_x & \eta_y & \eta_t \\ \xi_x & \xi_y & \xi_t \\ \tau_x & \tau_y & \tau_t \end{vmatrix} = \eta_x \xi_y - \eta_y \xi_x \quad (A8)$$

If the transformation is regular the Jacobian is neither zero nor infinite. Assuming the Jacobian to be finite, all the terms in Equation (A5) are divided by the Jacobian  $J$ . It can then be rearranged as

$$\begin{aligned}
& \left[ \frac{U}{J} \right]_{\tau} + \left[ \frac{U\eta_t + E\eta_x + F\eta_y}{J} \right]_{\eta} + \left[ \frac{U\xi_t + E\xi_x + F\xi_y}{J} \right]_{\xi} - \left[ U \left\{ \left( \frac{1}{J} \right)_{\tau} + \left( \frac{\eta_t}{J} \right)_{\eta} + \left( \frac{\xi_t}{J} \right)_{\xi} \right\} \right. \\
& \quad \left. + E \left\{ \left( \frac{\eta_x}{J} \right)_{\eta} + \left( \frac{\xi_x}{J} \right)_{\xi} \right\} + F \left\{ \left( \frac{\eta_y}{J} \right)_{\eta} + \left( \frac{\xi_y}{J} \right)_{\xi} \right\} \right] = 0 \quad (A9)
\end{aligned}$$

It can be easily shown that all the terms inside the fourth bracket cancel out. Thus, Equation (A9) is composed of only the first three bracketed terms. The strong conservation-law of the transformed equations can thus be written in a simpler fashion as:

$$\bar{U}_{\tau} + \bar{E}_{\eta} + \bar{F}_{\xi} = 0 \quad (A10)$$

where

$$\left. \begin{aligned}
\bar{U} &= U/J \\
\bar{E} &= (U\eta_t + E\eta_x + F\eta_y)/J \\
\bar{F} &= (U\xi_t + E\xi_x + F\xi_y)/J \\
J &= \eta_x \xi_y - \eta_y \xi_x
\end{aligned} \right\} \quad (A11)$$

For an analytical transformation the geometric derivatives  $\eta_t$ ,  $\eta_x$ ,  $\eta_y$ ,  $\xi_t$ ,  $\xi_x$  and  $\xi_y$  can be evaluated analytically. For a numerical transformation these geometric derivatives will have to be evaluated numerically.

In the regular reflection problem (refer Figure 5) the independent variable transformation  $\tau = t$ ,  $\eta = \eta(x, y, t)$ , and  $\xi = \xi(x, y, t)$  which includes the self-similarity of the problem and a normalization of the distance between the ramp and the reflected shock is given by:

$$\left. \begin{aligned}
\tau &= t \\
\eta &= \frac{x - x_b(y)}{x_s(y, t) - x_b(y)} \\
\xi &= \frac{y}{t}
\end{aligned} \right\} \quad (A12)$$

where  $x_b(y) = y \cot \theta_r$  represents the equation of the ramp, and  $x_s(y,t)$  represents the equation of the reflected shock. The geometric derivatives required by Equation (A10) are:

$$\left. \begin{aligned} \eta_t &= -\frac{\eta x_{s_t}}{x_s - x_b} & \xi_t &= -\frac{\xi}{\tau} \\ \eta_x &= \frac{1}{x_s - x_b} & \xi_x &= 0 \\ \eta_y &= -\frac{x_{b_y} - \eta(x_{s_y} - x_{b_y})}{x_s - x_b} & \xi_y &= \frac{1}{\tau} \end{aligned} \right\} \quad (A13)$$

Since  $\xi_x = 0$ , the Jacobian reduces to  $J = \eta_x \xi_y$ .

In the Mach reflection problem (refer Figure 19a), the transformation involves a double normalization procedure. The transformation functions  $\tau$ ,  $\eta$ , and  $\xi$  include the self-similarity of the problem, a normalization of the distance between the ramp and the reflected shock and a normalization of the distance between the wall and the Mach stem. They are given by:

$$\left. \begin{aligned} \tau &= t \\ \eta &= \frac{x - X_b(\xi, \tau)}{X_s(\xi, \tau) - X_b(\xi, \tau)} \\ \xi &= \frac{y - Y_b(\tau)}{Y_s(\eta, \tau) - Y_b(\tau)} \end{aligned} \right\} \quad (A14)$$

Since the wall is aligned with the  $x$ -axis, the equation of the wall is just  $Y_b(\tau) = 0$  or  $\xi = 0$ . In Equation (A14),  $X_b(\xi, \tau) = y \cot \theta_r = \xi Y_s(0, \tau) \cot \theta_r$  represents the equation of the ramp ( $\eta = 0$ ),  $X_s(\xi, \tau)$  represents the equation of the reflected shock, and  $Y_s(\eta, \tau)$  represents the equation of the Mach stem. The body and the shock shapes are defined in terms of the computational

variables  $\eta$ ,  $\xi$ , and  $\tau$  and not in terms of the physical variables  $x$ ,  $y$ , and  $t$ . Such a representation is necessary because the constant  $\eta$  and constant  $\xi$  lines are not parallel to the  $x$  and  $y$  axis, respectively.

Corresponding to the transformation given by Equations (A14), the geometric derivatives are obtained as follows:

$$\begin{aligned}
 \eta_x &= \frac{\frac{\partial(\eta, y, t)}{\partial(\eta, \xi, \tau)}}{\frac{\partial(x, y, t)}{\partial(\eta, \xi, \tau)}} = \frac{\begin{vmatrix} \eta_\eta & \eta_\xi & \eta_\tau \\ y_\eta & y_\xi & y_\tau \\ t_\eta & t_\xi & t_\tau \end{vmatrix}}{\begin{vmatrix} x_\eta & x_\xi & x_\tau \\ y_\eta & y_\xi & y_\tau \\ t_\eta & t_\xi & t_\tau \end{vmatrix}} = \frac{y_\xi}{x_\eta y_\xi - x_\xi y_\eta} \\
 \eta_y &= \frac{\frac{\partial(x, \eta, t)}{\partial(\eta, \xi, \tau)}}{\frac{\partial(x, y, t)}{\partial(\eta, \xi, \tau)}} = - \frac{x_\xi}{x_\eta y_\xi - x_\xi y_\eta} \\
 \eta_t &= \frac{\frac{\partial(x, y, \eta)}{\partial(\eta, \xi, \tau)}}{\frac{\partial(x, y, t)}{\partial(\eta, \xi, \tau)}} = \frac{x_\xi y_\tau - x_\tau y_\xi}{x_\eta y_\xi - x_\xi y_\eta} \\
 \xi_x &= \frac{\frac{\partial(\xi, y, t)}{\partial(\eta, \xi, \tau)}}{\frac{\partial(x, y, t)}{\partial(\eta, \xi, \tau)}} = - \frac{y_\eta}{x_\eta y_\xi - x_\xi y_\eta} \\
 \xi_y &= \frac{\frac{\partial(x, \xi, t)}{\partial(\eta, \xi, \tau)}}{\frac{\partial(x, y, t)}{\partial(\eta, \xi, \tau)}} = \frac{x_\eta}{x_\eta y_\xi - x_\xi y_\eta} \\
 \xi_t &= \frac{\frac{\partial(x, y, \xi)}{\partial(\eta, \xi, \tau)}}{\frac{\partial(x, y, t)}{\partial(\eta, \xi, \tau)}} = \frac{x_\tau y_\eta - x_\eta y_\tau}{x_\eta y_\xi - x_\xi y_\eta}
 \end{aligned} \tag{A15}$$

Evaluation of (A15) requires the following:

$$x_{\tau} = \eta X_{S_{\tau}}(\xi, \tau) + (1 - \eta) X_{b_{\tau}}(\xi, \tau)$$

$$x_{\xi} = \eta X_{S_{\xi}}(\xi, \tau) + (1 - \eta) X_{b_{\xi}}(\xi, \tau)$$

$$x_{\eta} = X_S(\xi, \tau) - X_b(\xi, \tau)$$

$$y_{\tau} = \xi Y_{S_{\tau}}(\eta, \tau)$$

$$y_{\xi} = Y_S(\eta, \tau)$$

$$y_{\eta} = \xi Y_{S_{\eta}}(\eta, \tau)$$

(A16)

## APPENDIX B. INTEGRATION PROCEDURE AND STEP SIZE CALCULATIONS

MacCormack (32) has constructed a two step, preferential, predictor-corrector sequence for use in solving systems of differential equations written in the conservation-law form. The scheme is second order in both time and space. In application to nonlinear equations with several dependent and independent variables, the method has low storage requirements and simple programming logic.

As applied to Equation (A10) MacCormack's method is as follows:

$$\tilde{\bar{U}}_{j,k}^{n+1} = \bar{U}_{j,k}^n - \frac{\Delta\tau}{\Delta\eta} \left( \bar{E}_{j+1,k}^n - \bar{E}_{j,k}^n \right) - \frac{\Delta\tau}{\Delta\xi} \left( \bar{F}_{j,k+1}^n - \bar{F}_{j,k}^n \right) \quad (B1)$$

$$\bar{U}_{j,k}^{n+1} = \frac{1}{2} \left[ \bar{U}_{j,k}^n + \tilde{\bar{U}}_{j,k}^{n+1} - \frac{\Delta\tau}{\Delta\eta} \left( \tilde{\bar{E}}_{j,k}^{n+1} - \tilde{\bar{E}}_{j-1,k}^{n+1} \right) - \frac{\Delta\tau}{\Delta\xi} \left( \tilde{\bar{F}}_{j,k}^{n+1} - \tilde{\bar{F}}_{j,k-1}^{n+1} \right) \right] \quad (B2)$$

The tilde that appears over certain of the variables denotes the predicted value of that particular variable. The subscripts  $j$  and  $k$  refer to mesh indices whereas the subscript  $n$  refers to the time.

In this version forward differences are used in the predictor and backward differences in the corrector. However, one could use backward differences in the predictor and forward differences in the corrector. Another possibility is to use a forward difference for the  $\eta$ -derivative and a backward difference for the  $\xi$ -derivative in the predictor and the opposite in the corrector. Because of these various options MacCormack's scheme is termed a preferential difference scheme.

In the case of a boundary mesh point for which the forward grid is not available, the forward difference in the predictor in that direction is modified to a backward difference in that direction. Similarly, if the backward grid is not available then the backward difference in the corrector



is modified to a forward difference in that direction. For example, for all the grid points along the ramp no backward grid point is available in the  $\eta$ -direction. At these grid points the term  $\tilde{E}_{j,k}^{n+1} - \tilde{E}_{j-1,k}^{n+1}$  in the corrector is modified to  $\tilde{E}_{j+1,k}^{n+1} - \tilde{E}_{j,k}^{n+1}$ .

The integration step size  $\Delta\tau$  must be specified to initiate the calculation. The maximum allowable step size  $\Delta\tau_\eta$  in the  $\eta$ -direction and the maximum allowable step size  $\Delta\tau_\xi$  in the  $\xi$ -direction are obtained from the one-dimensional, amplification matrix, stability analysis (34) of MacCormack scheme. They are given by

$$\Delta\tau_\eta = \text{CN} \frac{\Delta\eta}{|\sigma_{\max,\eta}|} \quad (\text{B3})$$

$$\Delta\tau_\xi = \text{CN} \frac{\Delta\xi}{|\sigma_{\max,\xi}|} \quad (\text{B4})$$

where CN is the Courant number,  $\sigma_{\max,\eta}$  is the maximum eigenvalue in the  $(\eta-\tau)$  plane, and  $\sigma_{\max,\xi}$  is the maximum eigenvalue in the  $(\xi-\tau)$  plane. For the calculation to be stable, the minimum of the two step sizes  $\Delta\tau_\eta$  and  $\Delta\tau_\xi$  is used:

$$\Delta\tau = \min(\Delta\tau_\eta, \Delta\tau_\xi) \quad (\text{B5})$$

In order to compute these maximum eigenvalues first the equations of motion are written in nonconservation form in terms of the transformed coordinates variables  $\eta$ ,  $\xi$ , and  $\tau$ . The continuity equation and the energy or the entropy equation are coupled together to eliminate any derivatives of density. This is done in the following manner:

$$\text{Continuity:} \quad \rho_t + \vec{q} \cdot \nabla \rho + \rho \nabla \cdot \vec{q} = 0 \quad (\text{B6})$$

$$\text{Energy:} \quad p_t - c^2 \rho_t + \vec{q} \cdot (\nabla p - c^2 \nabla \rho) = 0 \quad (\text{B7})$$

where

$$\vec{q} = u\hat{i} + v\hat{j}$$

$$\nabla = \frac{\partial}{\partial x} \hat{i} + \frac{\partial}{\partial y} \hat{j}$$

$$c^2 = \frac{\gamma p}{\rho}$$

Multiplying Equation (B6) by  $c^2$  and adding it to Equation (B7) results in

$$p_t + up_x + vp_y + \rho c^2(u_x + v_y) = 0 \quad (B8)$$

In terms of the transformed coordinate variables  $\eta$ ,  $\xi$ , and  $\tau$  Equation (B8) becomes

$$p_\tau + p_\eta \bar{u} + p_\xi \bar{v} + \rho c^2(u_\xi \xi_x + u_\eta \eta_x + v_\xi \xi_y + v_\eta \eta_y) = 0 \quad (B9)$$

where

$$\bar{u} = \eta_t + u\eta_x + v\eta_y \quad (B10)$$

$$\bar{v} = \xi_t + u\xi_x + v\xi_y \quad (B11)$$

The x-momentum and the y-momentum equations are also written in terms of the transformed coordinates.

$$\text{x-momentum: } u_\tau + p_\eta \eta_x / \rho + p_\xi \xi_x / \rho + u_\eta \bar{u} + u_\xi \bar{v} = 0 \quad (B12)$$

$$\text{y-momentum: } v_\tau + p_\eta \eta_y / \rho + p_\xi \xi_y / \rho + v_\eta \bar{u} + v_\xi \bar{v} = 0 \quad (B13)$$

Equations (B9), (B12), and (B13) are written in matrix form as:

$$Q_\tau + A_1 Q_\eta + A_2 Q_\xi = 0 \quad (B14)$$

where

$$Q = \begin{pmatrix} p \\ u \\ v \end{pmatrix}, \quad A_1 = \begin{pmatrix} \bar{u} & \rho c^2 \eta_x & \rho c^2 \eta_y \\ \eta_x / \rho & \bar{u} & 0 \\ \eta_y / \rho & 0 & \bar{u} \end{pmatrix}, \quad A_2 = \begin{pmatrix} \bar{v} & \rho c^2 \xi_x & \rho c^2 \xi_y \\ \xi_x / \rho & \bar{v} & 0 \\ \xi_y / \rho & 0 & \bar{v} \end{pmatrix} \quad (B15)$$

The matrix  $A_1$  has three eigenvalues the maximum of which is  $\sigma_{\max,\eta}$ . Similarly the matrix  $A_2$  has three eigenvalues the maximum of which is  $\sigma_{\max,\xi}$ . The eigenvalues of  $A_1$  are obtained by solving the matrix equation

$$|A_1 - I\sigma| = 0 \quad (B16)$$

Where  $I$  is the identity matrix. Solving Equation (B16) yields the following three eigenvalues:

$$\sigma_1^{A1} = \bar{u} \quad (B17)$$

$$\sigma_{2,3}^{A1} = \bar{u} \pm c\sqrt{\eta_x^2 + \eta_y^2} \quad (B18)$$

The absolute maximum is given by

$$|\sigma_{\max,\eta}| = |\bar{u}| + c\sqrt{\eta_x^2 + \eta_y^2} \quad (B19)$$

Similarly solving  $|A_2 - I\sigma| = 0$  yields the following three eigenvalues:

$$\sigma_1^{A2} = \bar{v} \quad (B20)$$

$$\sigma_{2,3}^{A2} = \bar{v} \pm c\sqrt{\xi_x^2 + \xi_y^2} \quad (B21)$$

and

$$|\sigma_{\max,\xi}| = |\bar{v}| + c\sqrt{\xi_x^2 + \xi_y^2} \quad (B22)$$

The integration step size is now given by

$$\Delta\tau = \min\left(CN \frac{\Delta\eta}{|\bar{u}| + c\sqrt{\eta_x^2 + \eta_y^2}}, \quad CN \frac{\Delta\xi}{|\bar{v}| + c\sqrt{\xi_x^2 + \xi_y^2}}\right) \quad (B23)$$

Equation (B23) is evaluated at each of the grid points in the computational plane and the smallest value of  $\Delta\tau$  over all the grid points is then chosen as the integration step size. The Courant number  $CN$  is usually chosen to be one or slightly less than one.

## APPENDIX C. EXACT SOLUTION FOR REGULAR REFLECTION

When a planar shock strikes a wall it will reflect in one of two forms, regular reflection or Mach reflection. The form that occurs depends on the shock strength and the shock incident angle. In the present problem (refer Figure C1) the incident planar blast wave denoted by its strength  $M_s$  strikes the ramp with an incident angle of  $(90-\theta_r)$ , where  $\theta_r$  is the ramp angle measured from the positive  $x$ -axis. For incident shock Mach numbers greater than 1.5, regular reflection results as long as the incident angle is less than  $39^\circ$  (39).

In the numerical formulation of the regular reflection problem, the computational region is chosen such that the outer boundary (refer Figure 6a) falls between the sonic circle and the point  $I$  where the incident shock strikes the ramp. Along the outer boundary exact two-dimensional regular reflection results are specified and kept fixed throughout the iterative process. The exact regular reflection results are obtained by making use of various shock relations in the following manner.

As the incident shock moves with a Mach number  $M_s$ , the shock incident point  $I$  (Figure C1) moves up the ramp with a Mach number  $M_s/\cos \theta_r$ . The shock relations such as the Rankine Hugoniot jump conditions are applicable only when the shock is at rest. These shock relations can be applied to a moving shock by merely employing a moving coordinate system relative to which the shock is at rest. By placing a moving coordinate  $(x',y')$  rigidly attached to the moving point  $I$ , the stationary region (1) in the  $(x,y)$  system becomes nonstationary in the  $(x',y')$  system. With respect to the moving system  $(x',y')$  the nonstationary flow in region (1) is parallel to

the ramp and has a Mach number  $M_s/\cos \theta_r$  as shown in Figure C2. The transformation from  $(x,y)$  to  $(x',y')$  system alters only the velocities in the regions (1), (2), (3). The pressure and density remain unchanged. The velocities with respect to the  $(x',y')$  system are denoted by a prime.

To obtain the flow variables in regions (2) and (3), first the pressure and density in region (1) are chosen to be unity (i.e.,  $p_1 = \rho_1 = 1$ ). Then the following equations found in NACA 1135 (40) are used.

$$a_1 = \sqrt{\frac{\gamma p_1}{\rho_1}} = \sqrt{\gamma} \sim \text{speed of sound in region (1)} \quad (C1)$$

$$q_s = M_s \sqrt{\gamma} \sim \text{velocity of the incident shock} \quad (C2)$$

$$q'_1 = \frac{q_s}{\cos \theta_r} \sim \text{velocity in region (1) with respect to } (x',y') \text{ system} \quad (C3)$$

$$M'_1 = \frac{q'_1}{a_1} \quad (C4)$$

$$p_2 = p_1 \left[ \frac{2\gamma M_s^2 - (\gamma - 1)}{\gamma + 1} \right] \sim \text{pressure in region (2)} \quad (C5)$$

$$\rho_2 = \rho_1 \left[ \frac{(\gamma + 1) M_s^2}{(\gamma - 1) M_s^2 + 2} \right] \sim \text{density in region (2)} \quad (C6)$$

$$\theta_1 = \frac{\pi}{2} - \theta_r \quad (C7)$$

$$M_{N1} = M'_1 \sin \theta_1 = M_s \quad (C8)$$

$$q'_2 = q'_1 \sqrt{1 - \frac{4(M_{N1}^2 - 1)(\gamma M_{N1}^2 + 1)}{(\gamma + 1)^2 M_{N1}^2 M_1'^2}} \sim \text{velocity in region (2) with respect to } (x',y') \text{ system} \quad (C9)$$

$$\delta = \tan^{-1} \left[ \frac{2 \cot \theta_1 (M_s^2 - 1)}{2 + M_1'^2 (\gamma + 1 - 2 \sin^2 \theta_1)} \right] \sim \text{flow deflection angle from region (1) to (2)} \quad (C10)$$

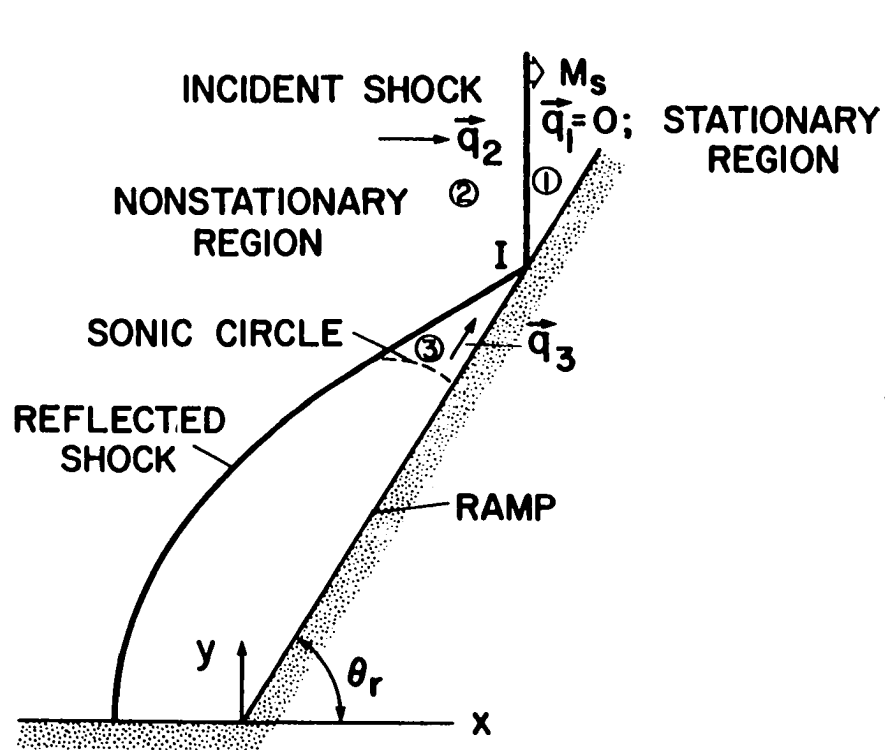


Figure C1. Regular reflection in a fixed  $x, y$  Cartesian system

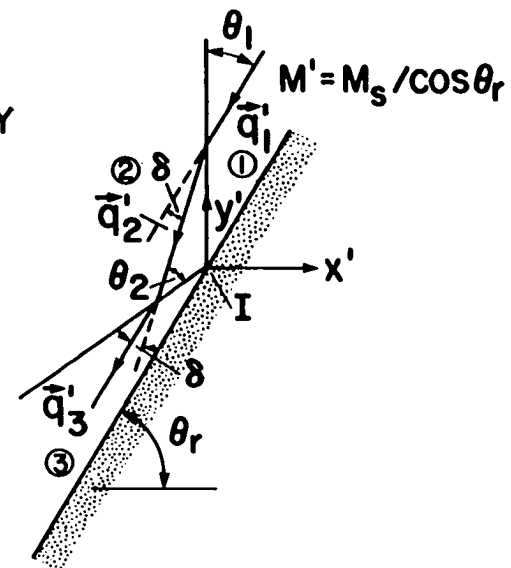


Figure C2. Regular reflection in a moving  $x', y'$  Cartesian system rigidly attached at the point  $I$

$$a_2 = \sqrt{\frac{\gamma p_2}{\rho_2}} \sim \text{speed of sound in region } (2) \quad (C11)$$

$$M_2' = \frac{q_2'}{a_2} \quad (C12)$$

In region (3) the flow again becomes parallel to the ramp. Thus knowing  $\delta$  and  $M_2'$  the reflected shock angle  $\theta_2$  is found by solving the following polynomial:

$$\sin^6 \theta_2 + b \sin^4 \theta_2 + c \sin^2 \theta_2 + d = 0 \quad (C13)$$

where

$$b = -\frac{M_2'^2 + 2}{M_2'^2} - \gamma \sin^2 \delta \quad (C14)$$

$$c = \frac{2M_2'^2 + 1}{M_2'^2} + \left[ \frac{(\gamma + 1)^2}{4} + \frac{\gamma - 1}{M_2'^2} \right] \sin^2 \delta \quad (C15)$$

$$d = -\frac{\cos^2 \delta}{M_2'^4} \quad (C16)$$

Equation (C15) has three roots, the smallest of which corresponds to a decrease in entropy and should therefore be disregarded according to the second law of thermodynamics. The largest root corresponds to the strong shock. The middle root, which corresponds to the weak shock, is the one of interest.

$$M_{N2} = M_2' \sin \theta_2 \quad (C17)$$

$$q_3' = q_2' \sqrt{1 - \frac{4(M_{N2}^2 - 1)(\gamma M_{N2}^2 + 1)}{(\gamma + 1)^2 M_{N2}^2 M_2'^2}} \sim \text{velocity in region } (3) \text{ with respect to } (x'y') \text{ system} \quad (C18)$$

$$p_3 = p_2 \left[ \frac{2\gamma M_{N2}^2 - (\gamma - 1)}{\gamma + 1} \right] \sim \text{pressure in region } (3) \quad (C19)$$

$$\rho_3 = \rho_2 \left[ \frac{(\gamma + 1)M_{N2}^2}{(\gamma - 1)M_{N2}^2 + 2} \right] \sim \text{density in region } \textcircled{3} \quad (\text{C20})$$

Knowing the velocities  $q'_1$ ,  $q'_2$ , and  $q'_3$  in the  $(x', y')$  system, the velocities  $q_1$ ,  $q_2$ , and  $q_3$  in the  $(x, y)$  system are obtained by employing the simple transformation:

$$\vec{q}_1 = \vec{q}'_1 - \vec{q}'_1 = \vec{0} = u_1 \hat{i} + v_1 \hat{j} \quad (\text{C21})$$

$$\vec{q}_2 = \vec{q}'_2 - \vec{q}'_1 = u_2 \hat{i} + v_2 \hat{j} \quad (\text{C22})$$

$$\vec{q}_3 = \vec{q}'_3 - \vec{q}'_1 = u_3 \hat{i} + v_3 \hat{j} \quad (\text{C23})$$

where

$$q'_1 = q'_1 (-\cos \theta_r \hat{i} - \sin \theta_r \hat{j}) \quad (\text{C24})$$

$$q'_2 = q'_2 (-\cos[\theta_r + \delta] \hat{i} - \sin[\theta_r + \delta] \hat{j}) \quad (\text{C25})$$

$$q'_3 = q'_3 (-\cos \theta_r \hat{i} - \sin \theta_r \hat{j}) \quad (\text{C26})$$

and  $(u_1, v_1)$ ,  $(u_2, v_2)$ , and  $(u_3, v_3)$  are the Cartesian velocity components in regions  $\textcircled{1}$ ,  $\textcircled{2}$ , and  $\textcircled{3}$ , respectively.



## APPENDIX D. KENTZER'S SCHEME FOR IMPERMEABLE BOUNDARIES

An impermeable boundary is one across which no mass can flow such as a solid surface or a plane of symmetry. At an impermeable boundary a surface tangency condition must be satisfied. Proper implementation of the surface boundary condition is a crucial step in computing the correct body pressure distribution. One method of applying the surface boundary condition is to use Kentzer's (35) scheme at the body grid points.

Kentzer's scheme is based on the method of characteristics approach in combination with one-sided finite differences. Here, the aim is to derive an expression for  $p_\tau$  valid at the body points which can be integrated in a predictor-corrector fashion to obtain the body pressure. This is achieved by combining the characteristic compatibility relation and the surface tangency condition in differential form. The procedure is outlined below for both the ramp and the wall.

The eigenvalues of the time dependent Euler equations have already been derived in Appendix B (see Equations (B6) through Equation (B21)). The left eigenvectors  $y_1^{A_1}$  corresponding to the eigenvalues of the  $A_1$  matrix are obtained by solving

$$y_i^{A_1}(A_1 - I\sigma_i^{A_1}) = 0 \quad i = 1, 2, 3 \quad (D1)$$

Similarly solving

$$y_i^{A_2}(A_2 - I\sigma_i^{A_2}) = 0 \quad i = 1, 2, 3 \quad (D2)$$

yields the left eigenvectors  $y_i^{A_2}$  corresponding to the  $A_2$  matrix. The final result is

$$\left. \begin{aligned}
 y_1^{A_1} &= (0, \eta_y, -\eta_x) \\
 y_{2,3}^{A_1} &= \left( 1, \pm \frac{\rho c \eta_x}{\sqrt{\eta_x^2 + \eta_y^2}}, \pm \frac{\rho c \eta_y}{\sqrt{\eta_x^2 + \eta_y^2}} \right) \\
 y_1^{A_2} &= (0, \xi_y, -\xi_x) \\
 y_{2,3}^{A_2} &= \left( 1, \pm \frac{\rho c \xi_x}{\sqrt{\xi_x^2 + \xi_y^2}}, \pm \frac{\rho c \xi_y}{\sqrt{\xi_x^2 + \xi_y^2}} \right)
 \end{aligned} \right\} \quad (D3)$$

The compatibility relations are obtained from these eigenvectors and eigenvalues.

Referring to Figure D1, only the down running characteristics drawn in the  $(\xi - \tau)$  plane strikes the wall grid point. The eigenvalue associated with this characteristic is  $\sigma_3^{A_2}$ . Kentzer's scheme requires only the compatibility relation along this down running characteristic. The compatibility relation is derived by starting from Equation (B14).

$$Q_\tau + A_1 Q_\eta + A_2 Q_\xi = 0 \quad (D4)$$

Multiplying Equation (D4) throughout by  $y_3^{A_2}$  and making use of Equation (D2) it results in the form

$$y_3^{A_2} (Q_\tau + \sigma_3^{A_2} Q_\xi) = y_3^{A_2} A_1 Q_\eta \quad (D5)$$

Substituting for  $y_3^{A_2}$  from Equation (E3) and for  $Q$  from Equation (B15), Equation (D5) simplifies to

$$\begin{aligned}
& (p_\tau + \sigma_3^{A_2} p_\xi) - \frac{\rho c \xi_x}{\sqrt{\xi_x^2 + \xi_y^2}} (u_\tau + \sigma_3^{A_2} u_\xi) - \frac{\rho c \xi_y}{\sqrt{\xi_x^2 + \xi_y^2}} (v_\tau + \sigma_3^{A_2} v_\xi) \\
& = - \left[ \bar{u} p_\eta + \rho c^2 \eta_x u_\eta + \rho c^2 \eta_y v_\eta - \frac{\rho c \xi_x}{\sqrt{\xi_x^2 + \xi_y^2}} \left( \frac{\eta_x p_\eta}{\rho} + \bar{u} u_\eta \right) \right. \\
& \quad \left. - \frac{\rho c \xi_y}{\sqrt{\xi_x^2 + \xi_y^2}} \left( \frac{\eta_y p_\eta}{\rho} + \bar{u} v_\eta \right) \right] \tag{D6}
\end{aligned}$$

Along the wall the surface tangency condition in differential form is given by

$$\left. \begin{aligned} v_\tau &= 0 \\ v_\eta &= 0 \end{aligned} \right\} \tag{D7}$$

In addition along the wall (plane of symmetry)  $\bar{v}$  is zero and  $\xi_x$  is zero. Combining Equation (D6) and Equation (D7) and then substituting for  $u_\tau$  from Equation (B12) yields the following expression for  $p_\tau$  valid only at the wall grid points.

$$p_\tau = - \left( \sigma_3^{A_2} p_\xi - \rho c \sigma_3^{A_2} v_\xi + \bar{u} p_\eta + \rho c^2 \eta_x u_\eta - \frac{\rho c \eta_y p_\eta}{\rho} \right) \tag{D8}$$

$$u_\tau = -p_\eta \frac{\eta_x}{\rho} - \bar{u} u_\eta \tag{D9}$$

Equations (D8) and (D9) are integrated in a predictor-corrector fashion to get the pressure and the  $u$ -velocity at the wall grid points at the new time level.

$$\left. \begin{aligned} \bar{p}_{j,k}^{n+1} &= p_{j,k}^n + (p_\tau)_{j,k}^n \Delta\tau \\ \bar{u}_{j,k}^{n+1} &= u_{j,k}^n + (u_\tau)_{j,k}^n \Delta\tau \end{aligned} \right\} \text{ predictor} \tag{D10}$$

$$\left. \begin{aligned} p_{j,k}^{n+1} &= p_{j,k}^n + \frac{1}{2} \left[ (p_\tau)_j^n + (\tilde{p}_\tau)_j^{n+1} \right] \Delta\tau \\ u_{j,k}^{n+1} &= u_{j,k}^n + \frac{1}{2} \left[ (u_\tau)_j^n + (\tilde{u}_\tau)_j^{n+1} \right] \Delta\tau \end{aligned} \right\} \text{corrector} \quad (D11)$$

In evaluating  $p_\tau$  and  $u_\tau$ , forward differences are used for the  $\eta$  and  $\xi$  derivatives in the predictor. In the corrector backward differences are used for the  $\eta$  derivatives and forward differences for the  $\xi$  derivatives.

Knowing the pressure and the  $u$ -component of the velocity all the other flow variables can be easily computed. This procedure is outlined in Chapter II under Boundary Conditions.

Similar to the analysis presented above, an expression for  $p_\tau$  and  $u_\tau$  are now derived for the ramp grid points. Referring to Figure E2, only the down running characteristics drawn in the  $(\eta - \tau)$  plane strikes the ramp grid point. The eigenvalue associated with this characteristics is  $\sigma_3^{A1}$ . The compatibility relation along this down running characteristics is obtained by multiplying Equation (D4) by  $y_3^{A1}$ .

$$y_3^{A1} (Q_\tau + \sigma_3^{A1} Q_\eta) = -y_3^{A1} A_2 Q_\xi \quad (D12)$$

Substituting for  $y_3^{A1}$  from Equation (D3) and for  $Q$  from Equation (B15), Equation (D12) results in

$$\begin{aligned} (p_\tau + \sigma_3^{A1} p_\eta) - \frac{\rho c \eta_x}{\sqrt{\eta_x^2 + \eta_y^2}} (u_\tau + \sigma_3^{A1} u_\eta) - \frac{\rho c \eta_y}{\sqrt{\eta_x^2 + \eta_y^2}} (v_\tau + \sigma_3^{A1} v_\eta) \\ = - \left[ \bar{v} p_\xi + \rho c^2 \xi_x u_\xi + \rho c^2 \xi_y v_\xi - \frac{\rho c \eta_x}{\sqrt{\eta_x^2 + \eta_y^2}} \left( \xi_x \frac{p_\xi}{\rho} + \bar{v} u_\xi \right) \right. \\ \left. - \frac{\rho c \eta_y}{\sqrt{\eta_x^2 + \eta_y^2}} \left( \xi_y \frac{p_\xi}{\rho} + \bar{v} v_\xi \right) \right] \end{aligned} \quad (D13)$$

Along the ramp the surface tangency condition in differential form is given by

$$\left. \begin{aligned} v_{\xi} &= u_{\xi} \tan \theta_r \\ v_{\tau} &= u_{\tau} \tan \theta_r \end{aligned} \right\} \quad (D14)$$

In addition,  $\bar{u}$  is zero along the ramp. Combining Equation (D14) and then substituting for  $u_{\tau}$  from Equation (B12) yields the following expression for  $p_{\tau}$  valid only at the ramp points.

$$\begin{aligned} p_{\tau} = & - \left( \sigma_3^{A1} p_{\eta} - \frac{\rho c \eta_x}{\sqrt{\eta_x^2 + \eta_y^2}} \sigma_3^{A1} u_{\eta} - \frac{\rho c \eta_y}{\sqrt{\eta_x^2 + \eta_y^2}} \sigma_3^{A1} v_{\eta} + \bar{v} p_{\xi} \right. \\ & \left. + \rho c^2 \xi_x u_{\xi} + \rho c^2 \xi_y v_{\xi} - \frac{\rho c \eta_x}{\sqrt{\eta_x^2 + \eta_y^2}} \xi_x \frac{p_{\xi}}{\rho} - \frac{\rho c \eta_y}{\sqrt{\eta_x^2 + \eta_y^2}} \xi_y \frac{p_{\xi}}{\rho} \right) \end{aligned} \quad (D15)$$

$$u_{\tau} = -p_{\eta} \frac{\eta_x}{\rho} - p_{\xi} \frac{\xi_x}{\rho} - \bar{v} u_{\xi} \quad (D16)$$

Equations (D15) and (D16) are integrated in a predictor-corrector fashion described by Equations (D10) and (D11). In evaluating  $p_{\tau}$  and  $u_{\tau}$  forward differences are used for  $\eta$  and  $\xi$  derivatives in the predictor. In the corrector backward differences are used for the  $\xi$  derivatives and forward differences for the  $\eta$  derivatives. Knowing the pressure and the u-component of the velocity all the flow variables are easily obtained.

By combining the compatibility relation with the surface tangency condition in differential form, the disadvantages of the true method of characteristics, the iterations and the interpolations to get the data at specific points on a characteristic, are eliminated in Kentzer's scheme.

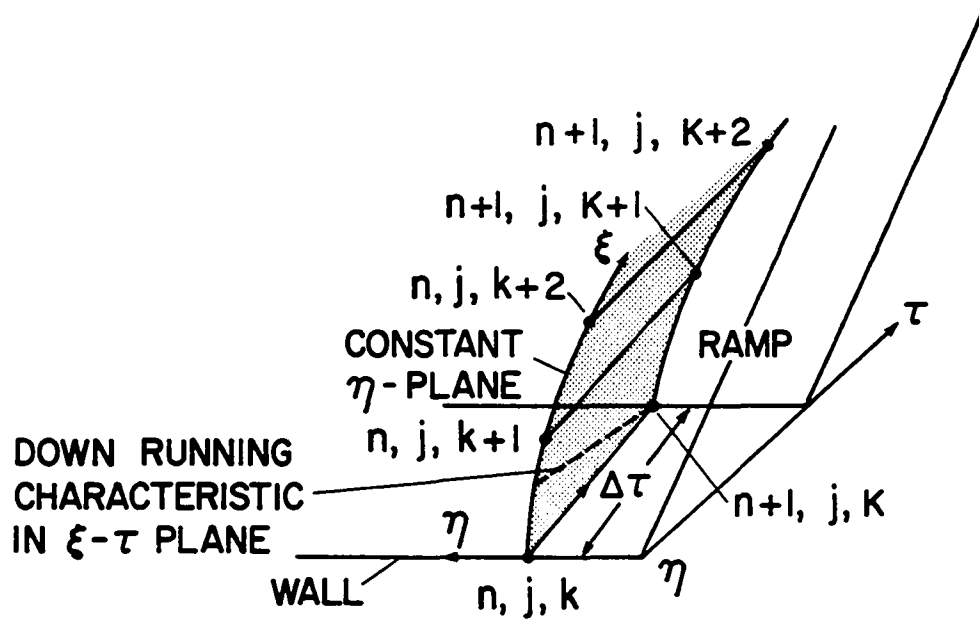


Figure D1. Kentzer's scheme at the wall point ( $k = 1$ )

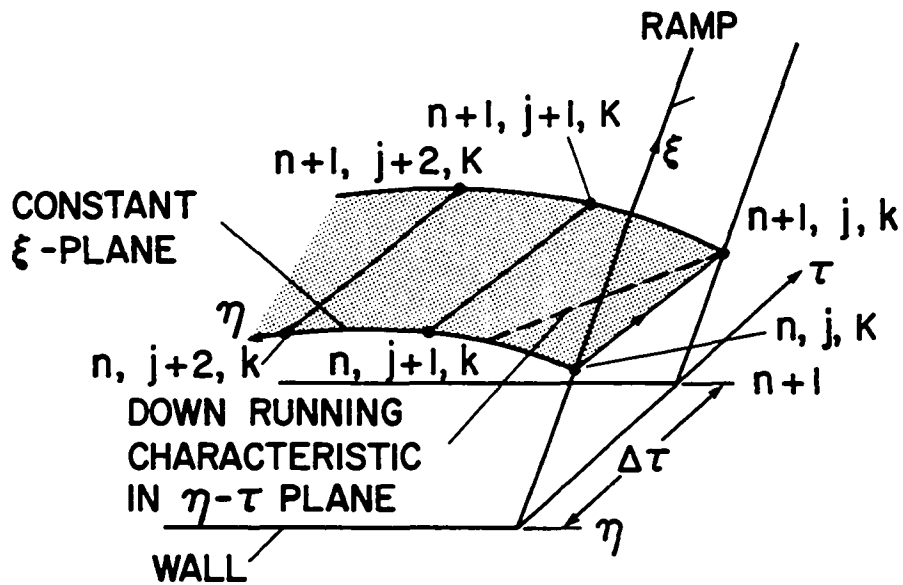


Figure D2. Kentzer's scheme at the ramp point ( $j = 1$ )

## APPENDIX E. EXACT TRIPLE POINT SOLUTION

When the incident angle (that is the angle between the incident planar shock and the ramp) is greater than  $39^\circ$ , Mach reflection occurs as long as the incident shock Mach number is greater than 1.5 (39). As mentioned in the Introduction (Chapter I), the Mach reflection can take various forms depending on the incident angle and the incident shock strength. The present problem considers only the single Mach reflection case in which only one triple point is present. Since the flow field is self-similar the triple point moves along a straight line denoted by the triple point trajectory angle  $\chi$  in Figure E1.

As was pointed out in Appendix C, all the shock jump conditions are true only if the shock is at rest. In order to obtain a solution to the moving triple point where the incident shock, the reflected shock, the Mach stem, and the slip surface meet, a moving Cartesian coordinate  $(x',y')$  is rigidly placed at the moving triple point. With respect to the  $(x',y')$  system the triple point is at rest and the flow comes into the triple point along the triple point trajectory with a Mach number  $M_s/\cos(\theta_r + \chi)$ , as shown in Figure E2. The transformation from  $(x,y)$  to  $(x',y')$  system alters only the velocities in regions (1), (2), (3), and (4). The pressure and density remain unchanged. The velocities in the two system  $(x,y)$  and  $(x',y')$  are related to each other by means of a simple transformation.

The triple point solution is first obtained in the  $x',y'$  system where all the shock relations found in NACA 1135 (40) are applicable. Knowing flow variables in region (1), region (2) is easily obtained using oblique shock relations. To solve regions (3) and (4) uniquely, an iterative procedure is

necessary to satisfy the two jump conditions across the slip surface. In the  $x', y'$  system the slip surface is at rest. The two jump conditions across a stationary slip surface are one, the pressure must be same on either side of the slip surface and two, the velocity vector on either side must be parallel to the slip surface. Knowing region (1), the following procedure explains how to obtain the flow variables in regions (2), (3), and (4).

$$p_1 = \rho_1 = 1 \sim \text{pressure and density in region (1)} \quad (\text{E1})$$

$$a_1 = \sqrt{\frac{\gamma p_1}{\rho_1}} = \sqrt{\gamma} \sim \text{speed of sound in region (1)} \quad (\text{E2})$$

$$q_s = M_s \sqrt{\gamma} \sim \text{velocity of the incident shock} \quad (\text{E3})$$

$$q'_1 = \frac{q_s}{\cos(\theta_r + \chi)} \sim \text{velocity in region (1) with respect to } (x', y') \text{ system} \quad (\text{E4})$$

$$M'_1 = \frac{q'_1}{a_1} \quad (\text{E5})$$

$$p_2 = p_1 \left[ \frac{2\gamma M_s^2 - (\gamma - 1)}{\gamma + 1} \right] \sim \text{pressure in region (2)} \quad (\text{E6})$$

$$\rho_2 = \rho_1 \left[ \frac{(\gamma + 1)M_s^2}{(\gamma - 1)M_s^2 + 2} \right] \sim \text{density in region (2)} \quad (\text{E7})$$

$$\theta_1 = \frac{\pi}{2} - \theta_r - \chi \quad (\text{E8})$$

$$M_{N1} = M'_1 \sin \theta_1 = M_s \quad (\text{E9})$$

$$q'_2 = q'_1 \sqrt{1 - \frac{4(M_{N1}^2 - 1)(\gamma M_{N1}^2 + 1)}{(\gamma + 1)^2 M_{N1}^2 M_1'^2}} \quad (\text{E10})$$

$$\delta = \tan^{-1} \left[ \frac{2 \cot \theta_1 (M_s^2 - 1)}{2 + M_1'^2 (\gamma + 1 - 2 \sin^2 \theta_1)} \right] \quad (\text{E11})$$



$$a_2 = \sqrt{\frac{\gamma p_2}{\rho_2}} \quad (\text{E12})$$

$$M_2' = \frac{q_2'}{a_2} \quad (\text{E13})$$

This completes region (2) calculations. The following iterative procedure determines region (3) and region (4) flow conditions.

1. For a given Mach number there is a maximum flow deflection angle. Knowing  $M_2'$  in region (2), the maximum flow deflection angle  $\delta_{\max}$  across the reflected shock is computed from

$$\cot \delta_{\max} = \left( \frac{\gamma + 1}{2} \frac{M_2'^2}{M_2'^2 \sin^2 \beta_{\max} - 1} - 1 \right) \tan \beta_{\max} \quad (\text{E14})$$

$$\beta_{\max} = \sin^{-1} \sqrt{\frac{1}{\gamma M_2'^2} \left[ \frac{\gamma + 1}{4} M_2'^2 - 1 + \sqrt{(\gamma + 1) + \frac{\gamma^2 - 1}{2} M_2'^2 + \frac{(\gamma + 1)^2}{16} M_2'^2} \right]} \quad (\text{E15})$$

The flow deflection angle  $\delta_R$  across the reflected shock has to be less than or equal to  $\delta_{\max}$ .

2. An initial value for the Mach stem angle  $\xi_M$  is chosen. The Mach stem being a strong shock, the initial value for  $\xi_M$  is chosen to be  $89.99^\circ$ .

3. Corresponding to the assumed Mach stem angle  $\xi_M$  and the Mach number  $M_1'$ , the flow deflection angle  $\delta_M$  is obtained from

$$\delta_M = \tan^{-1} \left[ \frac{2 \cot \xi_M (M_1'^2 \sin^2 \xi_M - 1)}{2 + M_1'^2 (\gamma + 1 - 2 \sin^2 \xi_M)} \right] \quad (\text{E16})$$

4. The pressure in region (4) is computed from

$$p_4 = p_1 \left[ 1 + \frac{2\gamma}{\gamma + 1} (M_1'^2 \sin^2 \xi_M - 1) \right] \quad (\text{E17})$$

5. The slip surface angle  $\alpha$  is given by

$$\alpha = 90^\circ - \delta_M - \theta_r - \chi \quad (\text{E18})$$

6. Since the flow in region (3) has to be parallel to the slip surface the flow deflection angle  $\delta_R$  across the reflected shock is given by

$$\delta_R = \alpha - (90^\circ - \theta_r - \chi - \delta) \quad (\text{E19})$$

7. If  $\delta_R$  is greater than  $\delta_{\max}$  given by Equation (D14), the initial guess for  $\xi_M$  is reduced by  $0.01^\circ$  and the calculation is repeated from step 3 until  $\delta_R$  becomes equal to or less than  $\delta_{\max}$ .

8. Knowing the flow deflection angle  $\delta_R$  and the Mach number  $M_2'$  the shock angle  $\xi_R$  is computed. The procedure is outlined in Appendix C.

9. The pressure in region (3) is then computed from

$$p_3 = p_2 \left[ 1 + \frac{2\gamma}{\gamma + 1} (M_2'^2 \sin^2 \xi_R - 1) \right] \quad (\text{E20})$$

10. Across the slip surface the pressure must be same (i.e.,  $p_3 = p_4$ ).

If the convergence criteria

$$|p_3 - p_4| \leq 10^{-4} \quad (\text{E21})$$

is not satisfied then the assumed value of  $\xi_M$  is reduced by 0.005 and the calculation is repeated from step 3. This repetition is continued until the convergence criteria is satisfied.

11. The total velocities  $q_3'$  in region (3) and  $q_4'$  in region (4) are given by

$$q_3' = q_2' \sqrt{1 - \frac{4(M_2'^2 \sin^2 \xi_R - 1)(\gamma M_2'^2 \sin^2 \xi_R + 1)}{(\gamma + 1)^2 M_2'^4 \sin^2 \xi_R}} \quad (\text{E22})$$

$$q_4' = q_1' \sqrt{1 - \frac{4(M_1'^2 \sin^2 \xi_M - 1)(\gamma M_1'^2 \sin^2 \xi_M + 1)}{(\gamma + 1)^2 M_1'^4 \sin^2 \xi_M}} \quad (\text{E23})$$

12. Knowing the velocities  $q'_1, q'_2, q'_3$ , and  $q'_4$  in  $x', y'$  system, the velocities  $q_1, q_2, q_3$ , and  $q_4$  in  $x, y$  system are obtained by employing the simple transformation:

$$\vec{q}_1 = \vec{q}'_1 - \vec{q}'_1 = \vec{0} = u_1 \hat{i} + v_1 \hat{j} \quad (\text{E24})$$

$$\vec{q}_2 = \vec{q}'_2 - \vec{q}'_1 = u_2 \hat{i} + v_2 \hat{j} \quad (\text{E25})$$

$$\vec{q}_3 = \vec{q}'_3 - \vec{q}'_1 = u_3 \hat{i} + v_3 \hat{j} \quad (\text{E26})$$

$$\vec{q}_4 = \vec{q}'_4 - \vec{q}'_1 = u_4 \hat{i} + v_4 \hat{j} \quad (\text{E27})$$

where

$$\vec{q}'_1 = q'_1 [-\cos(\theta_r + \chi) \hat{i} - \sin(\theta_r + \chi) \hat{j}] \quad (\text{E28})$$

$$\vec{q}'_2 = q'_2 [-\cos(\theta_r + \chi + \delta) \hat{i} - \sin(\theta_r + \chi + \delta) \hat{j}] \quad (\text{E29})$$

$$\vec{q}'_3 = q'_3 [-\sin \alpha \hat{i} - \cos \alpha \hat{j}] \quad (\text{E30})$$

$$\vec{q}'_4 = q'_4 [-\sin \alpha \hat{i} - \cos \alpha \hat{j}] \quad (\text{E31})$$

and  $(u_1, v_1), (u_2, v_2), (u_3, v_3)$ , and  $(u_4, v_4)$  are the Cartesian velocity components in regions (1), (2), (3), and (4), respectively.

13. The slopes of the reflected shock and the Mach stem are given by

$$\phi_M = \theta_r + \chi + \xi_M \quad (\text{E32})$$

$$\phi_R = \theta_r + \chi + \delta + \xi_R \quad (\text{E33})$$

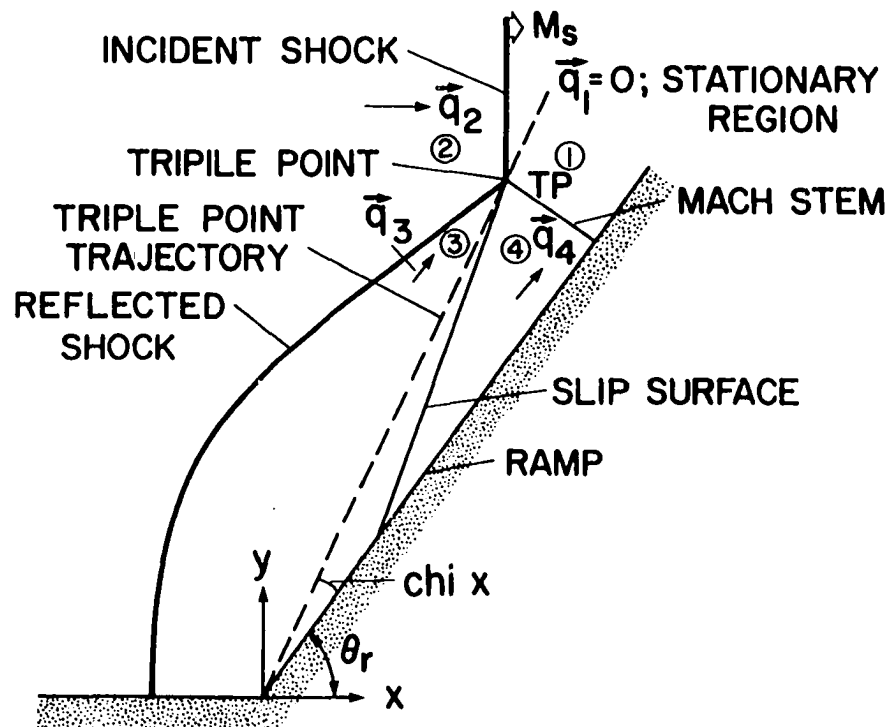


Figure E1. Mach reflection in a fixed  $x, y$  Cartesian system

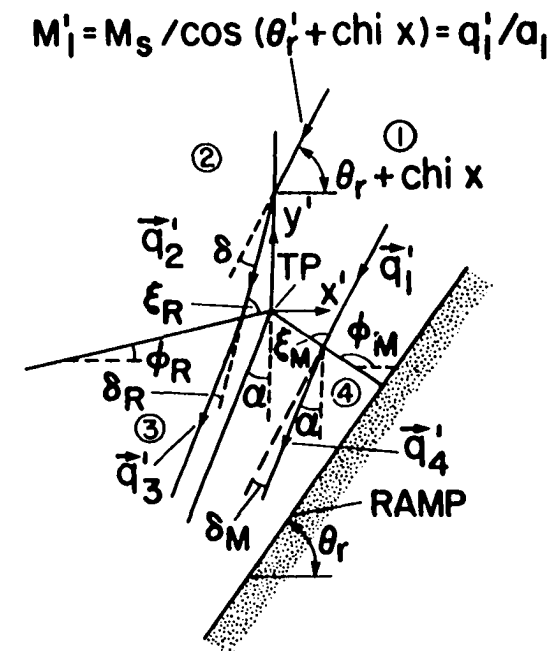


Figure E2. Mach reflection in a moving  $x', y'$  system rigidly attached at the triple point TP